NONLINEAR FINITE ELEMENT MODELING OF REINFORCED CONCRETE COLUMNS

by

Yağız Erçin

B.S., Civil Engineering, Yıldız Technical University, 2014

Submitted to the Institute for Graduate Studies in
Science and Engineering in partial fulfillment of
the requirements for the degree of
Master of Science

Graduate Program in Civil Engineering
Boğaziçi University
2018

ACKNOWLEDGEMENTS

I would like to express my sincerest gratitude to my thesis advisor, Associate Prof. Kutay Orakçal for his continuing support and invaluable guidance throughout this research. His knowledge and positive approach was very helpful and encouraging all the time.

I would also like to thank the members of my Master's thesis examination committee: Associate Prof. Serdar Soyöz and Prof. Alper İlki for their constructive comments and recommendations.

I would like to express my special thanks to M. Fethi Güllü for his generous help and guidance on model code. His contribution to this thesis was invaluable.

I am also grateful to Prof. Bilge Doran and Associate Prof. Murat Altekin for their encouragement and support since my undergraduate years.

I would like to thank my friend Emir Hazar Bekaroğlu, who has been my classmate since undergraduate years, for his help during the preparation of this thesis. I would also like to thank many friends for their support over the course of my studies, especially Korkut Kaynardağ, Yavuz Altuğ and Ecem Akcan for their companionship during long hours of study.

Most of all, I would like to thank my parents and my sister who have always supported me. Finally, I wish to thank my wife. Without her love, patience and support, I could not have completed this thesis.

ABSTRACT

NONLINEAR FINITE ELEMENT MODELING OF REINFORCED CONCRETE COLUMNS

Analytical modeling of the lateral load response of reinforced concrete columns under reversed cyclic loading conditions is investigated in this study, using a relatively simple finite element model formulation developed originally for reinforced concrete walls. The objective of this analytical study is successful simulation of the lateral load response of RC columns, irrespective of whether the response and failure mode is flexure-controlled, shear-controlled or a combination of flexural and shear responses. The behavior of the constitutive panel elements in the finite element model formulation is based on a fixed-crack-angle modeling approach. Shear aggregate interlock stresses along cracks and dowel action on the reinforcing bars are considered in the model formulation. The model also incorporates rotational springs at the column-pedestal interface, in order to represent strain penetration effects on the reinforcing bars anchored within the pedestal. Regularization of the post-peak stress-strain behavior of concrete in compression was also conducted, using a simple methodology, to minimize strain localization effects in the analysis results. For calibration and experimental validation of the model, column specimens tested as part of four experimental programs, with both flexure-controlled and shear-controlled responses, are used. Model predictions are compared with test results for selected twelve column specimens with a variety of geometric properties, reinforcement configurations, loading conditions, and response characteristics. The model is shown to provide reasonably accurate response predictions for the specimens investigated, in terms of lateral load capacity, drift capacity, stiffness, strength degradation behavior, and pinching characteristics. Based on comparison of model results with the test observations, model capabilities and limitations are identified.

ÖZET

BETONARME KOLONLARIN DOĞRUSAL OLMAYAN DAVRANIŞLARININ SONLU ELEMANLAR YÖNTEMİ İLE MODELLENMESİ

Bu çalışmada betonarme kolonların çevrimsel yatay yükleme altındaki davranışı, daha önce betonarme perde duvarlar için geliştirilmiş olan bir sonlu elemanlar modelleme yöntemi kullanılarak, analitik olarak incelenmiştir. Çalışmanın amacı, göçme modu açısından hem baskın eğilme, hem baskın kesme, hem de birleşik kesme-eğilme davranışı gösteren betonarme kolon davranışını kestirebilen bir modelleme yöntemi geliştirmektir. Modeli oluşturan sonlu elemanlarının doğrusal olmayan davranışı, bir sabit çatlak (payanda) açışı modelleme yaklaşımı kullanılarak temsil edilmiştir. Çatlak yüzeyleri boyunca oluşan agrega kenetlenmesi etkileri ve donatı çubuklarında oluşan kama etkileri, model formülasyonunda göz önüne alınmıştır. Modelin kolon ile temel birleşiminde bir dönme mafsalı kullanılarak, kolon boyuna donatısının temel içindeki akma penetrasyonu davranışı analizlerde gözetilmiştir. Analizlerde şekildeğiştirme lokazilazyonu etkilerini mümkün olduğunca minimize etmek amacıyla, betonun basınç altındaki gerilme-birim şekil değiştirme davranışı, literatürde sunulmuş olan bağıntılar kullanılarak kalibre edilmiştir. Seçilen dört deneysel program kapsamında hem baskın eğilme davranışı, hem baskın kesme davranışı, hem de birleşik eğilme-kesme davranışı gösteren on iki kolon numunesi için elde edilmiş olan deney sonuçları, analitik model kestirimleri ile karşılaştırılmıştır. İncelenen kolon numuneleri, geometrik özellikleri, donatı konfigürasyonları, yükleme koşulları ve davranış özellikleri açısından farklılık göstermektedir. Analitik model, incelenen kolon numunelerinin yatay yük–yerdeğiştirme davranışını, yatay yük kapasitesi, yanal rijitlik, yerdeğiştirme kapasitesi, kapasiteye ulaştıktan sonra yatay yükte azalma davranışı, çevrimsel rijitlik azalımı ve daralma gibi karakteristik davranış özellikleri açısından makul başarıyla temsil etmektedir.

TABLE OF CONTENTS

LIST OF FIGURES

LIST OF TABLES

LIST OF SYMBOLS

A_{cc}	Core concrete area
A_e	Effectively confined area
A_g	Gross concrete cross-section area
A_{st}	Total longitudinal steel area
A_{sx}	Total reinforcing bar area in x direction
A_{sy}	Total reinforcing bar area in y direction
b_c	Width of cross section
d_b	Diameter of reinforcing bar
d_c	Height of cross section
d_i	Local nodal displacement
D_i	Global nodal displacement
d_s	Diameter of reinforcing bar
$defx$	Deformation of mesh in x direction
$defy$	Deformation of mesh in y direction
$defyx$	Shear deformation of mesh in x direction
$defxy$	Shear deformation of mesh in y direction
D	Diameter of the circular cross section
$[E]$	Elasticity matrix
E_c	Elastic modulus for concrete
E_{cc}	Elastic modulus for confined concrete
EI_{eff}	Effective section stiffness of reinforced concrete member
f_c'	Peak concrete compressive strength
f'_{cc}	Confined strength of concrete
f_{cr}	Tensile cracking stress of concrete
f_{lx}	Lateral confinement pressure in x direction
f_{ly}	Lateral confinement pressure in y direction
f_s	Stress in transverse reinforcing bar
f_{yh}	Yield stress of horizontal reinforcement

$[G]$	Strain matrix
$G_{f,c}$	Fracture energy in compression
h	Height of mesh
$[k]$	Local stiffness matrix of one mesh
k_e	Confinement effectiveness coefficient
$[K]$	Global stiffness matrix
K	Analytical confinement ratio
K_θ	Rotational stiffness
l_d	Development Length
L_e	Element length
L_p	Plastic length
m	Mesh number in horizontal direction
n	Mesh number in vertical direction
N_i	Shape function for finite element model
P_{ax}	Axial load
r	Parameter defining shape of monotonic stress-strain curve for concrete
R_0, a_1, a_2	Steel parameters defining degradation of cyclic curvature
s	Spacing of stirrups or hoops
s'	Clear spacing of stirrups or hoops
V	Volume
w	Width of mesh
$w/$	With
w/o	Without
${w'}_i$	Clear spacing between laterally supported longitudinal reinforcing bars
x	Mesh length
x_{crn}	Critical strain parameter of concrete in compression by Saatcioglu and Razvi Model
x_{crp}	Critical strain parameter of concrete in tension by Belarbi and Hsu Model

γ_{xy}	Shear strain
ε_c'	Strain at peak compressive stress
ε_c	Stresses in concrete
ε_{cc}	Stresses in confined concrete
ε_{co}	Strain corresponding to peak stress in unconfined concrete
ε_{cr}	Concrete cracking strain
ε_o	Strain corresponding to peak stress
ε_p	Strain corresponding to peak stress
ε_r	Strain corresponding to zero stress
ε_x	Normal strain in x direction
ε_y	Normal strain in y direction
ε_{20}	Strain corresponding to residual stress
η	Normalized local coordinates of a mesh in y direction
ξ	Normalized local coordinates of a mesh in x direction
ρ	Reinforcement ratio
ρ_x	Reinforcement ratio in x direction
ρ_y	Reinforcement ratio in y direction
ρ_{cc}	Volumetric ratio of longitudinal steel
ρ_s	Volumetric ratio of the transverse confining steel
σ_c	Concrete stress
σ_x	Concrete normal stress in x direction
σ_y	Concrete normal stress in y direction
ϕ_x	Transverse reinforcing bar diameter
ϕ_y	Longitudinal reinforcing bar diameter
$\Delta\lambda$	The initial load increment
$\Delta\delta_n$	The initial displacement increment
$\Delta\delta$	Displacement increment
$\Delta\delta_r$	Residual displacement increment

LIST OF ACRONYMS/ABBREVIATIONS

2D	Two Dimensional
ACI	American Concrete Institute
DOF	Degree Of Freedom
FEM	Finite Element Model
FRP	Fiber Reinforced Polymers
FSAM	Fixed Strut Angle Model
MVLEM	Multiple Vertical Line Element Model
RC	Reinforced Concrete
SFI	Shear Flexure Interaction

1. INTRODUCTION

1.1. General

Under seismic actions, reinforced concrete columns are designed to reach their flexural capacity prior to reaching their shear strength, in order for them to exhibit adequate lateral displacement capacity. However, in existing buildings, columns may be subjected to high levels of axial load and may be constructed with insufficient amount of transverse reinforcement, which may lead to brittle flexural failure or shear failure. Based on variation of column geometry, reinforcement configuration and detailing, material characteristics, and loading conditions, various researchers have conducted numerous experimental and analytical studies to characterize the seismic response of RC columns. Axial load level, concrete quality, properties and anchorage characteristics of reinforcing steel bars, the amount and detailing of confinement, and shear strength are all crucial factors in determining the seismic response of RC columns in buildings. Such factors are also crucial in the seismic response of bridge columns with typically circular cross-sections.

For analytical representation of the seismic response of RC columns for design or seismic performance assessment purposes, reliable nonlinear modeling approaches that are capable of capturing the behavior of columns under generalized loading conditions are required. However, the current modeling approaches (e.g., plastic hinge or fiber models) used in nonlinear seismic performance assessment of RC structures typically represent nonlinear flexural behavior of columns (or walls) only, whereas the shear strength of a column (or a wall) is typically predicted using empirical relationships or code equations. However, such modeling approaches that do not take into account the combined effect of shear and axial/flexural modes of deformation on the overall response of a column typically result in overestimation of the lateral load capacity, as well as overestimation of the displacement (drift) capacity of columns with relatively high shear demands (e.g., low shear span-to-depth ratios) or deficiencies in the amount of shear reinforcement.

Most of the commonly-used model formulations for RC columns consider uncoupled flexural and shear responses, and incorporate empirical parameters or ad-hoc relationships to define shear response parameters (shear stiffness, shear strength, reduction in shear strength with increasing flexural ductility, etc.). There is still a need in the literature for a simple yet effective modeling approach that incorporates a mechanical formulation, which can capture the lateral load response of RC columns with reasonable accuracy, whether the column behavior/failure is flexure-dominated, shear controlled, or is governed by interaction between shear and flexural responses.

Based on these shortcomings, a relatively simple finite element modeling methodology, which was originally proposed by Gullu (2013) for simulating the response of reinforced concrete structural walls, is adopted in this study for simulating the lateral load behavior of reinforced concrete columns. The model is calibrated and experimentally validated against test results obtained from the literature, on column specimens with a variety of shear span to depth ratios, cross-sectional geometries, axial load levels, loading conditions, reinforcement configurations, and observed failure modes (shear vs. flexural). The behavior of the constitutive panel elements in the finite element model formulation is based on the Fixed-Strut-Angle Model proposed originally by Ulugtekin (2010). An updated formulation of the Fixed-Strut-Angle Model (Gullu and Orakcal, 2017), which incorporates peak-oriented hysteretic rules for representing shear aggregate interlock stresses along cracks and origin-oriented hysteretic rules for dowel action on the reinforcing bars, are used in the present model formulation. The model also incorporates rotational springs at column-pedestal interface, in order to represent strain penetration effects on the reinforcing bars anchored within the pedestal. Regularization of the post-peak stress-strain behavior of concrete in compression was also conducted, using a simple methodology, to minimize strain localization effects in the analysis results.

The main motivation of this analytical study is to capture, using a mechanical modeling approach, the lateral load response of columns that exhibit both flexure-controlled or shear-controlled response characteristics (or failure modes), as well as shear-flexure interaction behavior, using the same model formulation and calibration method. For calibration and experimental validation of the model, column specimens tested as part of four experimental programs (Lynn, 2001; Sezen and Moehle 2002, Benzoni and Priestley, 1996; Shanmugam 2009), which both flexure-controlled and shear-controlled responses, are used. Model predictions are compared with test results for selected twelve column specimens with a variety of geometric properties, reinforcement configurations, and response characteristics. Based on comparison of model results with test observations, model capabilities are discussed and potential model improvements are identified.

1.2. Literature Review

Various macroscopic and microscopic modeling approaches can be found in the literature for simulation of the nonlinear behavior of RC structural members under combined axial and lateral load demands (columns or walls). Microscopic models are based on detailed representation of local behavior; therefore they incorporate a more refined definition of local response, wheras macroscopic models focus on capturing the overall load-displacement response, with acceptable accuracy, using a semi-mechanical and semi-empirical modeling approach. Microscopic models are typically demanding in terms of complexities involved in development and calibration of the model, as well as computational time and stability of convergence. Macroscopic models, on the other hand, are much more effective are beneficial to use due to their basic formulation, simple calibration, and computational efficiency. However, their reliability is limited by the assumptions used in their formulation.

RC columns typically show predominantly flexural nonlinear behavior, due to their high aspect ratio compared to RC walls. Therefore, many researchers have focused on modeling of the nonlinear flexural behavior of columns. One of the early examples of flexural response modeling is the model by Takeda *et al.* (1970).

Within the scope of the research by Takeda *et al.* (1970), column specimens were constructed and tested under dynamic ground motions. Based on test results obtained for load deformation responses, a so-called "primary curve" was derived, with critical points corresponding to cracking and yielding. For mononotic loading cyclic load reversals, a set of rules were proposed based on test results.

Researchers also investigated hysteretic models to capture the nonlinear shear response of RC columns. One of the hysteretic models derived for shear behavior was the one proposed by Ozcebe and Saatcioglu (1989). This modeling methodology can simply be into two stages. At the first stage, a primary shear force versus shear displacement curve was obtained considering flexural, axial and shear forces under monotonic loading conditions up to the starting point of strength loss. The curve was derived from sectional analysis using the Compression Field Theory. At the second stage, hysteretic loading and reloading backbone curves were generated based on proposed equations that were derived from comparison of the analysis results with test measurements (Saatcioglu and Ozcebe, 1988; Saatcioglu *et al.*, 1998).

Another model to simulate the shear behavior of RC members was proposed by Ambrisi and Filippou (1999). This modeling approach was applied by dividing RC members into sub-elements to isolate the main characteristics that constituted hysteretic behavior under flexure, shear, and bond slip effects. The sub-elements were connected in series and they represented different deformation components. A linear-elastic sub-element was adopted to represent flexural behavior until the reinforcing bar yields. Following yielding of the section, a rigid-plastic sub-element was defined to represent the nonlinear flexural deformation components. Bond slip effect between reinforcing bar and concrete and opening and closing of flexural cracks were simulated by an interface bond-slip element. Another sub-element was defined in the model formulation to describe nonlinear behavior under shear deformations.

The Multiple-Vertical-Line-Element-Model (Vulcano *et al.*, 1988; Fischinger *et al.*, 1990; Orakcal *et al.*, 2004) is a simple yet effective model formulation to represent nonlinear flexural behavior of RC walls and columns (Figure 1.1).

The model incorporates important characteristic of flexural response, such as neutral axis migration, tension stiffening, concrete confinement, nonlinear shear deformation behavior (although de-coupled from nonlinear flexural behavior), and the influence of axial load on strength and stiffness. The flexural response was simulated using a series of uniaxial elements (as shown in Figure 1.1), and these were connected to infinitely rigid beams at top and bottom of the model element to enforce the plane sections assumption. A horizontal shear spring was assigned to the model element to capture either linear elastic of nonlinear force deformation behavior under shear deformation, but the model was primarily adopted to capture nonlinear flexural behavior. Flexural and shear responses are uncoupled in the model formulation, which is one of the main shortcomings of this model.

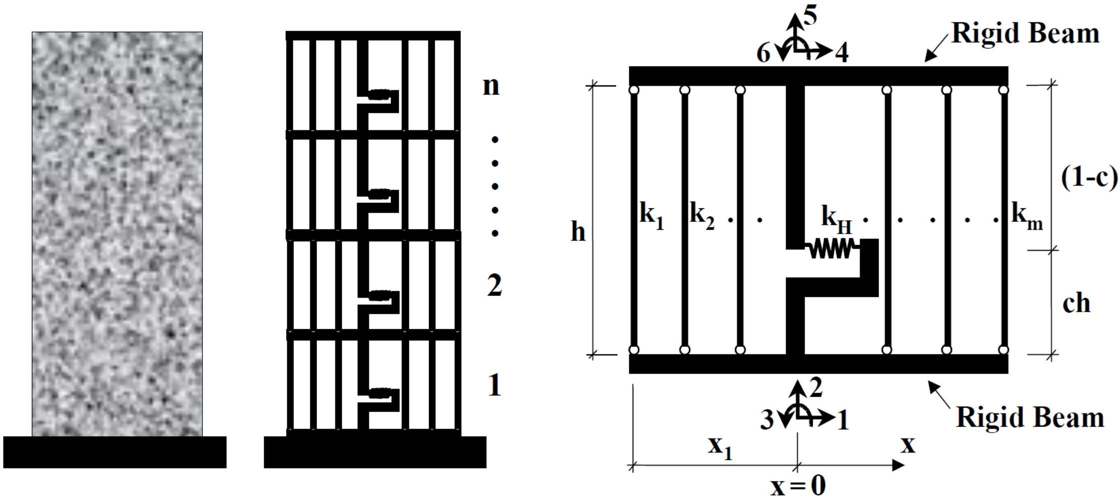

Figure 1.1. Multiple-Vertical-Line-Element-Model (MVLEM, Orakcal *et al.*, 2004)

Axial-shear-flexure interaction should be considered in nonlinear response modeling of RC columns, together with response characteristics such as strength deterioration, pinching behavior and stiffness degradation. Accordingly, Xu and Zhang (2011) proposed a hysteretic model considering shear-flexure interaction behavior for RC columns (Figure 1.2). This methodology is based on the constitutive shear model proposed by Ozcebe and Saatcioglu (1989), and flexural response model suggested by Takeda *et al.* (1970).

The model element consists of a flexural and a shear spring to represent flexure and shear displacement components at the element level. These springs were defined within the plastic hinge region of the columns. The overall response consisted of the flexural and shear backbone curves with a set of loading and unloading rules to generate the hysteretic behavioral characteristics. The main reason of the lumped plastic hinge model concept is based on the variation of response of columns with respect to their aspect ratios and loading conditions. For instance, in a cantilever column, shear and axial forces may be constant along the height, however bending moment gradually decreases towards the top of the column. Thus, moment curvature analysis were needed to consider the difference in behavior of different cross sections. According to the experimental program conducted by Ozcebe (1987), sections under larger M/V ratios tend to have larger moment capacities compared to sections with smaller M/V values. At the same time, smaller shear capacities are obtained for sections under larger of M/V ratios. This observation forms the basis of the modeling approach implemented, since it shows that shear capacity of a section cannot be defined independently of the bending moment demand on the section, and vice versa, and thus the lateral load capacity of the column (either flexural or shear) is related to its shear span.

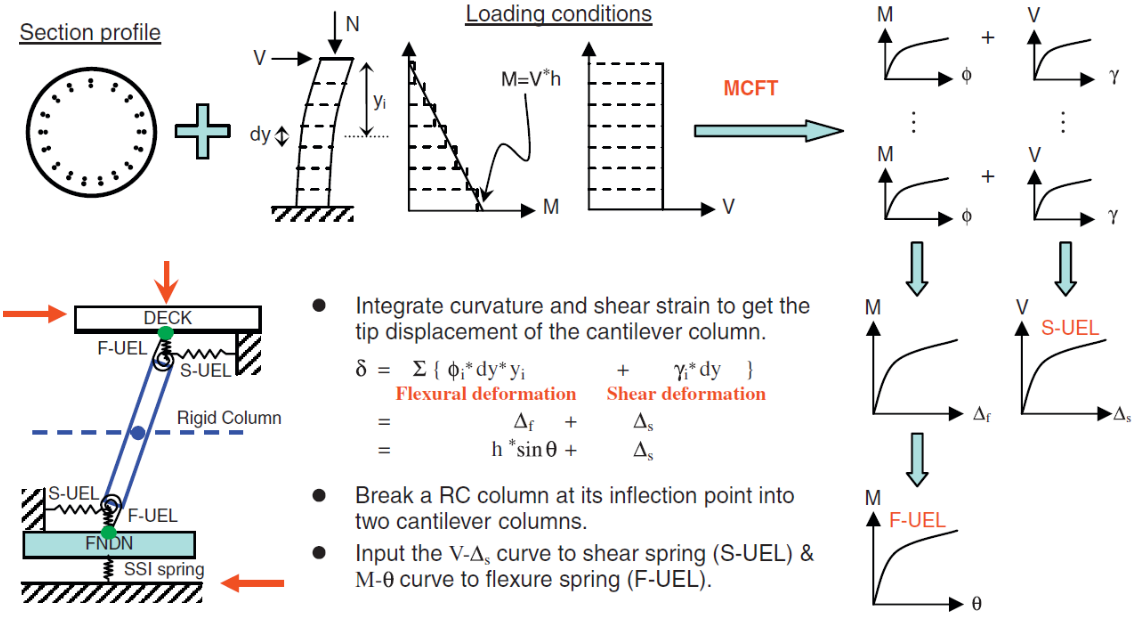

- Integrate curvature and shear strain to get the tip displacement of the cantilever column.

$$\delta = \Sigma\{\underbrace{\phi_i * dy * y_i}_{\text{Flexural deformation}} + \underbrace{\gamma_i * dy}_{\text{Shear deformation}}\}$$
$$= \Delta_f + \Delta_s$$
$$= h * \sin\theta + \Delta_s$$

- Break a RC column at its inflection point into two cantilever columns.
- Input the V-Δ_s curve to shear spring (S-UEL) & M-θ curve to flexure spring (F-UEL).

Figure 1.2. Implementation of the SFI scheme. (Xu and Zhang, 2011)

In the modeling approach by Xu and Zhang (2011), flexural and shear backbone curves were derived by separating shear and flexural components of the total monotonic force-displacement (pushover curve) relationship that was experimentally obtained from test results and analytically derived using the modified compression field theory. After separation of flexural and shear response components, decoupled curves were obtained. Moment–curvature and shear force–shear strain curves were integrated to obtain relative deformations along the height of the column specimens. Using the global and local equilibrium equations, envelopes of force–deformation responses were generated considering shear-flexure interaction. However, this modeling approach is more behavioral (semi-empirical) than mechanical although it considers coupling of shear and flexural response components.

Kolozvari (2013) developed a two dimensional macroscopic fiber model that considers shear–flexure interaction, based on the original formulation of the MVLEM, by replacing the uniaxial elements in the MVLEM with two-dimensional panel elements (Figure 1.3). For each constitutive panel element, the fixed-strut-angle model (FSAM) formulation proposed by Ulugtekin (2010), later improved by Orakcal *et al.* (2012), was adopted. Shear aggregate interlock effects and dowel action were incorporated in the model formulation using simple relationships. Since flexural and shear deformations are mechanically coupled in this model, reasonably accurate response predictions were captured with the model, at both global and local response levels for RC walls. However, effectiveness of the model for simulating the response of walls and columns failing under shear was not investigated in detail.

ElMandooh Galal and Ghoboraah (2003) proposed a shear–flexural hysteretic behavior model for biaxial cyclic and dynamic loading conditions. A triaxial spring was adopted in the model formulation since biaxial loading conditions were also considered. This three dimensional spring consist of flexure and shear subhinges at both end. Accordingly three flexure subhinges and one shear subhinge were assigned. Flexure subhinges represent the concrete cracking, steel yielding or ultimate conditions that element can be subjected to whereas shear subhinge provide model to capture shear failure. Moreover, axial load influence was accounted to on the subhinges.

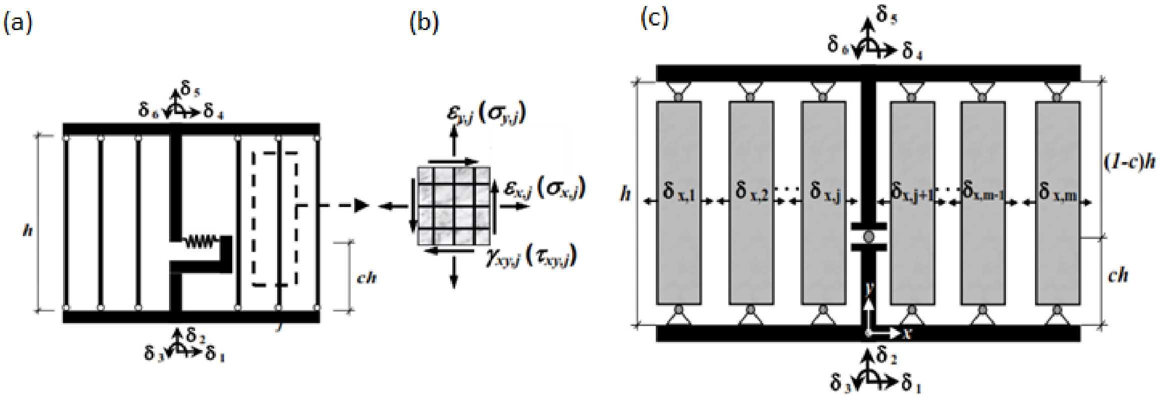

Figure 1.3. (a) Original MVLEM Element, (b) RC Panel Element, (c) SFI-MVLEM Element (Kolozvari *et al.*, 2013).)

Mullapudi and Ayoub (2010) generated a force-based finite element method to model the seismic behavior of shear-critical reinforced concrete columns. In this modeling approach, a smeared stress-strain methodology was adopted in the constitutive model elements, the behavior of which was represented using the so-called Softened Membrane Model. Stress and strain values were calculated using the equilibrium equations based on numerical integration, to obtain axial, shear, and flexural deformations and response components.

Hu and Barbato (2014) proposed a finite element method to estimate the response of circular columns. Their model was developed for columns confined with fiber reinforced polymers. Accordingly, the constitutive material model for concrete was adopted as unconfined, steel-confined, and FRP-confined. For simulating the cyclic stress-strain relationship of reinforcing steel, the Menegetto-Pinto (1973) model was used, and it was extended with implementation of isotropic strain hardening and local buckling effects. The model was force-based to achieve computational efficiency and high accuracy even for coarse mesh discretization.

As aforementioned, columns are not only subjected to one-directional lateral loads during seismic excitation. Therefore Osorio *et al.* (2017) conducted an experimental program and an analytical study to estimate the response of the reinforced concrete columns under lateral loads acting in more than one direction. Their model was derived to take into account bi-directional loading effects. They observed that bi-directional shear forces reduce the shear strength and confinement effect provided by transverse reinforcement. In their model formulation, shear-related strains and confinement strains on the transverse reinforcement were calculated separately and then the contributions were assembled. Moreover, since loading was bi-directional, shear strains were found to be higher compared to one-directional loading, which reduces the deformation capacity of the column.

One of the latest modeling methodologies was proposed by Mourlas *et al.* (2017). Their model was originally based on the concrete model proposed by Kotsovos and Pavlovic (1995), and their experimental program that was conducted to simulate the behavior of reinforced concrete members under cyclic loading. A smeared crack approach was adopted in this study, and reinforcing bars were modeled as truss and beam elements. The reinforcing bars were considered as embedded elements into the model, and the model element was assigned a hexahedral geometry, since it was developed for three dimensional analysis. A schematic representation of the model element and crack planes is depicted in Figure 1.4.

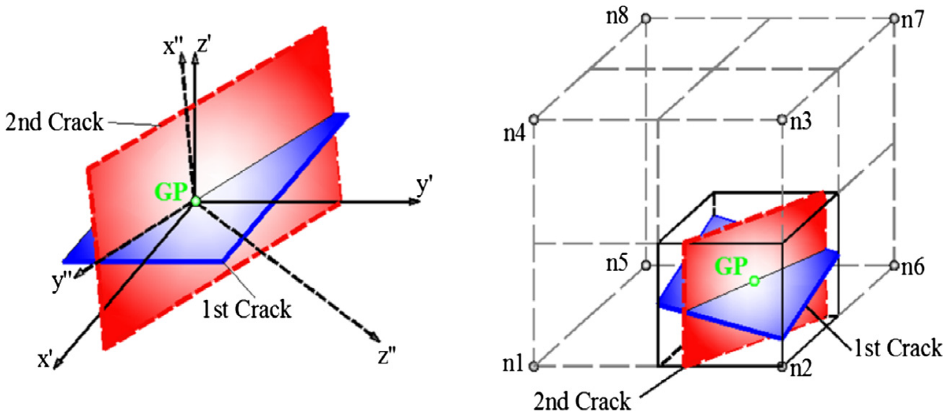

Figure 1.4. Sample Mesh and Two Crack Planes (Mourlas *et al.*, 2017)

In addition to the aforementioned modeling studies, many other researchers have proposed modeling methodologies for simulating the inelastic response of RC columns. As well, numerous experimental programs have been conducted to investigate the seismic response of RC columns, only a few interesting examples of which are summarized the following paragraphs.

Ozcebe (1987) conducted an experimental program to investigate the effects of the axial load variation, configuration and amount of transverse reinforcement, confinement conditions, and loading history on inelastic response of reinforced concrete columns. Two different transverse reinforcement configurations were considered in this study. Fourteen column specimens were laterally loaded under different axial load levels, using a single-curvature loading test setup.

Most of the test programs in the literature have neglected the effect of displacement history on the response of columns, by applying a standard loading history on the specimens. Within the scope of his study, Pujol (2002) tested sixteen cantilever columns under various displacement histories to obtain a correlation between drift capacity and displacement history.

Thomson and Wallace (1994) conducted experiments focusing on the behavior of high-strength reinforced concrete columns. Twelve specimens with varying transverse reinforcement spacing and configuration, reinforcing steel grades, and levels of axial load were tested in their study.

McDaniel (1997) tested three circular columns with different scales to investigate the scale effect on the response of reinforced concrete columns with circular cross-section.

Lehman and Moehle (1998) conducted an experimental program to characterize the response of circular columns used in highways. Five well-confined circular RC columns were tested under lateral loads in this experimental study.

The bridge column specimens varied with respect to their shear span to depth ratios and longitudinal reinforcement ratios. The test results were evaluated in terms of the lateral load capacity and load-displacement response characteristics of the specimens tested.

1.3. Objectives and Scope

The seismic response of RC columns has already been investigated by numerous researchers. Various analytical models have also been proposed to simulate the experimentally-observed response characteristics of RC columns. However, most of the experimental studies and analytical modeling approaches available in the literature focus on the effect of only a specific parameter on the column response, such as amount or configuration of transverse reinforcement, aspect (or shear span to depth) ratio, or axial load level. However, validation of a generalized analytical model formulation for RC columns needs to be conducted not only under specific conditions related to geometry, material properties, reinforcement configuration, and loading, but also considering various combinations of these conditions. Therefore, there is still a need for a generalized, reliable, and widely-applicable modeling approach for simulating the nonlinear hysteretic response of RC columns with various configurations and response characteristics.

Analytically simulating important hysteretic behavioral characteristics, including lateral load capacity, deformation capacity, stiffness, pinching, and lateral load degradation of columns that exhibit either flexure-dominated or shear-controlled response characteristics (or failure modes), as well as shear-flexure interaction behavior, is the main objective of this study. Both well-designed columns and columns with inadequate transverse reinforcement and poor seismic details are investigated for this purpose. RC column test specimens which differentiate in terms of their cross-sectional geometry, aspect ratios, failure modes, levels of axial load, material properties, and loading protocols are considered in the analytical study. The model is extensively calibrated to represent the characteristics of the column specimens investigated, using the same calibration methodology applied for all specimens.

The model results are compared with the experimental observations, and the effectiveness of the model in simulating the lateral load behavior of columns with a wide range of response characteristics, is evaluated.

1.4. Thesis Outline

The focus of this thesis is successful simulation of the lateral load response of RC columns, irrespective of whether the response and failure mode is flexure-controlled, shear-controlled, or a combination of flexure and shear responses. To experimentally validate the finite element modeling modeling approach adopted in this study for RC columns, test programs during which both flexural and shear failures were observed on column specimens, were selected for model calibration and analysis. The model was calibrated and analyzed considering four different experimental programs selected from the literature. The column specimens tested during these experimental programs differentiated with respect their failure modes, cross-sectional geometries, shear span to depth ratios, reinforcement amount and detailing, levels of axial load, and lateral displacement histories.

Chapter 1 of this Thesis provides an introduction, a brief literature review, and the objective and scope of this study. Chapter 2 provides a description of the modeling approach adopted in this study for simulation of RC column behavior, including the constitutive model element and material models implemented, and the finite element model assembly procedure used. Chapter 3 presents details on calibration of the model for representing the characteristics of the test specimens investigated. Comparison of analytical model results with experimentally-measured column responses are presented in Chapter 4. Finally, the conclusions deducted from this study and recommendations for future research are provided in Chapter 5. The Appendix of this thesis presents local response predictions obtained from the analytical model for the column specimens investigated.

2. MODEL DESCRIPTION

2.1. Overview

In this chapter, the constitutive RC panel (membrane) model implemented in the two dimensional finite element modeling methodology adopted in this study is briefly described. Description of the constitutive material models that are used in the panel model formulation is also provided. The constitutive panel model formulation also incorporates, behavioral features including hysteretic biaxial damage and compression softening in concrete, shear stress transfer mechanisms across cracks, and strain localization effects, in order to simulate important response characteristics of reinforced concrete columns.

The constitutive panel model formulation called the Fixed-Strut-Angle Model (FSAM), originally proposed by Ulugtekin (2010), is implemented in finite element model. The main advantages of this panel model are its simplicity and accuracy. The model was developed by considering previous experimental and analytical studies which were conducted by various other researchers. The resulting panel model formulation was found to be reasonably accurate and feasible for implementation in a finite element model assembly. The formulation of FSAM is summarized in the following section.

2.2. Constitutive Panel Model

The original FSAM formulation (Ulugtekin, 2010) was developed with the assumption of perfect bond between reinforcing steel bars and concrete. Shear aggregate interlock effects and dowel action on reinforcing steel bars were also neglected. Perfect bond assumption relies on assuming an identical strain distribution between concrete and steel. Reinforcing steel model was adopted for uniaxial direction only, whereas constitute concrete model was adopted in biaxial directions. To simulate the biaxial stress-strain relationships for uncracked concrete (Figure 2.1), the Rotating Angle Strut and Tie Model formulation (Pang and Hsu, 1995) was used.

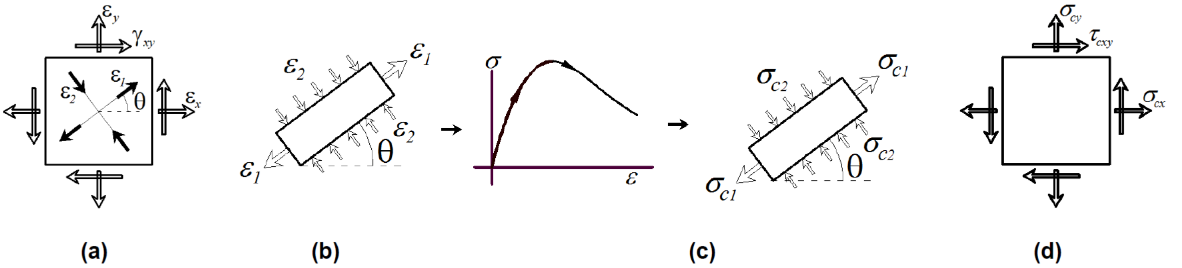

Figure 2.1. Behavior of uncracked concrete in the FSAM: (a) strain field, (b) principal strains; (c) principal stresses in concrete; (d) concrete stresses. (Kolozvari *et al.*, 2015)

The hysteretic behavior of uncracked concrete is defined monotonically up to the cracking strain for concrete. When the applied principal tensile strain first exceeds the concrete cracking strain, the first crack forms in the panel model, in perpendicular direction to the principal tensile strain. At this stage, the first “Fixed Strut” is assigned parallel to the principal tensile strain direction (Figure 2.2). For the next loading stages, principle strain directions can rotate with respect to the applied strain field; however, the principal compressive stress direction in concrete coincides with the first crack direction (the first ”Fixed Strut”). Since the principal concrete compressive stress and the crack direction are assumed to coincide, the model assumes that shear stresses do not develop along the crack direction.

Once the first crack is defined in the model, the applied strain field is transformed to parallel and perpendicular directions to the crack, and concrete stress values are calculated using the uniaxial stress-strain relationship adopted for concrete. The uniaxial concrete stresses calculated parallel and perpendicular to the crack direction are then modified (reduced) to incorporate biaxial behavior characteristics including compression softening and hysteretic biaxial damage.

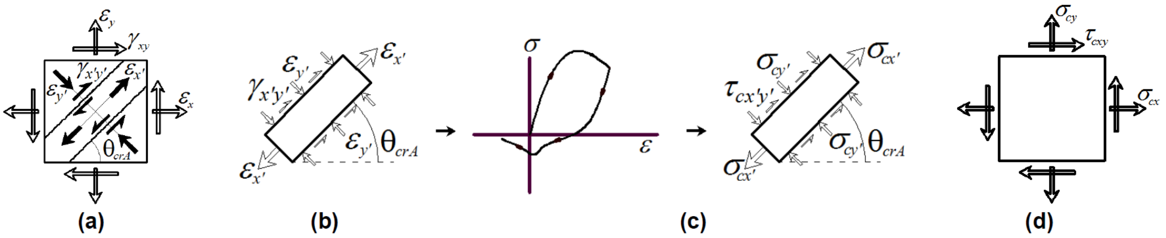

Figure 2.2. Behavior of concrete after formation of the first crack: (a) strain field; (b) concrete strut strains; (c) concrete strut stresses; and (d) concrete stresses (Kolozvari *et al.*, 2015)

The second crack in the FSAM forms under cyclic loading, when the tensile strain that along first strut direction exceeds the cracking strain of concrete. According to this methodology, the direction of the second crack is perpendicular to the first crack direction, which stems from the zero shear stress assumption along crack surfaces. The two struts are assumed perpendicular to each other, which is called the "orthogonal" crack modeling formulation. The second strut direction is parallel to the second crack direction, which is perpendicular to first crack direction. The first and second struts work under tension or compression, under positive or negative loading directions during cyclic loading. Although the concrete principal stress directions are constant along the fixed strut directions, the principal strains are able to rotate with respect to the applied strain field during loading. However, rather than using the principal strain values for calculating the principle stresses in concrete, the applied strain field is converted to strain components along the fixed strut directions. Concrete stresses are then calculated along these directions, using the uniaxial constitutive model adopted for concrete. Finally, the stresses are modified considering biaxial compression softening and hysteretic damage effects. The constitutive model adopted for reinforcing steel is applied along the orthogonal rebar directions, to obtain uniaxial stress values in reinforcing steel bars. Finally, smeared stresses on the panel element are calculated using superposition of stresses in concrete and reinforcing steel, also considering reinforcement ratios in the horizontal and vertical directions. More information on the FSAM can be found in the thesis by Ulugtekin (2010).

As described above, the original formulation of the FSAM (Ulugtekin, 2010) does not consider shear aggregate interlock effects between cracks (shear stresses developing along crack surfaces) and dowel action on reinforcing bars. Not considering these shear stress transfer mechanisms across cracks typically results in overestimation of shear strains along the crack surfaces. For that reason, Orakcal *et al.* (2012) improved the original model formulation by implementing a simple friction-based model to consider shear aggregate interlock effects on crack surfaces. Later, Gullu and Orakcal (2017) improved the FSAM formulation to better represent shear aggregate interlock behavior (considering frictional shear stress on cracks and clamping effects of reinforcement), and the dowel action on reinforcing steel bars, as described in the following paragraphs.

The original formulation of the FSAM, in which the aggregate interlock and the dowel action mechanisms are ignored, was later modified since the assumption that no shear stress transfer occurs across crack surface may lead to overestimation of shear deformations and prediction of premature sliding shear failures. To remedy this shortcoming of the original FSAM, Orakcal *et al.* (2012) proposed a simple friction-based elasto-plastic aggregate interlock model, generating sliding shear stresses on crack surfaces. In this interlock model, when the normal stress perpendicular to the crack surface is tensile, the sliding stress effect is assumed to be zero. When the normal stress perpendicular to the crack surface is compressive, the sliding shear stress is bounded by the product of that compressive stress and a shear friction coefficient. In the present model formulation, friction-based elasto-plastic aggregate interlock model was developed by implementation of a peak-oriented hysteretic model to describe the cyclic characteristics of the friction-based constitutive model for aggregate interlock (Figure 2.3(a)), where the unloading from the shear (friction) stress vs. shear (sliding) strain envelope follows the initial elastic stiffness (e.g., 0.4Ec), zero stress is maintained until the origin, and reloading to the envelope in the opposite direction is oriented towards the previous peak. In this interlock model, when the normal stress in concrete perpendicular to the crack surface is tensile, the sliding shear stress and stiffness are assumed to be zero as it was proposed in friction-based elasto-plastic model, whereas when the normal stress is compressive, the sliding shear stress is bounded by the product of that compressive stress and a shear friction coefficient (e.g., η_{fr}=0.5).

Clamping effect of the reinforcing steel bars on the shear aggregate interlock mechanism is also considered, in a similar manner to the shear-friction approach used in ACI 318, with the capacity calculated by multiplying the yield strength of the reinforcement perpendicular to crack surface with a clamping coefficient (e.g., η_{cl}=0.5). A peak-oriented hysteretic model is used also to describe the cyclic behavior of the clamping component of the shear aggregate interlock mechanism (Figure 2.3(b)). To represent the dowel action on the reinforcement, the elasto-plastic dowel action model proposed by He and Kwan (2001) is implemented as the monotonic envelope of the dowel force vs. shear strain constitutive relationship, and origin-oriented unloading and reloading rules are adopted to represent the hysteretic behavior (Figure 2.3(c)).

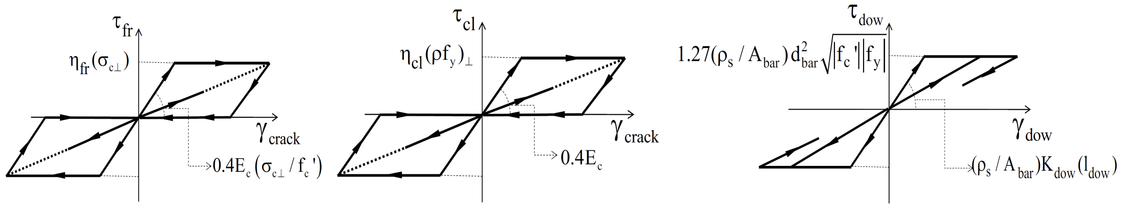

Figure 2.3. a) Peak-oriented hysteretic model for shear aggregate interlock b) Peak-oriented hysteretic model for clamping effect c) Origin-oriented hysteretic model for dowel action

2.3. Constitutive Material Models

2.3.1. Constitutive Model for Reinforcement

Cyclic stress-strain behavior of reinforcing steel is represented with the model proposed by Menegetto Pinto (1973) in the constitutive panel model formulation. This hysteretic material model was improved by Filippou *et al.* (1983) to capture influence of isotropic strain hardening. Bauschinger's effect is also represented in the model formulation, by considering cyclic degradation of tangent stiffness of the stress–strain curves in the unloading and reloading branches.

The Menegetto Pinto (1973) model is one of the most well-known nonlinear hysteretic relationships in the literature for reinforcing steel, due to its simplicity and accuracy. The model is illustrated in Figure 2.4.

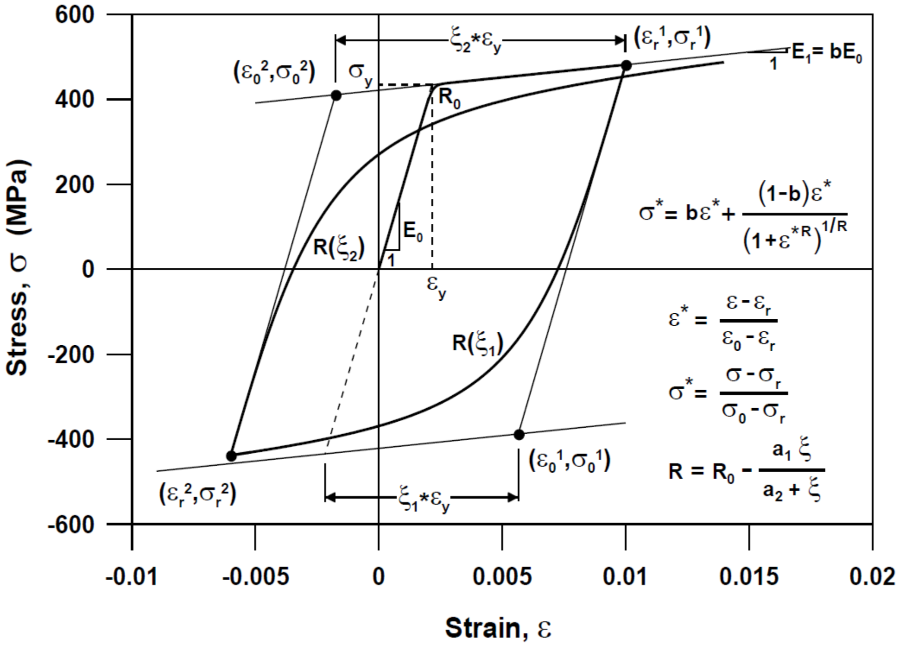

Figure 2.4. Constitutive Model for Steel (Menegetto and Pinto, 1973)

2.3.2. Constitutive Model for Concrete

The cyclic stress-strain behavior of concrete adopted in the panel model formulation is the hysteretic constitutive material model proposed by Chang and Mander (1994). Experimental validation of the model was done by various researchers. The model is able to simulate hysteretic behavior of both confined and unconfined concrete under cyclic tension and compression.

The Chang and Mander (1994) model implemented in the FSAM is modified by implementing compression softening effect (as proposed by Vecchio and Collins, 1993) and hysteretic biaxial damage effect (as proposed by Mansour *et al.*, 2002) into its formulation.

These improvements were made in order to simulate the behavioral characteristic of concrete subjected to biaxial loading, along the two perpendicular strut directions. Characteristics of the cyclic stress-strain relationship generated by the Chang and Mander (1994) model is depicted in Figure 2.5.

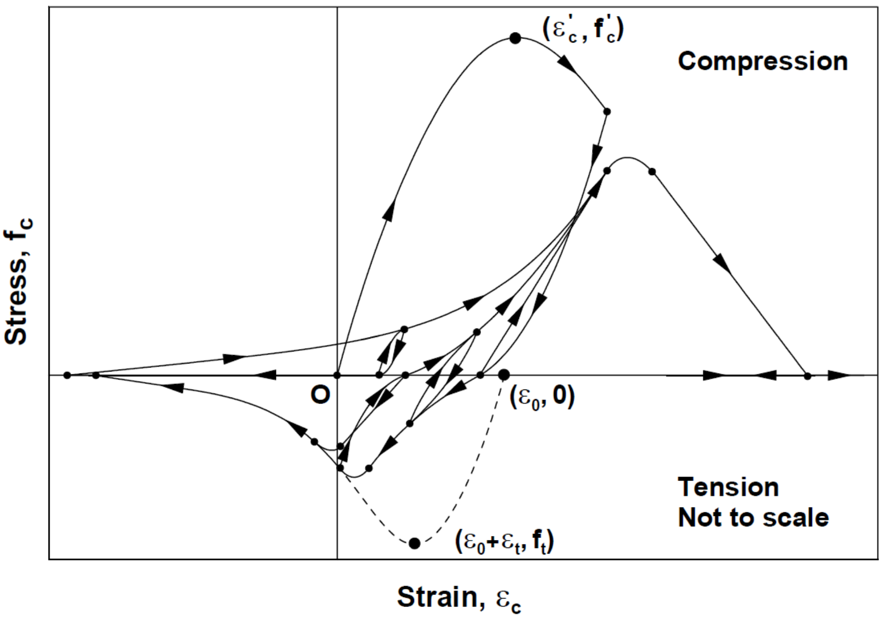

Figure 2.5. Constitutive Model for Concrete (Chang and Mander, 1994)

2.3.3. Strain Localization on Concrete

Studies on the strain localization phenomenon in nonlinear modeling methodologies generally focus on development of regularization techniques that consider material nonlinearity and strain energy, for reliable prediction of localization of deformations in nonlinear model elements, particularly during the degradation stage of load–deformation behavior. Within the scope of this phenomenon, Coleman and Spacone (2001) proposed a methodology that is applicable for constitutive steel and concrete models, to avoid modeling errors resulting from strain localization. This regularization technique basically involves modifying post-peak slope of stress-strain relationship while satisfying constant fracture energy, based on the volume (height in particular) of the nonlinear model element used.

The methodology was shown to provide reliable model results that are not overly sensitive to the element size, for displacement-based and force-based fiber model formulations. Maintaining fracture energy is illustrated at Figure 2.6. This methodology by Coleman and Spacone (2001) is adopted in the model formulation used this study for concrete, as a simple regularization approach to remedy the strain localization problem.

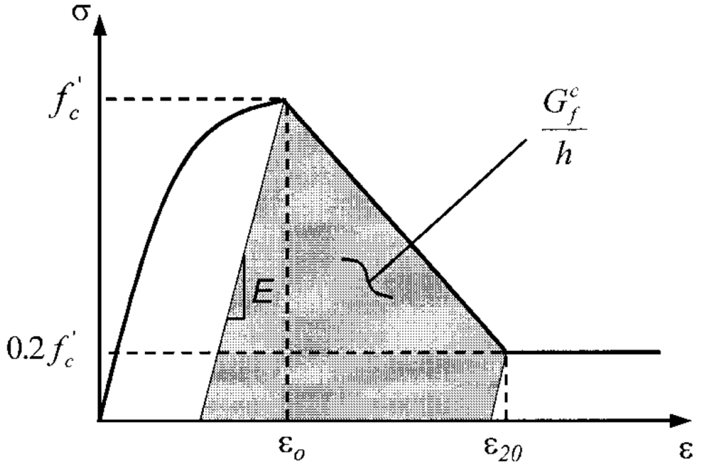

Figure 2.6. Stress-Strain Law and Compression Fracture Energy (Kent and Park, 1971)

2.3.4. Tension Stiffening on Reinforcing Steel

Within the scope of this study, it was debated whether or not the effect of tension stiffening on the stress–strain behavior of reinforcing steel bars should be considered. Experimental studies by Belarbi and Hsu (1994), as well as others, on reinforced concrete elements subjected to uniaxial tension have shown that the average yield strength and strain hardening ratio of reinforcing steel bars embedded in concrete can differ from those of bare bars, because of amplification of tensile strains at discrete crack locations. Belarbi and Hsu (1994) proposed empirical equations for modifying the effective yield strength and strain hardening ratio of bars surrounded by concrete, depending on the reinforcement ratio of a RC panel element subjected to tension.

Based tests on 17 full-size reinforced concrete panels, they proposed a revised stress – strain relationship for embedded steel bars, for which the yield strength of the average stress–strain curve of a bare bar reduces when the bar is embedded in concrete. Mansour *et al.* (2001) suggested a lower limit of 0.25% for reinforcement ratio, for this reduction in yield strength to be realistic. This approach was implemented in panel model formulation developed originally for structural walls, since each panel element in a wall model can be assumed to have a uniform reinforcement ratio in both horizontal and vertical directions.

However, in RC column cross sections, longitudinal reinforcing bars are not uniformly distributed, and the reinforcement ratio defined for each model element is very sensitive to discretization of the column cross-section in the model calibration Because of this reason, the effect of tension stiffening on the stress–strain behavior of reinforcing steel bars has been neglected in this study, since the scope of the present study is adaptation and validation of the model for RC columns.

2.4. Finite Element Methodology

The finite element model (FEM) formulation used in this study for assembly of the FSAM panel elements for constructing a RC column model, is described in this section. Four nodes, eight degree of freedom panel elements were assembled to simulate nonlinear response of relatively slender structural walls by Gullu (2013). According to this methodology, assembly of local and global stiffness matrices and resisting force vectors, as well as, formulation of support conditions and constraints are summarized in the following sections. More information on the FEM formulation can be found in the thesis by Gullu (2013).

2.4.1. 4 Nodes, 8 Degree of Freedom Rectangular Element

In the FEM formulation adopted, rectangular elements are used for modeling of RC structural columns. The rectangular elements are formulated as membrane (panel) elements, which means four node model elements were assembled in two dimensional space to formulate the FEM under only in plane loading conditions. Each membrane element has four nodes and each node has two degrees of freedom (DOF), which are in vertical and horizontal translational directions. In other words, rotational degrees of freedom are not defined at the nodes. The stress and strain values are obtained at the geometric centroid of each model elements (meaning one Gauss integration point per model element) for the sake of simplicity of the formulation. The numbering rule adopted for the local degrees of freedom on each model element is shown in Figure 2.7.

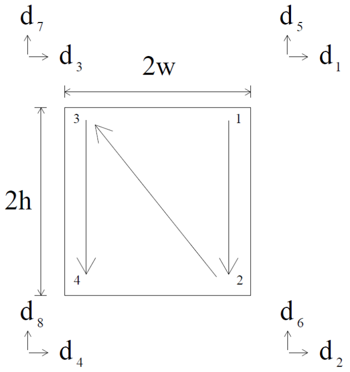

Figure 2.7. Local Nodes and DOFs in a Rectangular Model Element (Gullu, 2013)

Simple linear shape functions are used to obtain the in-plane strains, based on the displacement values along the nodal DOFs at the four nodes of each model element (Figure 2.8).

As shown in the following equations, strains were calculated at the centroid of each rectangular element, which means assigning zero values to parameters ξ and η.

Although more refined shape functions and more integration points per model element could have been used in the formulation of the FEM; this approach was selected to make the model formulation as simple as possible.

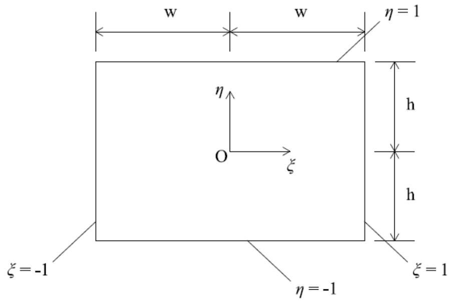

Figure 2.8. Normalized coordinates of a rectangular element.

$$N_1 = \frac{1}{4}(1+\xi)(1+\eta) \tag{2.1}$$

$$N_2 = \frac{1}{4}(1+\xi)(1-\eta) \tag{2.2}$$

$$N_3 = \frac{1}{4}(1-\xi)(1+\eta) \tag{2.3}$$

$$N_4 = \frac{1}{4}(1-\xi)(1-\eta) \tag{2.4}$$

Accordingly, after obtaining the deformations of the model elements (depending on the element degrees of freedom) at each increment of the loading history, the deformations can be transformed into the average strain values using Equation 2.5, Equation 2.6 and Equation 2.7.

The average strain values in the two dimensional model element are used as input strains for the constitutive FSAM panel model. Afterwards, the tangent stiffness matrix are obtained from the FSAM as illustrated in Figure 2.9.

$$\varepsilon_x = \frac{defx}{2w} \tag{2.5}$$

$$\varepsilon_y = \frac{defy}{2h} \tag{2.6}$$

$$\gamma_{xy} = \frac{defyx}{2h} + \frac{defxy}{2w} \tag{2.7}$$

$$\begin{Bmatrix} \varepsilon_x \\ \varepsilon_y \\ \gamma_{xy} \end{Bmatrix} \rightarrow \textbf{Fixed Strut Angle Panel Model (FSAM)} \rightarrow \begin{bmatrix} E_{11} & E_{12} & E_{13} \\ E_{21} & E_{22} & E_{23} \\ E_{31} & E_{32} & E_{33} \end{bmatrix}$$

Figure 2.9. Tangent Stiffness (Elasticity) Matrix Calculation Path (Gullu, 2013).

Multiplying the transpose of strain matrix $[G]^T$, the elasticity matrix $[E]$ and the strain matrix $[G]$, and then integrating along the element volume, provides the element local stiffness matrix for each model element.

$$[k] = \int_V [G]^T[E][G]dV = \int_V [G]^T[E][G]dxdydz \tag{2.8}$$

2.4.2. Finite Element Model Stiffness Assembly

After obtaining the local stiffness matrices for each model element, stiffness assembly operations are carried out. By superimposing the overlapping terms of the 8x8 local stiffness matrices, the global stiffness matrix is generated for the overall analytical model. A representative column is divided into m×n number of elements, and the numbering technique used for these elements is represented in Figure 2.10

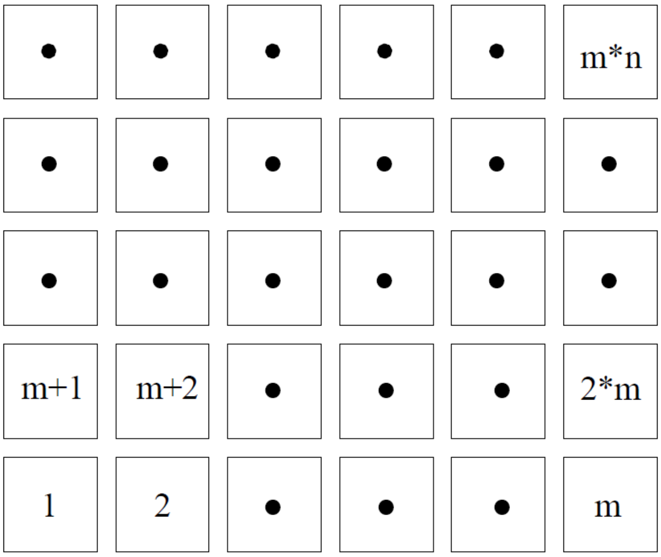

Figure 2.10. Numbering Technique Used For The FEM (Gullu, 2013)

An illustrative calculation for one term in the global stiffness matrix is shown in Equation 2.9. The superscripts in the equation represent the model element numbers, whereas the subscripts indicate the local stiffness parameters. All terms in global stiffness matrix are generated using a similar methodology.

$$[K]_{99} = [k]^{1}_{11} + [k]^{2}_{33} + [k]^{3}_{22} + [k]^{4}_{44} \tag{2.9}$$

2.4.3. Internal Force Vector Assembly

Assembling of the global internal force vector of the FEM is described in this section. The constitutive FSAM is used, as described in previous section, to generate stress values for each model element, corresponding to the average strain values applied on the model element.

$$\begin{Bmatrix}\varepsilon_{\mathrm{x}}\\ \varepsilon_{\mathrm{y}}\\ \gamma_{\mathrm{xy}}\end{Bmatrix} \rightarrow \text{Fixed Strut Angle Panel Model (FSAM)} \rightarrow \begin{Bmatrix}\sigma_{\mathrm{x}}\\ \sigma_{\mathrm{y}}\\ \tau_{\mathrm{xy}}\end{Bmatrix}$$

Figure 2.11. Stress Vector Calculation Path (Gullu, 2013).

The model element thickness and half of the vertical or horizontal width of the model element is multiplied with stress values generated from FSAM to calculate internal force parameters for each of the model elements. Numbering of force parameters is defined identically with the local displacement numbering pattern. In order to obtain the internal force vector for each element, the obtained stress values are used. At each increment of the applied loading history, the local internal force vectors are superimposed to generate global internal force vector for the FEM of a column.

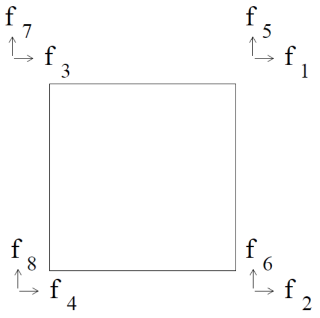

Figure 2.12. Numbering Technique of Internal Forces For a Mesh (Gullu, 2013).

Accordingly, the internal force component numbering methodology is shown in Figure 2.12. Each of the term of the global internal force vector can be calculated as representatively shown in Equation 2.9. Superscripts are used to represent model element numbers whereas subscripts are used to describe the components of the force vector for each model element.

$$\{F\}_{91} = \{f\}^1_{11} + \{f\}^2_{31} + \{f\}^3_{21} + \{f\}^4_{41} \tag{2.10}$$

2.4.4. Support Conditions and Constraints

The reinforced concrete column specimens investigated in this study for validation of the model were fixed, using a pedestal, to a strong floor, as is typical in column tests. In the model, the nodal displacements in horizontal and vertical directions were therefore assumed to be zero at the supports. The support reactions predicted by the model can be calculated from the internal forces developing at the support degrees of freedom.

In order to simulate the test setup characteristics into the model, a rigid body constraint was also defined in the model formulation. At the elevation where the columns are subjected to axial and lateral loads, a rigid body constraint is defined on the model degrees of freedom (along a horizontal line), so that the applied loads can be more uniformly distributed across the column cross section. The body constraint is typically assigned at the top of the column specimens, where lateral and axial loads are applied during the analysis (Figure 2.13).

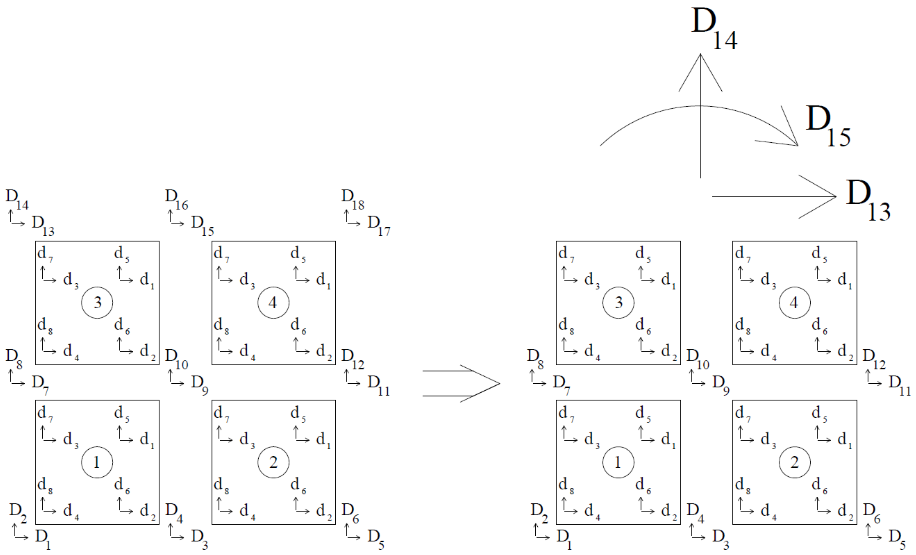

Figure 2.13. Body Constraints Assignment For a Model (Gullu, 2013).

2.4.5. Nonlinear Analysis Solution Strategy

A brief overview of the nonlinear analysis solution strategy used in this study is presented in this section. An iterative solution strategy (Clarke and Hancock, 1990; Simons and Powell, 1982) was used for conducting nonlinear analysis of RC columns using the finite element modeling methodology adopted. First, depending on an applied displacement field (not necessarily satisfying equilibrium), the global stiffness matrix and internal force vector of the model are assembled from the model elements, as described in the previous section. Support conditions and rigid body constraints are assigned to the model formulation. Afterwards, the iterative nonlinear analysis solution strategy proposed by Clarke and Hancock (1990) and, Simons and Powell (1982) is adopted to reach equilibrium conditions during each loading step of the analysis. The displacement-controlled solution strategy selected for the analysis is very suitable for simulating displacement-controlled (or drift-controlled) cyclic lateral load tests conducted on the RC column specimens investigated.

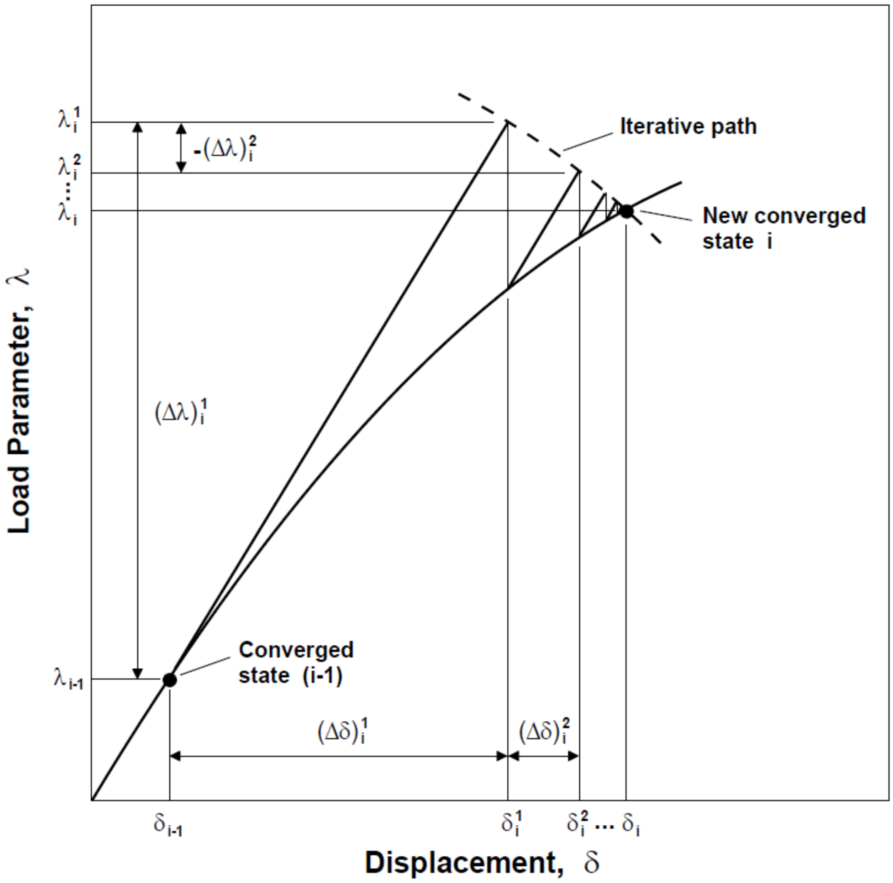

Figure 2.14. Representation of the nonlinear analysis solution strategy for a single degree of freedom system (Clarke and Hancock, 1990).

In this solution strategy, a target displacement (applied during testing of a column specimen) is assigned to the model along a particular degree of freedom, and solution strategy iterates the displacements along all degrees of freedom of the model (while the target displacement along the specified DOF is kept constant), until the equilibrium equations (the internal and external forces being equal along all DOFs) are satisfied within a small margin of error. A detailed description of the nonlinear analysis solution strategy is presented in the thesis by Gullu (2013). The solution strategy is illustrated in Figures 2.14 and 2.15.

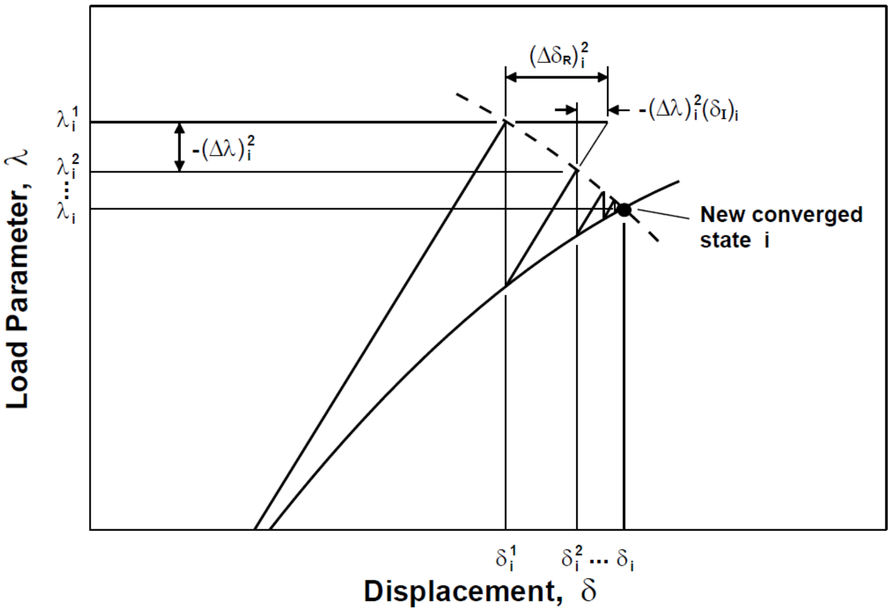

Figure 2.15. Iterative Strategy and Residual Displacements (Clarke and Hancock, 1990).

3. EXPERIMENTAL CALIBRATION OF THE MODEL FOR COLUMN SPECIMENS

In this chapter, details of the test specimens including properties of materials, test setup procedures, and loading conditions were briefly summarized. Calibration procedure for each specimens was described in detail for the concrete and steel material models. Contribution of strain localization to the calibration of concrete model and rotational spring implementation were also described. With the calibrated material parameters and calibration of the analytical model for column geometry, analysis of selected column specimens were performed in Matlab to validate the analytical model. For the calibration and validation, five specimens from Lynn (2001), three specimens from Sezen and Moehle (2002), two specimens from Benzoni and Priestley (1996), and finally two specimens from Shanmugam (2009) were used within the scope of this study.

3.1. Description of the Column Specimens

3.1.1. Lynn (2001) Specimens

The test program conducted by Lynn (2001) was aimed to simulate the behavior of columns which were built before 1970's in West Coast U.S.A. Within the scope of this experimental program, eight rectangular columns with identical geometries, different reinforcement configurations, and varying axial load levels were tested.

The motivation of this test program was to evaluate the shear strength and lateral load capacity of existing columns. Reinforcement configuration were differentiated by the spacing of transverse reinforcement and longitudinal reinforcement ratios. Two types of confinement configurations, which were rectangular and diamond shape ties, were used in the test specimens. Naming of test specimens is presented in Figure 3.1.

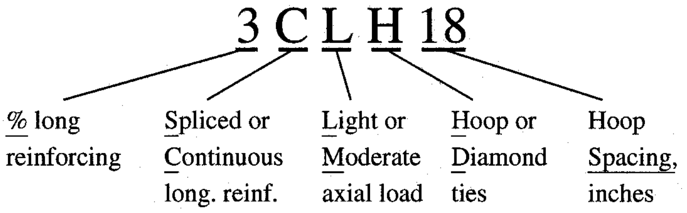

Figure 3.1. Naming of Specimens (Lynn, 2001).

The first number in the specimen name represents longitudinal reinforcement ratio (2% or 3%), the following first letter indicates the configuration of column reinforcement, whether it is lap spliced (S) or continuous (C). The second letter indicates the axial load level whether it is light (L) or moderate (M), whereas configuration of transverse reinforcement is represented by last letter, which is either diamond shaped (D) or hoop (rectangular) ties (H). Finally, last two numbers represent the hoop spacing in units of inches.

The analytical model is not capable of simulating the hysteretic response of column specimens with inadequate lap-splices on the longitudinal reinforcement. Since three of eight column specimens were constructed with lap-spliced reinforcement configuration, five of column specimens tested by Lynn (2001) were used to verify the analytical model. The effects of longitudinal reinforcement ratio, axial load level, and spacing of transverse reinforcement, as well as flexural or shear controlled column failure modes were experimentally investigated by the use of these five test specimens. The geometry of the specimens as well as longitudinal and transverse reinforcement configurations are summarized in Table 3.1.

A representative figure for the geometry and reinforcement details of one of the five columns specimens used for validation of the model is presented in Figure 3.2. The dimensions of square-shaped cross-section was 457 mm and the column the height was 2946 mm.

Table 3.1. Test Specimen Details for Lynn (2001)

Specimen	**Depth**	**Width**	**Height**	**Spacing**	**Longitudinal Reinforcement**		**Transverse Reinforcement**	
	(mm)	(mm)	(mm)	(mm)	Diameter (mm)	ρ (%)	Diameter (mm)	ρ (%)
2CLH18	457.2	457.2	2946	457.2	25	1.94	9.5	0.07
3CLH18	457.2	457.2	2946	457.2	32	3.03	9.5	0.07
2CMH18	457.2	457.2	2946	457.2	25	1.94	9.5	0.07
3CMH18	457.2	457.2	2946	457.2	32	3.03	9.5	0.07
3CMD12	457.2	457.2	2946	304.8	32	3.03	9.5	0.17

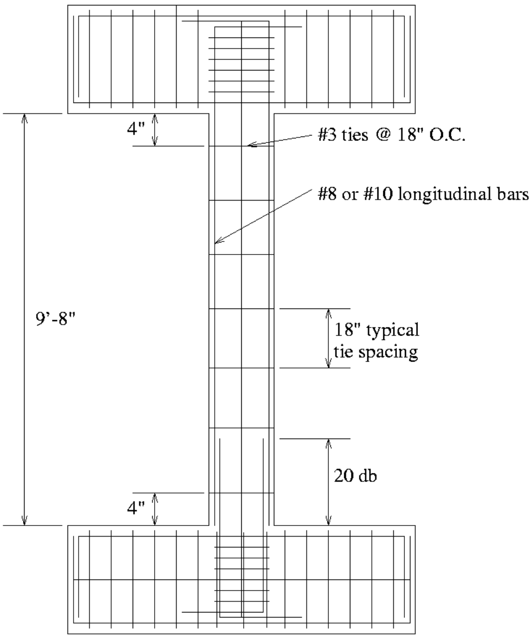

Figure 3.2. Typical Column Test Specimen (Lynn, 2001).

Longitudinal reinforcement with 25 mm (#8) or 32 mm (#10) diameter was used with different longitudinal reinforcing ratio and transverse reinforcement of 9.5 (#3) mm were used in test specimens. Clear cover of concrete was approximately 32 mm for all columns. Diamond-shaped or hoop ties with 90 degree hooks had spacing of 457 mm or 305 mm, as represented by last two numbers in the names of test specimens (Figure 3.3). Grade of longitudinal and transverse reinforcement bars was Grade 40, whereas and the modulus of elasticity of reinforcements was assumed to be 200 GPa.

Average yield stress values of longitudinal (25mm or 32mm) and transverse reinforcement bars were 331 MPa and 400 MPa, and ultimate stress values were 500 MPa and 565 MPa, respectively. Compressive strength of concrete was obtained from compression tests of cylindrical concrete specimens on the test day. More detailed information for these test specimens are available in Ph.D. Dissertation by Lynn (2001).

Table 3.2. Level of Axial Loads for Lynn (2001) Specimens

Specimen	f'_c	P_{ax}	$P_{ax}/A_g f'_c$
	(Mpa)	(kN)	(%)
2CLH18	33.07	518.8	12
3CLH18	26.89	518.8	12
2CMH18	27.65	1512.4	35
3CMH18	25.75	1512.4	35
3CMD12	25.75	1512.4	35

Loading setup of the test specimens imposed zero rotation at top and bottom pedestals of the columns, creating a double curvature loading condition to simulate the actual loading conditions of columns in buildings. Vertical actuators were used to provide constant axial load and zero top rotation, whereas a horizontal actuator with a line of action along the mid-height of the specimens was used to apply cyclic lateral loading. Axial load levels applied on the test specimens are presented in Table 3.2.

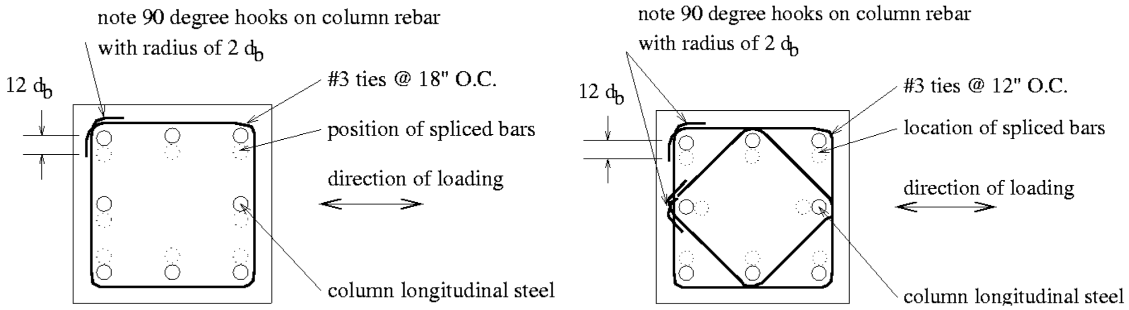

Figure 3.3. Cross Section of The Specimens (Lynn, 2001).

3.1.2. Sezen and Moehle (2002) Specimens

Sezen and Moehle (2002) conducted an experimental study to identify main factors influencing shear and shear-flexure interaction failure under different axial load levels, for columns with insufficient shear confinement and inadequate confinement. Four full-scale column specimens were tested within the scope of this experimental study. Based on test results, the authors proposed an empirical shear strength model, which relates shear strength to flexural ductility. Table 3.3 summarizes the details of test specimens investigated in this experimental program.

Table 3.3. Test Specimen Details for Sezen and Moehle (2002)

Specimen	**Depth**	**Width**	**Height**	**Spacing**	**Longitudinal Reinforcement**		**Transverse Reinforcement**	
	(mm)	(mm)	(mm)	(mm)	Diameter (mm)	ρ (%)	Diameter (mm)	ρ (%)
Specimen No:1	457.2	457.2	2946	304.8	29	2.47	9.5	0.17
Specimen No:2	457.2	457.2	2946	304:8	29	2.47	9.5	0.17
Specimen No:4	457.2	457.2	2946	304.8	29	2.47	9.5	0.17

Specimens were classified by different displacement histories and axial load levels. Specimens No. 1 and 2 were tested under 15% and 60% of axial load capacities, respectively. Specimen 4 was subjected to additional lateral displacements after reaching the target drift level, in order to observe whether the lateral load capacity of the specimen remains constant or not. Since Specimen 3 was tested under varying axial load, it was not used for validation of the analytical model adopted in this study. Within the scope of this thesis, specimens that were tested under only constant axial load levels were selected for model validation.

Similar to the test specimens by Lynn (2001), column dimensions were identical for all test specimens. The cross-sectional dimension of the square shaped specimens was 457 mm (Figure 3.5). Column clear height was 2946 mm and the clear cover was approximately 50 mm (Figure 3.4). Test specimens were identically reinforced in both transverse and longitudinal directions.

Average yield stress values of longitudinal (29 mm or 32 mm) and transverse (9.5 mm) reinforcing bars were 434 MPa and 476 MPa, and ultimate stress values were 645 MPa and 724 MPa, respectively.

Concrete compressive strengths that were obtained on the test day were approximately equal. Concrete strength and axial load levels of the specimens are listed in Table 3.4.

Table 3.4. Level of Axial Loads for Sezen and Moehle (2002) Test Specimens

Specimen	f'_c	P_{ax}	$P_{ax}/A_g f'_c$
	(Mpa)	(kN)	%
Specimen No:1	21.10	667	15
Specimen No:2	21.10	2670	60
Specimen No:4	21.79	667	15

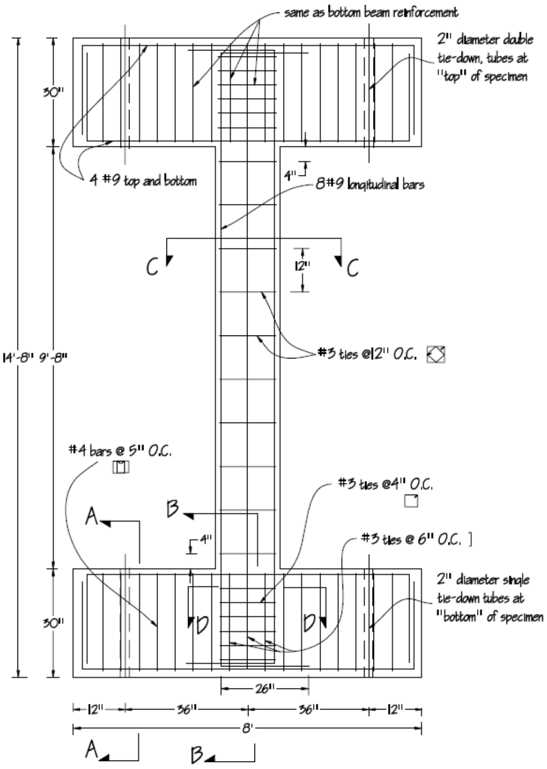

Figure 3.4. Column Geometry and Reinforcement for Test Specimens (Sezen and Moehle, 2002)

Two vertical actuators and one horizontal actuator were used in the test setup. The vertical ones were pin connected to top and bottom pedestals and enforced constant axial load and zero rotation at the top. All of the specimens were tested under double curvature loading condition, and the lateral load was applied along the mid-height of the specimens, similarly to the test setup by Lynn (2001).

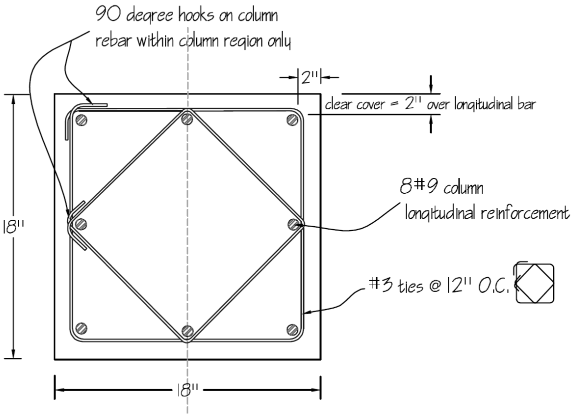

Figure 3.5. Cross Section of Test Specimens (Sezen and Moehle, 2002).

3.1.3. Priestley and Benzoni (1996) Specimens

Priestley and Benzoni (1996) tested two large-scale circular column specimens to investigate the seismic performance of columns designed according to lower limit of longitudinal reinforcement that is recommended by ACI 318 provisions. The first specimen was designed with the longitudinal reinforcement ratio of 0.5%, which was half of the lower limit specified in the code. The researchers expected to observe the influence of lower longitudinal reinforcement ratio on the ductile flexural response of columns. The second specimen was reinforced with longitudinal reinforcement ratio of 1.0% satisfying the ACI318 minimum requirements. However, the transverse reinforcement spacing was varied to observe the relationship between longitudinal steel ratio and shear strength.

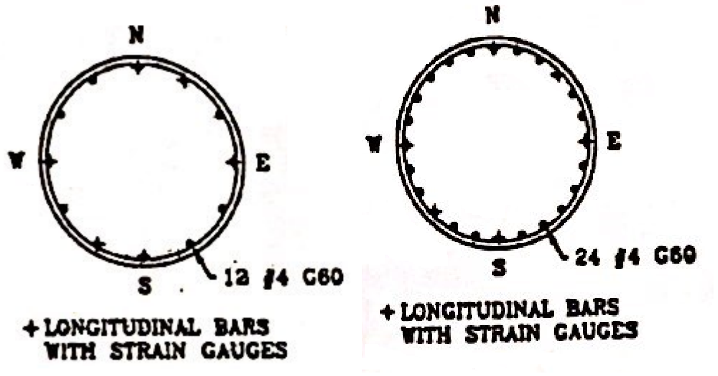

Figure 3.6. Cross Section of Test Specimens (Priestley and Benzoni, 1996).

The diameter and height of both column specimens were 610 mm and 1829 mm, respectively. For the first specimen, 12–#4 (12.7mm) reinforcing bars in longitudinal direction and #2 rebars (6.4mm) in transverse direction were used. For the second specimen, the number of the longitudinal reinforcing bars was increased to twice of the first specimen, which is equal to 24–#4 reinforcing bars. As well as the spacing of transverse hoops bars were decreased in the second specimen. Details of the geometry and reinforcement configuration for these test specimens are summarized in Table 3.5. The aim of the researchers was to increase the flexural capacity while decreasing the shear capacity of the second test specimen, to obtain specimen that is more susceptible to failing in shear.

Table 3.5. Details of Test of Specimens (Priestley and Benzoni, 1996)

Specimen	**Diameter**	**Height**	**Spacing**	**Longitudinal Reinforcement**		**Transverse Reinforcement**	
	(mm)	(mm)	(mm)	Diameter (mm)	ρ (%)	Diameter (mm)	ρ (%)
Column 1	610	1830	76.2	12.7	0.5	6.35	0.30
Column 2	610	1830	127	12.7	1.0	6.35	0.18

The yield stress was 462 MPa for the longitudinal bars and 361 MPa for the transverse hoops. Compressive strength for concrete was 30 MPa for both column specimens.

Since steel stress-strain relationships were not presented in the study by Priestley and Benzoni (1996), a reasonable strain hardening ratio was assumed in modeling of these columns.

Both the columns were loaded under axial load levels of approximately 6% $A_g f'_c$ (Table 3.6). A double-curvature loading setup with three actuators was used, similarly to the tests by Lynn (2001) and Sezen and Moehle (2002).

Table 3.6. Level of Axial Loads for Priestley and Benzoni (1996) Test Specimens

Specimen	f'_c	P_{ax}	$P_{ax}/A_g f'_c$
	(Mpa)	(kN)	%
Column 1	30	503	5.7
Column 2	30	503	5.7

3.1.4. Shanmugam (2009) Specimens

The test program conducted by Shanmugam (2009) was carried out to identify the seismic response of the bridge columns under combined loadings in terms of bending moment, torsional moment, axial and shear forces. In this thesis, specimens named as H/D(6)- T/M(0.0)/0.73 and H/D(3)-T/M(0.0)/1.32, which were tested under uni-directional bending moment were analytically investigated. In naming of these specimens, H/D represents the aspect ratio, whereas T/M represents the ratio of torsional moment (T) to bending moment (M), which when equal to zero means the section was subjected to pure bending moment. Lastly, the value at the end of naming indicates the transverse reinforcement ratios of the test specimen. Table 3.7 presents the geometric and reinforcement configuration details of the selected test specimens by Shanmugam (2009). The diameter of the both column specimens were 610 mm, but column heights were 1830 mm and 3660 mm, resulting in aspect ratios of 3 and 6. Concrete compressive strength was 34 MPa for both column specimens. Longitudinal reinforcement amounts were identical for the two specimens.

Transverse reinforcement diameters for specimen H/D(3)- T/M(0.0)/1.32 was equal to 12.7 mm, whereas for specimen H/D(6)-T/M(0.0)/0.73, it was equal to 9.5 mm.

Table 3.7. Details of Shanmugam (2009) Test Specimens

Specimen	**Diameter**	**Height**	**Spacing**	**Longitudinal Reinforcement**		**Transverse Reinforcement**	
	(mm)	(mm)	(mm)	Diameter (mm)	ρ (%)	Diameter (mm)	ρ (%)
H/D(3)-T/M(0.0)/1.32%	610	1830	70	25	2.0	12.7	1.32
H/D(6)-T/M(0.0)/0.73%	610	3660	70	25	2.0	9.5	0.73

Axial load levels of both column specimens were approximately 7% $A_g f'_c$ as shown in Table 3.8. The two column specimens tested by Shanmugam (2009) had a different test setup from other test specimens investigated in this thesis. Loading was applied at the top rather than the mid-height of test specimens, with no zero rotation restraint at the top, creating a single curvature (cantilever) loading condition.

Table 3.8. Level of Axial Loads for Shanmugam (2009) Specimens

Specimen	f'_c	P_{ax}	$P_{ax}/A_g f'_c$
	(Mpa)	(kN)	%
H/D(3)-T/M(0.0)/1.32	34	592	6.7
H/D(6)-T/M(0.0)/0.73	34	592	6.7

3.2. Calibration of Specimens

3.2.1. Mesh Discretization

The analytically model geometry was calibrated to represent the geometry of the column specimens investigated. The finite element column models were discretized using a number of meshes (model elements) along the longitudinal and horizontal directions. The number of meshes to be used along the height and cross section of the column specimens were selected a constant aspect (height to width) ratio (approximately 4) for each of the specimens modeled.

Following the assignment of meshes to the analytical model, reinforcement ratios for both horizontal and longitudinal directions were calculated considering the whether the elements incorporate longitudinal reinforcing bars or not. Since longitudinal reinforcement of RC column sections, is not uniformly distributed, some elements used along the middle regions of the column cross-section may not incorporate longitudinal reinforcing bars (Figure 3.7). For elements that do incorporate longitudinal bars, the horizontal length of the elements were determined using Equation 3.1:

$$x = \phi_y + 2\phi_x \tag{3.1}$$

where x is the length of the element that incorporates a longitudinal reinforcing bar, ϕ_y is the longitudinal reinforcing bar diameter and ϕ_x is the transverse reinforcing bar diameter. The remaining part of the column cross section (with no longitudinal bars) were divided into approximately equal widths.

Reinforcement ratios were defined by dividing the total longitudinal and transverse reinforcement areas with related cross sectional (horizontal and vertical) areas. Diamond-shaped transverse reinforcement areas were transformed into the loading direction in defining the transverse reinforcement ratios.

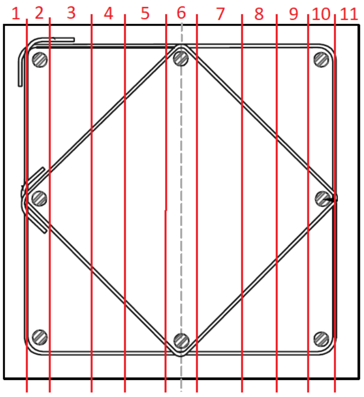

Figure 3.7. Mesh Discretization for Rectangular Cross-Sections (Sezen, 2002).

Mesh discretization for circular cross sections differs from rectangular cross sections due to geometry. For column specimens with rectangular cross sections, the criteria used was to more or less equalize the horizontal length of the model elements along the column cross section. However, for columns with circular cross sections, the dimension of the cross-section perpendicular to the loading direction varies from to center of the column cross section to the edge, due to the circular cross-section geometry (Figure 3.8). This results in significant difference between the areas of the model elements as well as significant difference between the reinforcing ratios of each model element, although the longitudinal reinforcement is uniformly distributed along the circular cross-section. Hence, for columns with circular cross section, the cross-sectional areas of the model elements were kept more or less equal, instead of equalizing the horizontal length distance of the model elements. Accordingly, the horizontal length of the model elements located at the sides of a circular column cross section were larger than the horizontal length of the center elements, in order to obtain approximately equal longitudinal reinforcement ratios among the elements. Following the definition of element sizes and longitudinal reinforcement ratios, transverse reinforcement ratios were calculated by dividing the area of transverse reinforcement in each model element to the vertical element area, and projecting it to the loading direction.

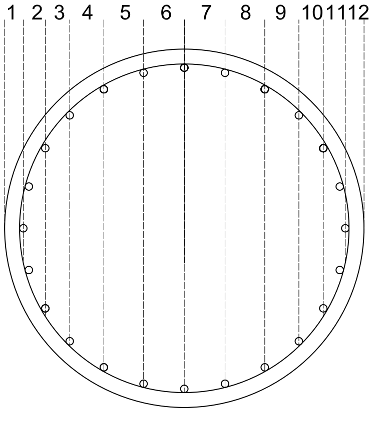

Figure 3.8. Mesh Discretization for Circular Cross-Sections.

In this study, column specimens with rectangular cross sections were defined with 11 elements along the cross section and 8 elements along the shear span of the columns, whereas column specimens with circular cross sections were defined with 12 elements along the cross section and again 8 elements along the shear span (Figure 3.7 and 3.8). However, one of exceptions is that specimen H/D(6)-T/M(0.0)/0.73% was discretized into 16 elements along its height, because its height (and shear span) was twice that of the other specimens. Also, Priestley specimens were discretized into 4 elements along its height, similarly because its shear span two depth ratio was half of the other specimens.

3.2.2. Calibration of Material Parameters

3.2.2.1. Concrete in Compression. Chang and Mander (1994) have proposed empirical relationships for unconfined and confined concrete, based on results of experimental studies. According to their empirical equations, initial modulus of elasticity for unconfined concrete E_c, can be calculated using Equation 3.2. The parameter ε'_c represents strain at peak stress (compressive strength) and it can be calculated using Equation 3.3. Finally, r is the shape parameter of the envelope curve for unconfined concrete in compression and ${f'}_c$ is characteristic compressive strength for concrete with units of MPa.

$$E_c = 8200\, {f'}_c^{(3/8)} \tag{3.2}$$

$$\varepsilon'_c = \frac{{f'}_c^{(1/4)}}{28} \tag{3.3}$$

$$r = \frac{{f'}_c}{5.2} - 1.9 \tag{3.4}$$

Calibration of non-dimensional parameters x_{crn} and x_{crp} were conducted by the comparison of envelope curves of Chang and Mander (1994) and Saatcioglu and Razvi (1992) constitutive models. x_{crn} is the parameter that define the post-peak slope of stress strain curve for concrete in compression which starts from peak compressive stress to spalling strain. x_{crp} is non- linear tensile strain used to define the tension envelope curve. Calibrated parameters of unconfined concrete material for all column specimens are summarized in Table 3.9.

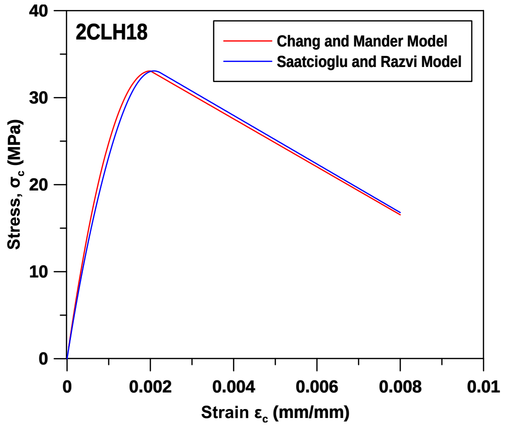

Figure 3.9. Unconfined concrete stress strain curve under compression for specimen 2CLH18 (Lynn, 2001)

Table 3.9. Calibrated Parameters for Unconfined Concrete in Compression

Specimen	f'_c	E_c	ε'_c	r	x_{crn}
	(Mpa)	(Mpa)	(mm/mm)	-	-
2CLH18	33.07	30450	0.002085	4.46	1.078
3CLH18	26.89	28178	0.001980	3.27	1.118
2CMH18	27.65	28476	0.001994	3.42	1.110
3CMH18	25.75	27722	0.001959	3.05	1.129
3CMD12	25.75	27722	0.001959	3.05	1.129
Specimen No:1	21.10	25728	0.001864	2.16	1.225
Specimen No:2	21.10	25728	0.001864	2.16	1.225
Specimen No:4	21.79	26040	0.001879	2.29	1.205
Column 1	30	29359	0.002035	3.87	1.092
Column 2	30	29359	0.002035	3.87	1.092
H/D(3)-T/M(0.0)/1.32%	34	30769	0.002100	4.64	1.074
H/D(6)-T/M(0.0)/0.73%	34	30769	0.002100	4.64	1.074

3.2.2.2. Concrete in Tension. Belarbi and Hsu (1994) developed constitutive model for the tensile stress strain relationship of concrete (Figure 3.10). According to model,

$$\text{If} \quad \varepsilon_c \leq \varepsilon_{cr} \qquad \text{Then} \quad \sigma_c = E_c\, \varepsilon_c \tag{3.5}$$

$$\text{If} \quad \varepsilon_c \geq \varepsilon_{cr} \qquad \text{Then} \quad \sigma_c = f_{cr} \left(\frac{\varepsilon_{cr}}{\varepsilon_c} \right)^{0.4} \tag{3.6}$$

where

$$E_c = 3875\sqrt{f'_c} \tag{3.7}$$

$$f_{cr} = 0.31\sqrt{f'_c} \tag{3.8}$$

$$\varepsilon_{cr} = 0.00008 \tag{3.9}$$

In these equation, E_c is Young's modulus of the average stress strain relationship, f_{cr} is tensile cracking stress and f_{cr} is the strain value corresponds to the tensile cracking stress. Units in the equations are in terms of Mpa.

The value of ε_{cr} was defined as 0.00008 according to recommendation by Belarbi and Hsu (1994) based on experimental program that was conducted on RC panels. Accordingly, parameters defining the tension envelope of the Chang and Mander (1994) model were calibrated to match the tensile stress-strain relationship proposed by Belarbi and Hsu (1994), as shown in Figure 3.10. The calibrated parameters of the Chang and Mander (1994) model are listed for each column specimen as listed in Table 3.10.

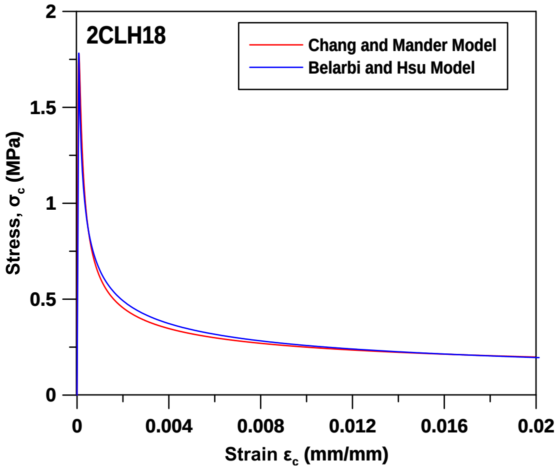

Figure 3.10. Unconfined concrete stress strain curve under tension for specimen 2CLH18 (Lynn, 2001)

Table 3.10. Calibration Parameters for Unconfined Concrete in Tension.

Specimen	f_{cr}	E_c	ε_{cr}	r_t	x_{crp}
	(Mpa)	(Mpa)	(mm/mm)	-	-
2CLH18	1.78	30450	0.00008	1.25	10000
3CLH18	1.61	28178	0.00008	1.26	10000
2CMH18	1.63	28476	0.00008	1.26	10000
3CMH18	1.57	27722	0.00008	1.26	10000
3CMD12	1.57	27722	0.00008	1.26	10000
Specimen No:1	1.42	25728	0.00008	1.26	10000
Specimen No:2	1.42	25728	0.00008	1.26	10000
Specimen No:4	1.45	26040	0.00008	1.26	10000
Column 1	1.70	29359	0.00008	1.25	10000
Column 2	1.70	29359	0.00008	1.25	10000
H/D(3)-T/M(0.0)/1.32%	1.81	30769	0.00008	1.25	10000
H/D(6)-T/M(0.0)/0.73%	1.81	30769	0.00008	1.25	10000

3.2.2.3. Confined Concrete. Formulation of the compressive envelope of confined concrete in the Chang and Mander (1994) model was calibrated to be compatible with the confinement model proposed by Mander *et al.* (1988a). The confinement model is applicable for reinforced concrete columns with either circular or rectangular cross sections.

In the confinement model by Mander *et al.* (1998a) for rectangular sections, effectively confined area A_e can be calculated using Equation(3.10)

$$A_e = \left(b_c d_c - \sum_{i=1}^{n} \frac{{w'}_i^2}{6} \right) \left(1 - 0.5 \frac{s'}{b_c} \right) \left(1 - 0.5 \frac{s'}{d_c} \right) \tag{3.10}$$

Parameters used in Equation 3.10 is given at Figure 3.11 and the core concrete area is defined using Equation 3.11.

$$A_{cc} = b_c \, d_c - A_{st} \tag{3.11}$$

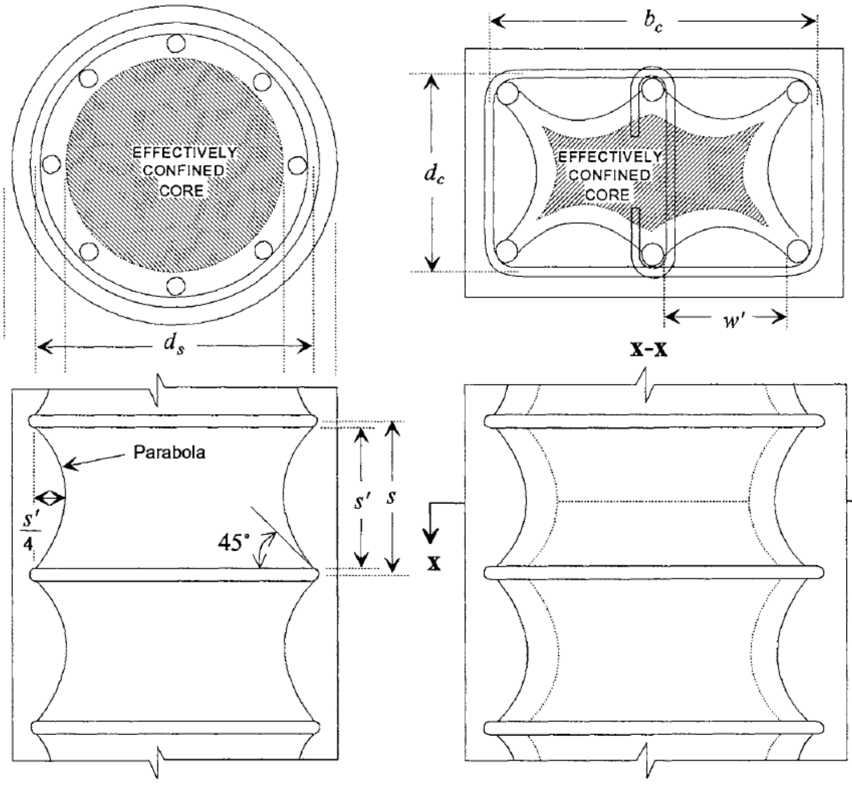

Figure 3.11. Confinement Mechanism for Circular and Rectangular Cross Sections (Chang and Mander, 1994)

Lateral confinement pressure values ${f'}_l$ are different in each direction, and are defined as:

$$f'_{lx} = k_e \, \rho_x \, f_{yh} \tag{3.12}$$

$$f'_{ly} = k_e \, \rho_y \, f_{yh} \tag{3.13}$$

in which confinement effectiveness coefficient is obtained by:

$$k_e = \frac{A_e}{A_{cc}} \tag{3.14}$$

and the transverse reinforcement ratio parallel to the x axis is given by:

$$\rho_x = \frac{A_{sx}}{s \, d_c} \tag{3.15}$$

and transverse reinforcement ratio parallel to the y axis is given by:

$$\rho_y = \frac{A_{sy}}{s \, b_c} \tag{3.16}$$

Finally, lateral confinement pressure can be found using Equation 3.17:

$$f_l = \frac{{f'}_{lx} + {f'}_{ly}}{2} \tag{3.17}$$

K is the coefficient that represents approximate analytical confinement ratio to ultimate strength, and it can be calculated using Equation 3.18:

$$K = \frac{{f'}_{cc}}{{f'}_c} = 1 + A\bar{x} \left(0.1 + \frac{0.9}{1 + B\bar{x}} \right) \tag{3.18}$$

$$\bar{x} = \frac{f'_{lx} + f'_{ly}}{f'_c} \tag{3.19}$$

$$r = \frac{min(f'_{lx}; f'_{ly})}{max(f'_{lx}; f'_{ly})} \tag{3.20}$$

$$A = 6.8886 - (0.6096 + 17.275\, r)e^{(-4.989\, r)} \tag{3.21}$$

$$B = \frac{4.5}{\frac{5}{A}\left(0.9849 - 0.6306e^{(-3.8389\, r)}\right) - 0.1} \tag{3.22}$$

Equation 3.18 can be also rewritten as follows:

$$f'_{cc} = f'_c + k_1 f'_l \tag{3.23}$$

where;

$$k_1 = A\left(0.1 + \frac{0.9}{1 + B\bar{x}}\right) \tag{3.24}$$

For the descending region of the stress-strain relationship, Richart *el al.* (1929) originally suggested

$$\varepsilon_{cc} = \varepsilon_{co}(1 + k_2\bar{x}) \tag{3.25}$$

with;

$$k_2 = 5\, k_1 \tag{3.26}$$

These two expression (Equation 3.25, Equation 3.26) adopted by Chang and Mander (1994) formulation for consideration of confinement effects in the stress-strain behavior of concrete in rectangular column cross-sections.

The Mander *et al.* (1988a) confinement model is also applicable for circular column cross-sections. First, effectively confined area A_e and core concrete area A_{cc} should be revised with respect to the geometry of circular cross-sections:

$$A_e = \frac{\pi d_s^2}{4}\left(1 - 0.5\frac{s'}{d_s}\right)^k \tag{3.27}$$

$$A_{cc} = (1 - \rho_{cc})\frac{\pi d_s^2}{4} \tag{3.28}$$

Then, volumetric reinforcement ratio for transverse steel ρ_s and the longitudinal reinforcement ρ_{cc} are modified for circular cross-section as follows;

$$\rho_s = \frac{4\,A_{sh}}{s\,d_s} \tag{3.29}$$

$$\rho_{cc} = \frac{A_{st}}{\pi\,{d_s}^2} \tag{3.30}$$

Finally the lateral confinement pressure can be obtained as:

$$A_e = \frac{\rho_s f_s}{2} \frac{\left(1 - 0.5\dfrac{s'}{d_s}\right)^k}{1 - \rho_{cc}} \tag{3.31}$$

Once the lateral confinement pressure is obtained, then the same equations proposed for rectangular cross-sections can be used to obtain confined compressive stress for circular cross-sections.

For illustration, a representative plot is presented in Figure 3.12 and 3.13 for comparison of the unconfined and confined concrete stress–strain relationships for Column 1 tested by Priestley and Benzoni (1996) and H/D(3)-T/M(0.0)/1.32% tested by Shanmugam (2009), obtained using both the Chang and Mander (1994), and the Saatcioglu and Razvi (1992) confinement model formulations.

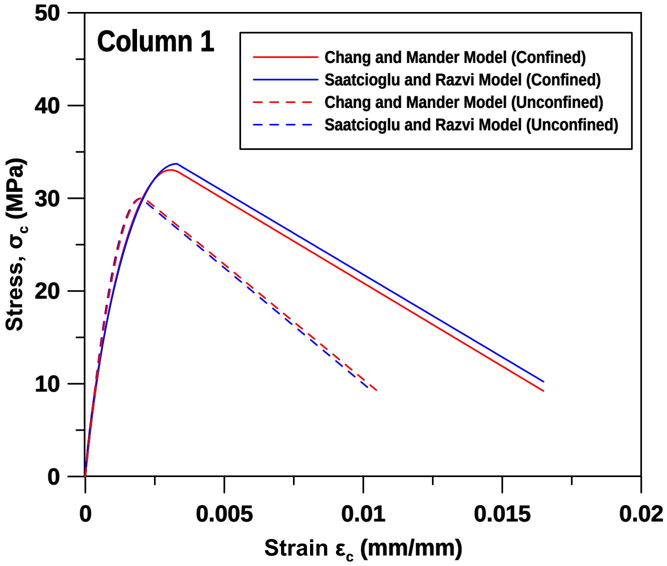

Figure 3.12. Confined and unconfined concrete stress strain curves under compression for Column 1 (Priestley and Benzoni, 1996)

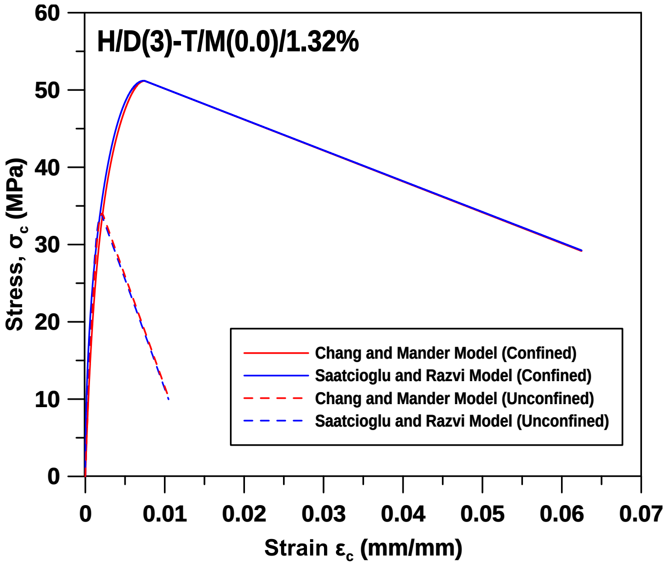

Figure 3.13. Confined and unconfined concrete stress strain curves under compression for specimen H/D(3)-T/M(0.0)/1.32% (Shanmugam, 2009)

Saatcioglu and Razvi (1992) also proposed a model for the stress-strain relationship of confined concrete in compression, based on test results obtained for both well confined and poorly confined sections, with either rectangular or circular cross sectional geometry. The model uses a parabolic ascending region until concrete reaches its confined compressive strength, followed by a linear descending branch. In this study, the stress-strain relationship for confined concrete proposed by Chang and Mander (1994) used for calibration; however, since the Chang and Mander (1994) model formulation does not empirically define the slope of the descending region of the stress-strain relationship, this slope was manually calibrated to match the descending slope of the Saatcioglu and Razvi (1992) model for confined concrete (as was also done for unconfined concrete). Accordingly, parameters listed in Table 3.11 are obtained by applying the aforementioned confinement equations for the cross-sections of the column specimens investigated in this study. These parameters are used in calibration of the Chang and Mander (1994) constitutive model for confined concrete.

Table 3.11. Calibration Parameters for Confined Concrete

Specimen	f'_{cc}	E_{cc}	ε_{cc}	r_c	x_{crnc}
	(Mpa)	(Mpa)	(mm/mm)	-	-
2CLH18	33.37	30553	0.0022	4.52	1.092
3CLH18	27.20	28300	0.0021	3.33	1.146
2CMH18	27.96	28595	0.0021	3.48	1.138
3CMH18	26.08	27856	0.0021	3.12	1.167
3CMD12	26.82	28149	0.0024	3.26	1.176
Specimen No:1	23.15	26638	0.0028	2.55	1.322
Specimen No:2	23.15	26638	0.0028	2.55	1.322
Specimen No:4	23.84	26933	0.0028	2.68	1.279
Column 1	33.05	30443	0.0031	4.45	1.106
Column 2	31.77	29996	0.0026	4.21	1.116
H/D(3)-T/M(0.0)/1.32%	51.16	35865	0.0074	7.94	1.031
H/D(6)-T/M(0.0)/0.73%	44.25	33965	0.0053	6.61	1.055

3.2.3. Calibration of the Rotational Interface Spring

Specimens are assumed to be fixed at the bottom in the original finite element model formulation. This assumption leads to steeper initial stiffness estimation compared to experimentally observed initial stiffness. Longitudinal reinforcing bars that are subjected to tension due to moment at the base of the columns experience axial elongation within the pedestal, due to the so-called strain penetration effects. With this additional elongation effect on the longitudinal bars, the initial stiffness of the column specimen is reduced, which is a physical and well-known phenomenon observed in structural walls and columns with relatively low shear span to depth ratios. To incorporate this strain penetration effect in modeling, Massone *et al.* (2009) proposed a simple methodology (Figure 3.14).

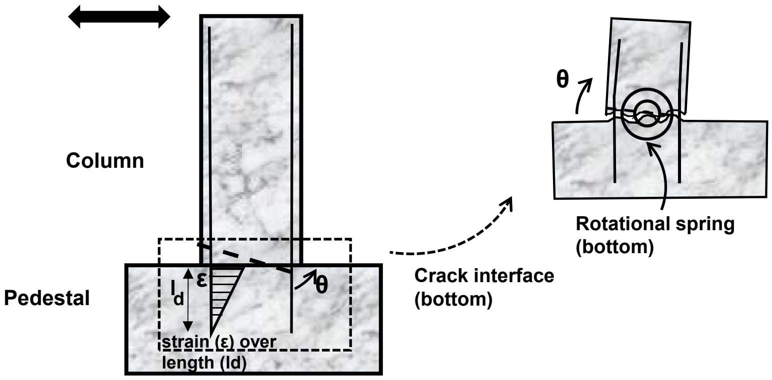

Figure 3.14. Interface crack and rotational spring model (Massone *et al.*, 2009)

According to this methodology, it is assumed that a crack is formed along the column-pedestal connection, called an interface crack (Figure 3.14). Following the formation of the interface crack, the flexural rigidity of the column reduces especially at low drifts levels.

Formation of this crack and its influence in initial stiffness is behaviorally represented using a rotational spring assigned to the column-pedestal interface. To define the stiffness of this rotational spring, first, a linear strain distribution was assumed along the development length of the longitudinal reinforcing bar. The distribution starts from zero and ends at the interface crack location at its maximum value. Integrating this strain area along the development length gives the longitudinal extension of the reinforcing bar, which is assumed to be accumulated at the interface. The corresponding rotation at the column-pedestal interface is derived by dividing the elongation with the depth of the neutral axis, under a specific bending moment value at or below yield moment. Once this angle of rotation is obtained, the rotational stiffness of the interface spring can be obtained by dividing the corresponding bending value to the angle of rotation.

This simple approach with the rotational interface spring was implemented in the present model formulation. The sectional analyses necessary to obtain the rotational stiffness of the interface spring were conducted using the software Xtract. Accordingly, the rotational stiffness values calculated for the interface spring are listed in Table 3.12. Representative figure is depicted in Chapter 4 for specimen 2CLH18 to clearly see the effect of rotational interface spring (Figure 4.2).

Table 3.12. Rotational Spring Calibration

Specimen	l_d	P_{ax}	$EI_{eff.}$	K_θ
	(mm)	(kN)	MNm2	MNm
2CLH18	600	518.8	40.94	136.4
3CLH18	806	518.8	50.84	126.1
2CMH18	630	1512.4	45.31	143.9
3CMH18	816	1512.4	54.50	133.6
3CMD12	816	1512.4	53.55	131.3
Specimen No:1	880	667	39.25	96.2
Specimen No:2	880	2670	57.15	129.8
Specimen No:4	816	667	39.27	96.2
Column 1	369	503	37.73	204.5
Column 2	369	503	51.86	281.1
H/D(3)-T/M(0.0)/1.32%	632	592	83.27	263.5
H/D(6)-T/M(0.0)/0.73%	632	592	81.46	257.8

3.2.4. Calibration for Strain Localization Effects

The so-called strain localization phenomenon in nonlinear modeling was briefly described in Chapter 2 of this Thesis. In this section, the regularization technique used to calibrate the post-peak slope of the concrete stress-strain relationship is described.

In the model formulation used, the envelope curve of concrete constitutive models was modified, by recalibrating the descending region of stress-strain curve of concrete in compression.

The post-peak slope of envelope stress-strain curve for concrete was recalibrated, in order to maintain constant fracture energy (which is related to the area under stress-strain curve and the volume of the constitutive model element) irrespective of the size of the model elements used. The modified post-peak slope (Figure 3.15) was defined according to strain value corresponding to the point where the concrete stress-strain relationship reaches zero. This strain value ε_r is defined using Equation 3.32.

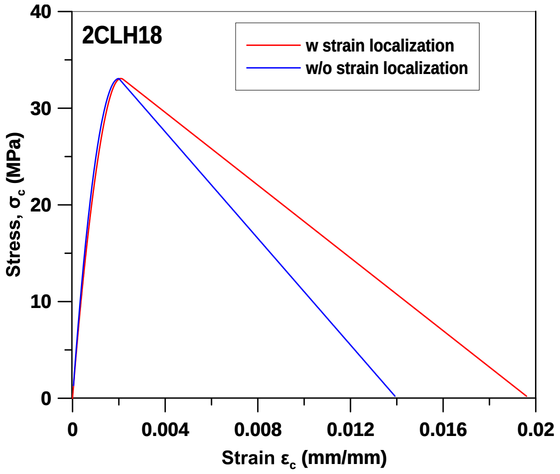

Figure 3.15. Post-peak slope of the specimen 2CLH18 considering strain localization. (Lynn, 2001)

ε_r is expressed:

$$\varepsilon_r = \frac{G_{f,c}}{f'_c L_e} - \frac{f'_c}{E_c} + \varepsilon_p \tag{3.32}$$

where $G_{f,c}$ is fracture energy in compression for concrete, f'_c is concrete compressive strength, L_e is the length (vertical dimension) of the model element, E_c is elasticity modulus of concrete and ε_p is the strain corresponding to the peak stress.

For E_c, Equation 3.2 was adopted as suggested by Chang and Mander (1988). Once ε_r is obtained, then the fracture energy can be calculated as:

$$G_{f,c} = \left(\frac{f'_c}{E_c} + (\varepsilon_r - \varepsilon_p) \right) f'_c L_p \tag{3.33}$$

where L_p is the plastic length, that was assumed to correspond to height of standard cylinder tests specimen with a height of 300 mm. Post-peak slopes of the stress-strain behavior of concrete in compression, for each of the test specimens investigated were recalibrated using the parameters listed in Table 3.13.

Table 3.13. Strain Localization Calibration

Specimen	n	ε_r	G_{fc}	ε'_r	x_{crn}	x_{crn}
	(mm)	(mm/mm)	(MN/mm)	(mm/mm)	(Before)	(After)
2CLH18	8	0.0139	115.23	0.0198	1.078	1.052
3CLH18	8	0.0140	96.97	0.0206	1.118	1.075
2CMH18	8	0.0140	100.42	0.0206	1.110	1.068
3CMH18	8	0.0141	93.02	0.0207	1.129	1.079
3CMD12	8	0.0140	93.02	0.0206	1.129	1.079
Specimen No:1	8	0.0139	76.19	0.0206	1.225	1.126
Specimen No:2	8	0.0139	76.19	0.0206	1.225	1.126
Specimen No:4	8	0.0140	79.24	0.0208	1.205	1.114
Column 1	8	0.0216	193.49	0.0522	1.106	1.039
Column 2	8	0.0167	139.49	0.0394	1.116	1.043
H/D(3)-T/M(0.0)/1.32%	8	0.1358	2036.29	0.1754	1.031	1.024
H/D(6)-T/M(0.0)/0.73%	16	0.0566	713.63	0.0716	1.055	1.043

4. EXPERIMENTAL VALIDATION OF THE MODEL

In this Chapter, validation of analytical model is presented for the RC column specimens that were described in the previous chapter. Nonlinear analysis of the RC column specimens was performed using the analytical model formulation described in Chapter 2, with the same systematic calibration procedure presented in Chapter 3. Lateral load – top displacement response predictions of the analytical model for each column specimen were compared with experimental observations. Since experimental data was not available for the specimens at local response levels, local response predictions of the analytical model were presented for demonstrative purposes. As described in the previous chapter, there are four different test programs considered for experimental validation of the model. It should be noted that the principal aim of this study is not to obtain perfectly accurate response predictions using adjusted model parameters for each specimen considered, but to evaluate the overall effectiveness of the model for various column configurations and failure modes. Therefore, parameters of the analytical model were not manipulated to optimize the model predictions for each test specimen. Identical model calibration methods were used for all column specimens investigated, except the parameters that represent the different geometric, reinforcement, and material characteristics of the column specimens, and the different loading conditions.

4.1. Lynn Specimens (2001)

Lynn (2001) tested eight full scale columns for investigating the behavior of typical columns configurations in existing building structures. Five of the eight specimens that do not incorporate lap splices were selected for analytical response predictions. Column specimens were tested under low and intermediate levels of axial load, with different spacing and configuration of transverse reinforcement. Longitudinal reinforcement amounts were also changed, while other parameters were kept constant.

For the five specimens tested by Lynn (2001), a rotational interface spring was considered to consider strain penetration effects, as described in Chapter 3. Cyclic top displacement histories were defined according to applied test data. Strain localization effects were also considered, and the post-peak slope of the stress-strain envelope of the concrete model was modified according to the methodology described in Chapter 3. Transverse reinforcement of the column specimens tested by Lynn (2001) had 90-degree hooks, so confinement effect was not considered in the calibration of concrete stress-strain behavior. However, contribution of transverse reinforcement to the shear strength of column specimens were considered. Tension stiffening effect on reinforcement was ignored, as explained in Chapter 2. Cyclic curvature degradation parameters of reinforcing steel, R_0, a_1 and a_2 were selected as recommended by Menegetto and Pinto (1973) as 20, 18.5 and 0.15, respectively. Strain hardening ratio of reinforcing steel was assigned in the model based on the measured stress-strain relationships for longitudinal and transverse reinforcing bars, as reported in the experimental study (Lynn, 2001). Strain hardening ratios for transverse reinforcement and longitudinal reinforcements were taken as 0.47% and 0.38%, respectively.

Specimen 2CLH18 consists of 8 #8 (25mm) longitudinal reinforcing bars whereas 3CLH18 consists of 8 #10 (32mm) longitudinal reinforcing bars, which leads to lower flexural strength for 2CLH18. Specimen 3CLH18 was designed to promote shear failure, with increased flexural strength due to higher longitudinal reinforcement ration, while spacing and configuration of transverse reinforcement were kept constant. Both of these specimens were tested under low axial load levels which corresponds to 12% of the capacity (0.12% $A_g f'_c$). As expected, test observations showed that specimen 2CLH18 experienced flexure dominant ductile behavior up to the last drift cycles, whereas specimen 3CLH18 specimen suffered early strength degradation due to brittle shear behavior.

Figure 4.1 shows the comparison of the lateral load – top displacement response of analytical model with test results for the specimen 2CLH18. Capacity is well-captured up to 1.5% drift ratio in the positive loading direction and is in good agreement with test results up to 2% drift in the negative loading direction.

Strength degradation started at 3% drift ratio and specimen represented shear failure after higher strain values developed at column base, which was reasonably captured by the model. Model estimations are also reasonable for the initial stiffness of the column.

Experimentally-observed lateral load capacity was kept constant until the last drift ratio, which represents flexural dominant behavior. As shown in Figure 4.1, analytical model captures the degradation of lateral load capacity at the last drift level of 3%, as well as contribution of higher shear deformation at the last drift level. Hysteretic properties of the experimentally-observed response are also reasonably-well represented in the model results, although the model moderately overestimates pinching behavior.

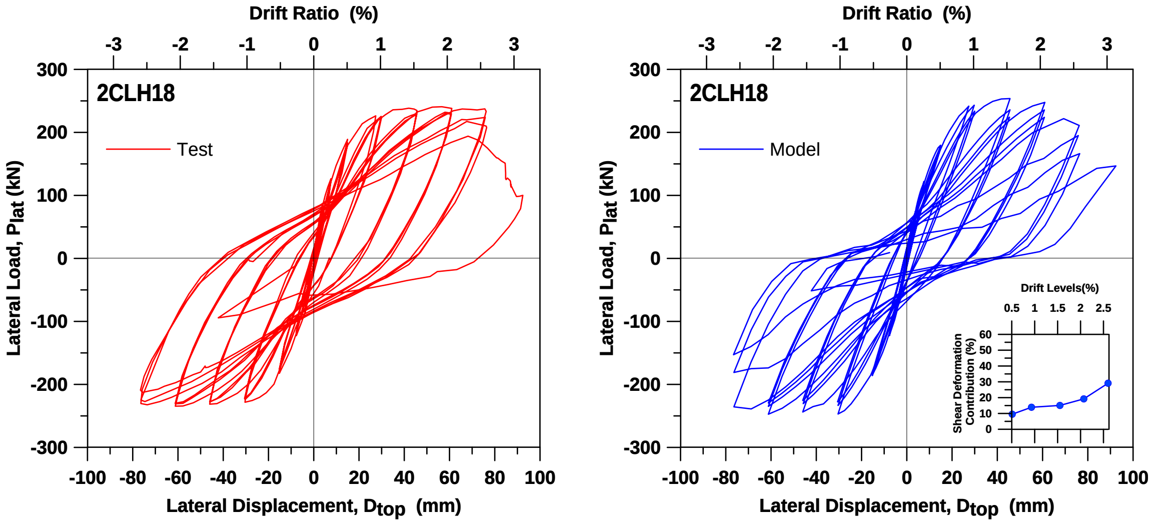

Figure 4.1. Experimentally Observed and Analytically Predicted Lateral Load vs Top Displacement Results for Specimen 2CLH18 (Lynn, 2001)

For the specimen 2CLH18, influence of rotational spring implementation is illustrated in Figure 4.2. Two model results are compared with experimentally observed response. In addition to this, the cumulative dissipated energy vs. drift level relationships for the specimen 2CLH18 is presented in Figure 4.3. According to the figure, model slightly underestimated the cumulative dissipated energy compared to experimentally observed response due to narrower cyclic loops.

The cumulative dissipated energy graphs are illustrated at Appendix for the rest of the specimens.

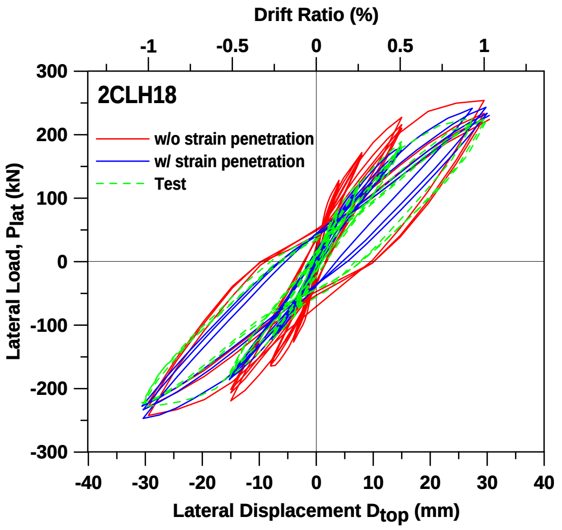

Figure 4.2. Rotational Spring Implementation for Specimen 2CLH18 (Lynn, 2001)

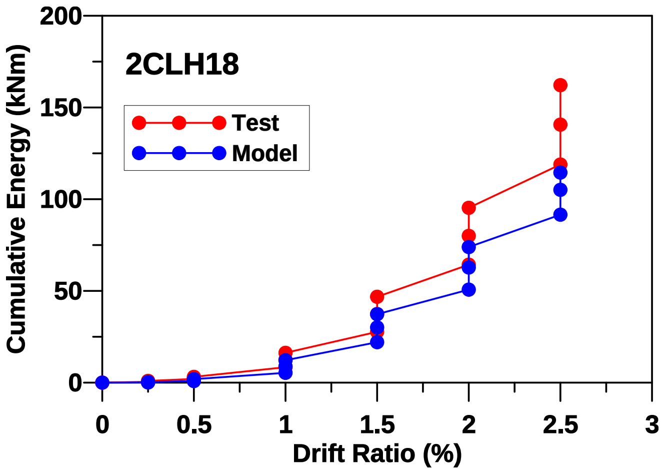

Figure 4.3. Dissipated Cumulative Energy vs. Drift Level for Specimen 2CLH18 (Lynn, 2001)

The analytical model is also capable of predicting the local responses of the RC column specimens. Lateral flexural and shear displacement profiles versus lateral load plots are shown in Figure 4.4 for specimen 2CLH18, in order to observe the shear and flexural deformation contributions to top displacement at each drift level. As shown in Figure 4.4, analytical predictions for flexural and shear deformation contributions of the specimen follow flexural dominant behavior (with approximately 2% flexural drift and 0.5% shear drift before significant strength degradation starts), which is expected for flexure-controlled columns with relatively high shear span to depth ratios.

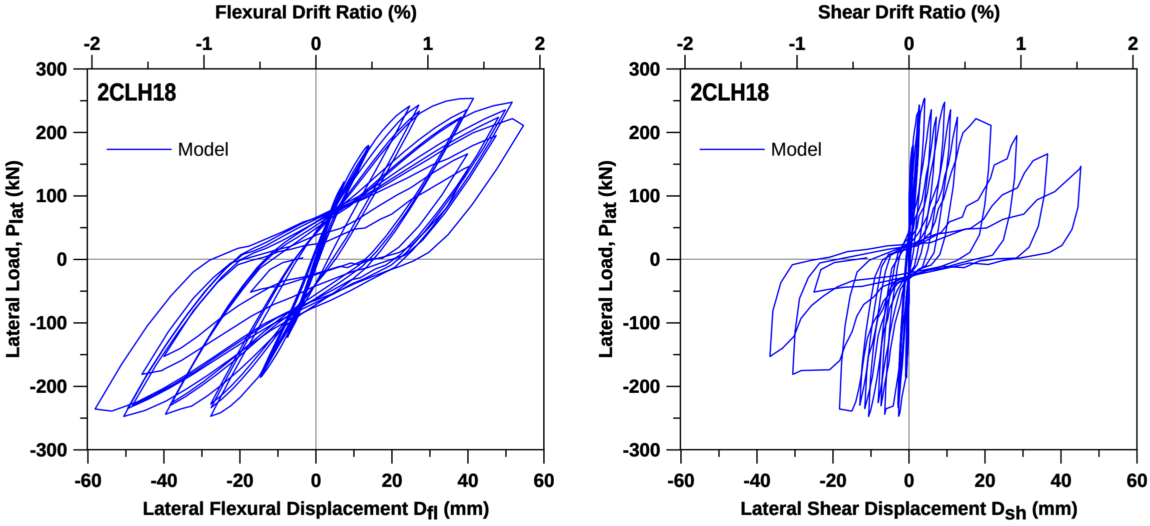

Figure 4.4. Flexural and Shear Deformation vs. Lateral Load for Specimen 2CLH18 (Lynn, 2001)

Longitudinal strain profiles at column base and total, flexural and shear lateral displacement profiles along column height were analytically estimated as shown in Figures 4.5, 4.6 and 4.7. These local deformation predictions are representatively shown here for specimen 2CLH18. Further predictions of the analytical model for local responses of the remaining specimens are presented in Appendix A. Longitudinal strain profiles were obtained along the width of the column specimen at the base, in order to observe the longitudinal strain values in concrete and reinforcing steel, at different drift levels. Variation of longitudinal (vertical) strain along the width of the column base is presented for increasing drift ratio, in Figure 4.5.

After lateral load degradation starts, the strain profile starts becoming erratic; therefore, the strain profile was only presented for the drift levels before strength degradation starts. In Figure 4.5, strain distribution in the compression zone was shown exaggeratedly, to better demonstrate the compressive strains developing in concrete. As well, the strain profiles shown in Figure 4.5 also show that the strain distribution does not necessarily follow the plane section remains plane assumption (typically used in sectional analysis or fiber models), especially at relatively large drift levels.

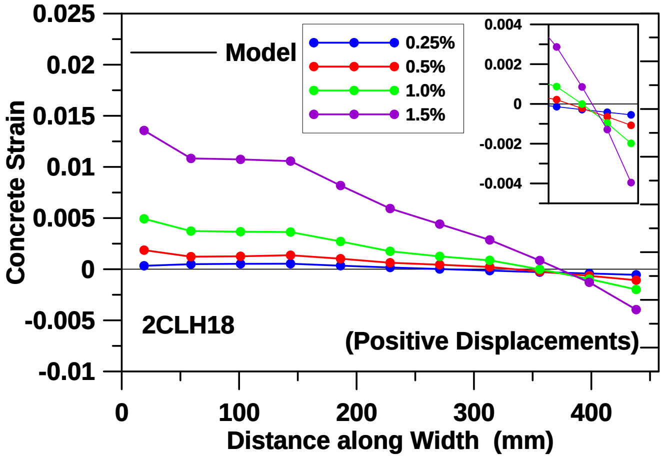

Figure 4.5. Longitudinal Strain Profiles for Specimen 2CLH18 (Lynn, 2001)

Analytical model predictions for the lateral displacement profiles along the height of the column specimen are shown in Figures 4.6 and 4.7. Lateral flexural displacement values are higher than lateral shear displacement values along the height of the column specimen at each drift level, which explains the flexural dominant behavior of specimen 2CLH18. The model results also represent concentration of nonlinear flexural deformations along the bottom 20% of the height of the column specimen, which can be considered as the plastic hinge region where the flexural demands are larger.

The main difference between specimens 2CLH18 and 3CLH18 was the longitudinal reinforcement ratio, as mentioned before, except minor concrete compressive strength difference obtained at the test day.

Therefore, both columns had approximately the same shear strength. However, by increasing flexural strength of specimen 3CLH18, it was made susceptible to shear failure. Test results have shown a shear-controlled failure mode for this specimen.

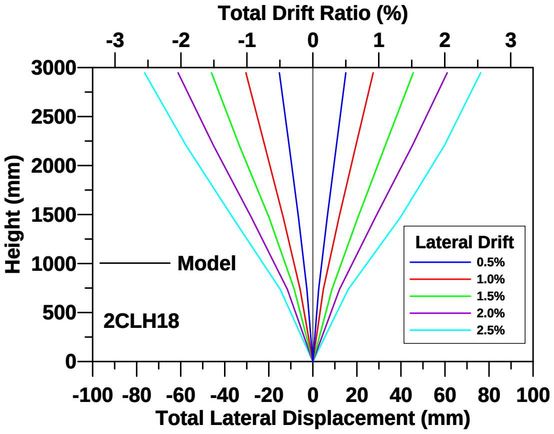

Figure 4.6. Total Lateral Displacement Profiles for Specimen 2CLH18 (Lynn, 2001)

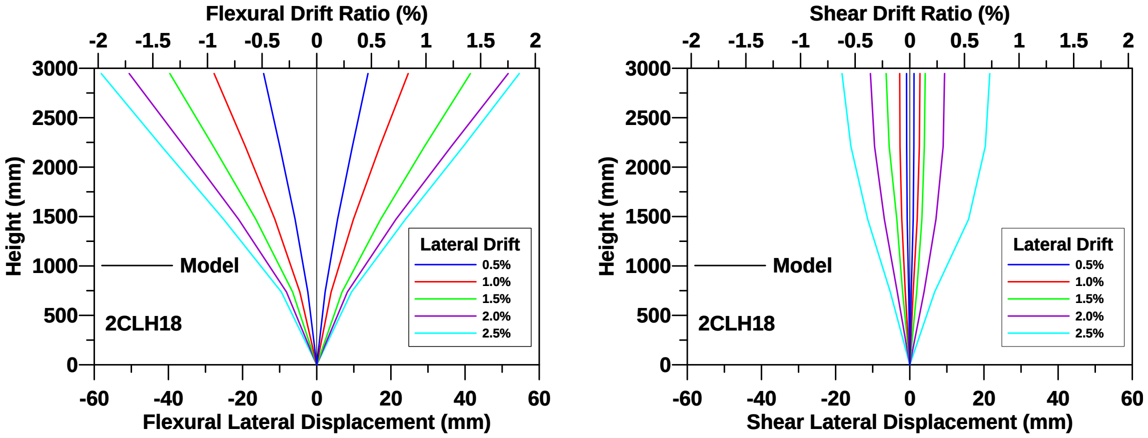

Figure 4.7. Flexural and Shear Lateral Displacement Profiles for Specimen 2CLH18 (Lynn, 2001)

According to test results of specimen 3CLH18, shown in Figure 4.8, the lateral load capacity of the column dropped to 50% of its peak value at a drift level of 1%. The model predicts strength degradation also at 1% drift.

In the model prediction, strength degradation is more gradual compared to the experimentally measured response. Contribution of shear deformation to lateral displacement rapidly increases (compared to 2CLH18) at around this drift level. The model overestimates the residual lateral load capacity at higher drift levels, which is possibly due to the incapability of the model of capturing buckling of the longitudinal bars. Initial stiffness of the specimen 3CLH18 is also well represented by the model.

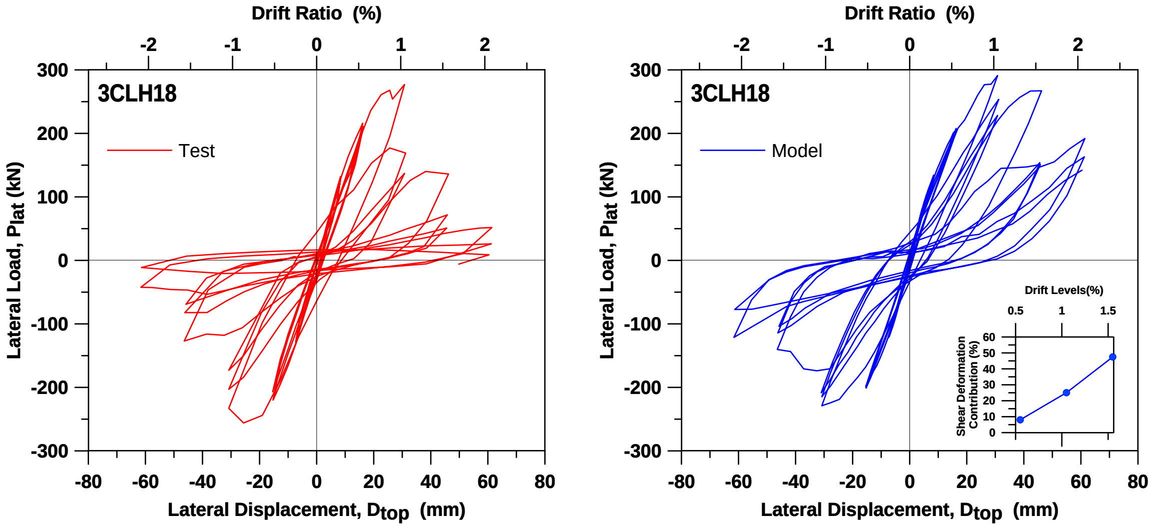

Figure 4.8. Experimentally Observed and Analytically Predicted Lateral Load vs Top Displacement Results for Specimen 3CLH18 (Lynn, 2001)

The lateral load vs. top displacement behavior of 3CLH18 was similar to 2CLH18 at early stages of loading. The behavior of this column specimen was controlled by shear-flexure interaction, followed by shear failure. Contribution of flexural and shear deformations to overall response of the column is analytically shown in Figure 4.9. As depicted in the analytical predictions, after the column reaches capacity and strength degradation is initiated, shear deformation contribution rapidly increases at larger drift ratios, especially in the negative loading direction. Overall, the model captures the limited drift capacity of the column (1% drift), due to shear failure associated with inadequate shear reinforcement.

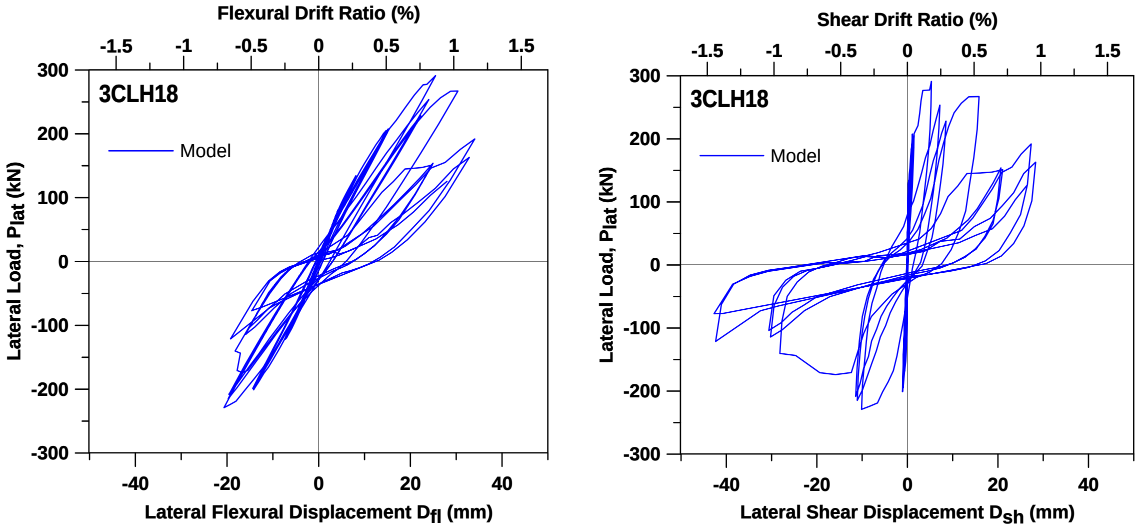

Figure 4.9. Flexural and Shear Deformation vs. Lateral Load for Specimen 3CLH18 (Lynn, 2001)

In order to investigate the effect of spacing and configuration of transverse reinforcement on the column response, specimen 3CMD12 was designed and tested. Diamond shape transverse reinforcement configuration was used in this specimen. Spacing of transverse reinforcement was reduced from 457 mm to 305 mm. Level of axial load increased from low to moderate, which corresponds to 35% of axial load capacity of the section $(0.35 A_g f_c')$. Although transverse reinforcement was improved compared to other column specimens tested by Lynn (2001), in terms of configuration and spacing of transverse reinforcement, stress-strain behavior of concrete in the analytical model was calibrated as unconfined behavior, because the specimen was constructed using 90 degree hooks on the transverse reinforcement.

Increased axial load level and improved transverse reinforcement configuration with reduced spacing leads to higher lateral load capacity for specimen 3CMD12, as shown in Figure 4.10. Model prediction is in good agreement with experimentally-observed lateral load capacity. Initial stiffness estimation is also reasonably well.

The model slightly underestimates the strength degradation however; initiation of strength degradation is predicted by the model at approximately the same drift ratio (1.5% drift) as test results. Shear deformation contribution predicted by the model rapidly increases at higher drift ratios. Overall, the experimentally-observed behavior mode of this specimen was relatively brittle flexural behavior (due to high axial load) followed by shear compression failure at approximately 1.5% drift, which was also represented in the model results.

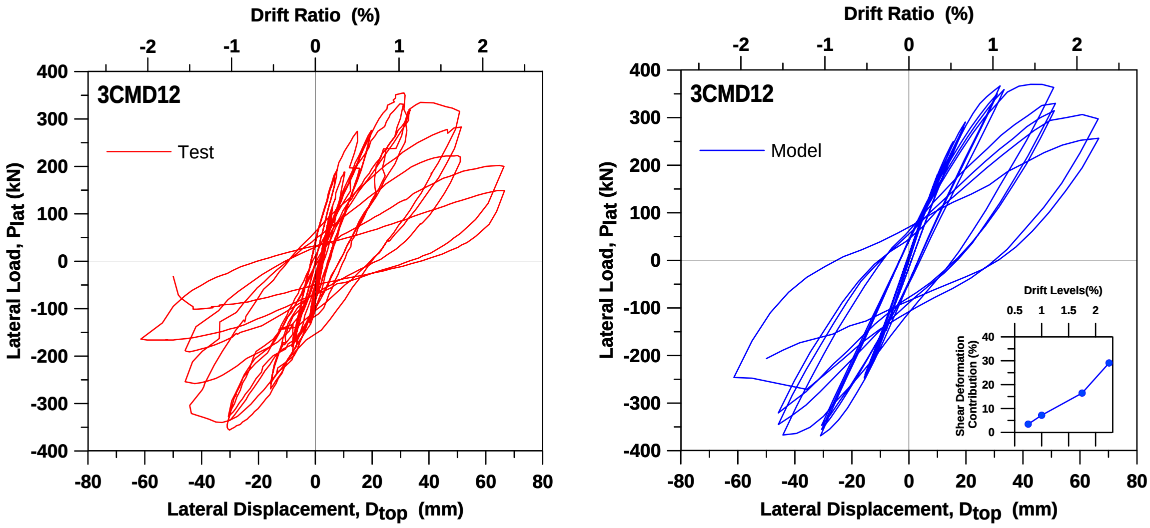

Figure 4.10. Experimentally Observed and Analytically Predicted Lateral Load vs Top Displacement Results for Specimen 3CMD12 (Lynn, 2001)

At the initial drift levels, the behavior of the column is dominated by flexural deformation, similarly to the previous specimens, due to the relatively high shear span to depth ratio ($M/VD = 3$). As shown in Figure 4.11, the flexural deformation contribution to lateral displacement is more dominant than the shear deformation contribution, although the ultimate failure mode is shear compression failure. Overall, the model is capable of capturing the overall response characteristics and the failure mode of this specimen also.

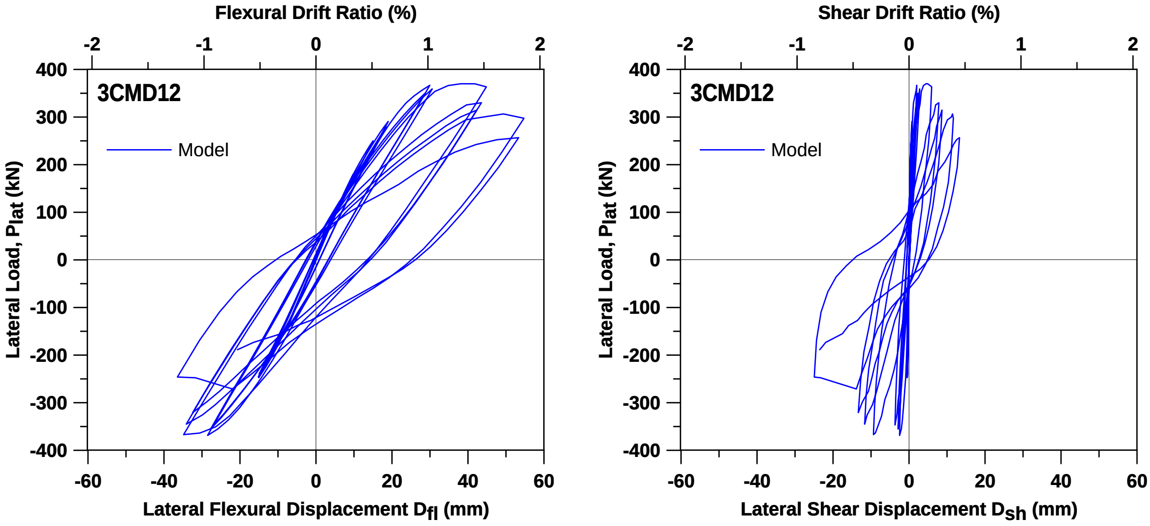

Figure 4.11. Flexural and Shear Deformation vs. Lateral Load for Specimen 3CMD12 (Lynn, 2001)

In order to identify the influence of different axial load levels on column response (relative to specimens 2CLH18 and 3CLH18), specimens 2CMH18 and 3CMH18 specimens were built and tested. All the other parameters in these specimens were kept constant, except the level of axial load increased from low to moderate ($0.35A_g f'_c$). Testing of specimen 2CMH18 was unexpectedly terminated due to formation of an unexpected inclined crack at the top of the specimen. Still, it was observed that from the test results of this specimen that before this termination of the test, the specimen was able to reach its flexural capacity. The model results obtained for this specimen also show a flexural dominant response. Lateral load capacity estimation of the model is in good agreement with test results in both positive and negative loading directions (Figure 4.12). Shear deformation contribution is limited to approximately 10% of lateral displacement, which is compatible with the experimental observations.

In addition to this, lateral load vs. flexural and shear deformation plots estimated by the analytical model (Figure 4.13) also demonstrate flexure-controlled behavior, with limited shear deformation contribution to lateral displacement.

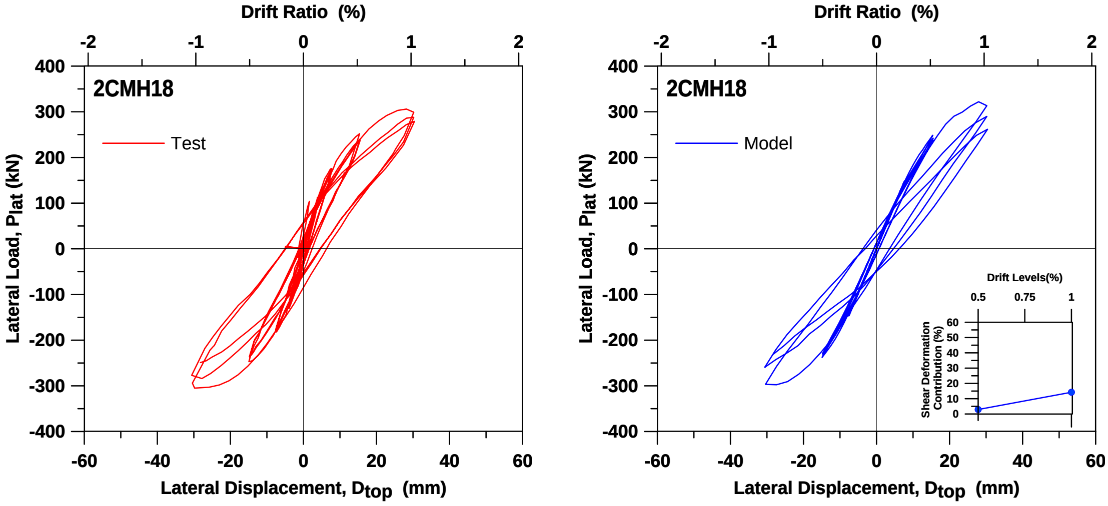

Figure 4.12. Experimentally Observed and Analytically Predicted Lateral Load vs Top Displacement Results for Specimen 2CMH18 (Lynn, 2001)

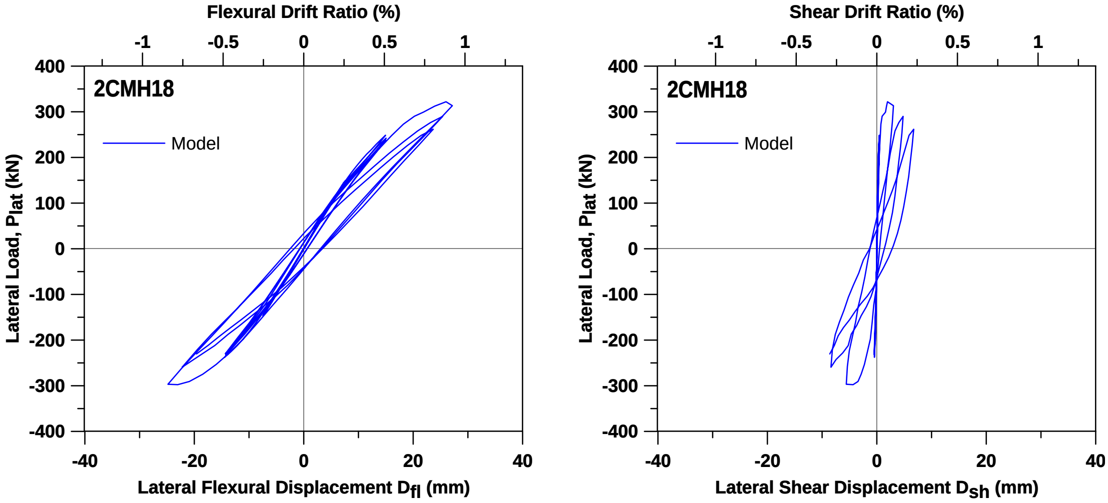

Figure 4.13. Flexural and Shear Deformation vs. Lateral Load for Specimen 2CMH18 (Lynn, 2001)

In order to make a comparison between the response of column specimens 3CLH18 and 2CLH18, specimen 3CMH18 was built and tested. This specimen was designed with 3% longitudinal reinforcement ratio and was tested under a moderate level of axial load corresponding to 35% of the axial capacity.

Test observations for specimen 3CMH18 indicated that the column experienced shear compression failure at a drift level of approximately 1%, which was also captured by the analytical model. As also observed experimentally, the analytical model predicted significant strength degradation after reaching the lateral load capacity at approximately 1% drift (Figure 4.14). In the model results, contribution of shear deformation to lateral displacement suddenly increases at this drift level of when strength degradation starts. The residual lateral load capacity at higher drift levels was slightly overestimated by the model.

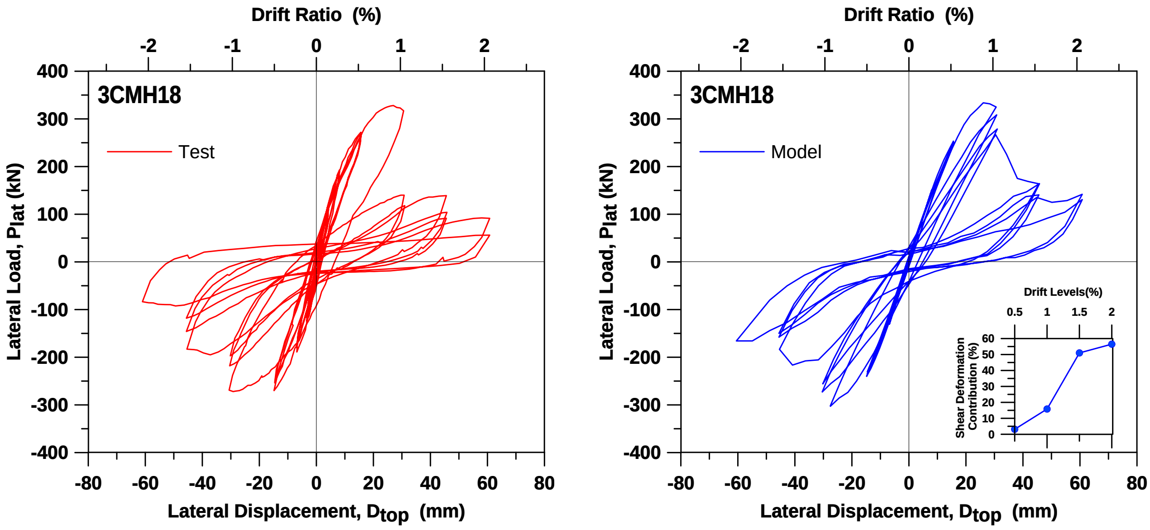

Figure 4.14. Experimentally Observed and Analytically Predicted Lateral Load vs Top Displacement Results for Specimen 3CMH18 (Lynn, 2001)

For this specimen, the longitudinal strain distributions at predicted at column base were plotted until the 1% drift level, which corresponded to the initiation of strength loss (Figure A.4). The strain profiles show that the longitudinal steel does not yield, whereas the concrete crushes at 1% drift, which is compatible with the overall response. The failure type of this specimen was shear compression failure, similarly to specimen 3CLH18. At the last drift level of 2%, the model prediction for the residual lateral load capacity is slightly higher. Flexural and shear deformation versus top lateral load responses is shown in Figure 4.15. Analytical model predictions indicated shear failure for this specimen, which is consistent with the test results.

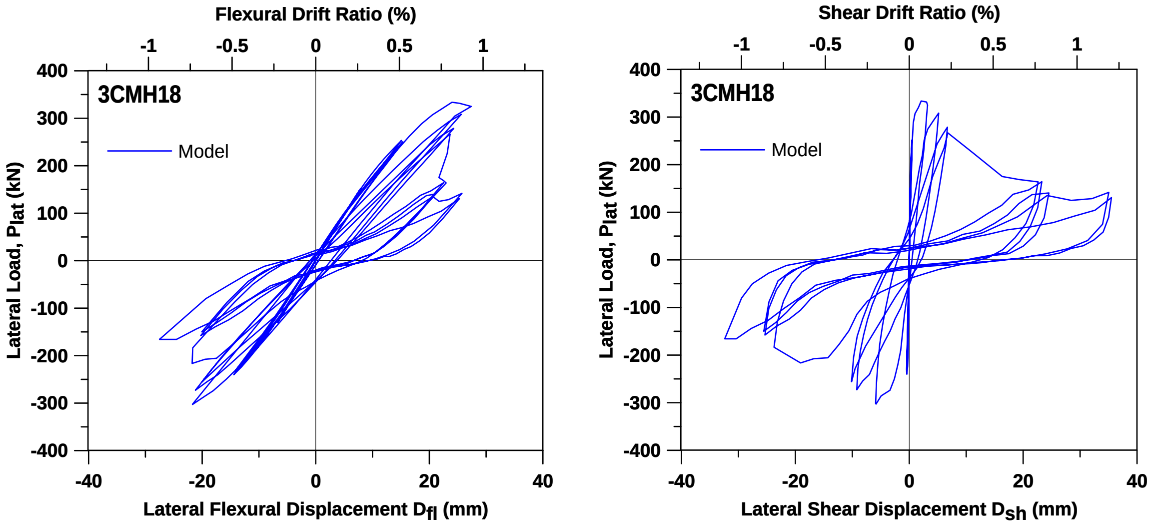

Figure 4.15. Flexural and Shear Deformation vs. Lateral Load for Specimen 3CMH18 (Lynn, 2001)

4.2. Sezen and Moehle (2002) Specimens

Sezen and Moehle tested four full scale RC column specimens under reversed cyclic loading to observe poorly reinforced column behavior under severe or moderate earthquakes. Another motivation was to identify post-earthquake behavior of columns. Columns with identical cross sections were loaded under different levels of axial loads. For Specimen 1, low level of axial load was applied (15% of axial load capacity). In order to estimate the influence of the axial load level, Specimen 2 was tested under 60% percent of its axial load capacity. Within the scope of this study, Specimen 4 was also investigated, which was loaded cyclically up to 1% drift level, and the top displacement increases monotonically after that, to observe whether the lateral load capacity of the model degrades under further monotonic loading or not.

In order to follow a consistent modeling methodology, similar calibration approaches that were applied to the Lynn (2001) specimens were used for these three specimens.

Tension stiffening effect on reinforcement was ignored and rotational interface spring implementation and mesh discretization procedures were carried out similarly to the Lynn (2001) specimens. The specimens were subjected to double curvature loading conditions. Strain localization phenomenon was considered to minimize the effect of mesh size on the analytical response.

However, according to preliminary analysis results carried out for these specimens, cyclic steel strss-strain parameters R_0, a_1 and a_2 are defined differently from the Lynn (2001) specimens. The parameters of R_0, a_1 and a_2 are defined as proposed by Elmorsi *et al.* (1998) as 20, 18.5 and 0.0015, respectively.

Since the transverse reinforcement of these specimens were constructed with 90-degree hooks, confinement effect was ignored in the model.

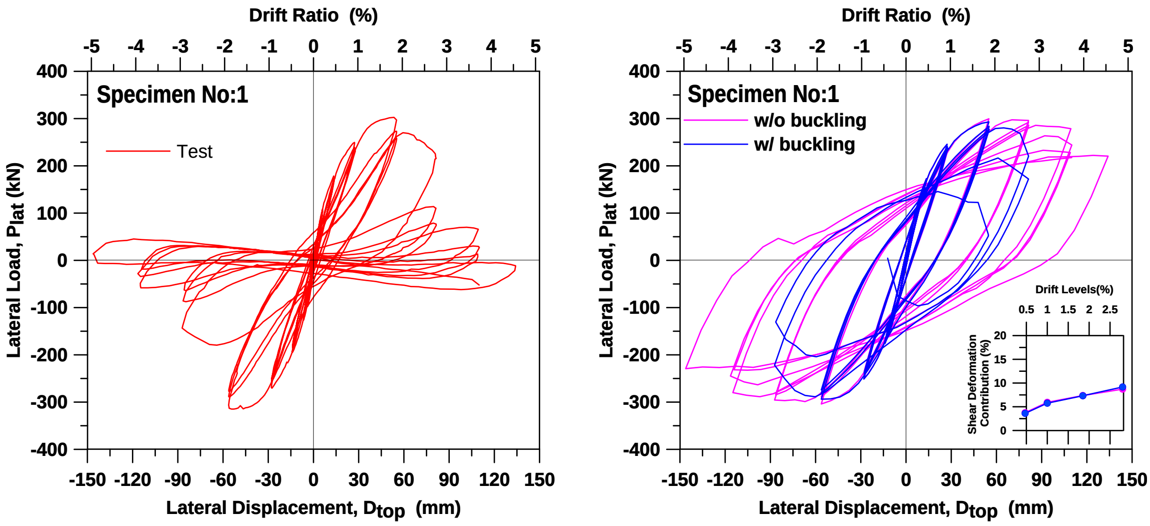

Figure 4.16. Experimentally Observed and Analytically Predicted Lateral Load vs Top Displacement Results for Specimen No:1 (Sezen, 2002)

Figure 4.16 presents the comparison of experimentally-observed and analytically predicted lateral load vs. deformation responses for Specimen No:1 (Sezen, 2002). Reasonable agreement between model and test results is observed up to the first loading cycle to 2% drift level.

Following this drift level, specimen lost its lateral load capacity by approximately 50%, due to observed bar buckling failure. The analytical model was not capable of simulating this experimentally observed strength degradation due to bar buckling. Hence, strength degradation of this specimen could not be simulated by the model. To investigate the effect of bar buckling on strength degradation, the compression envelope of the steel stress-strain model was modified using a negative strain hardening ratio for this specimen. The strain hardening ratio of the longitudinal reinforcement in compression was simply recalibrated, according to proposed methodology of Dhakal (2002), to investigate whether the model results will be improved with the implementation of buckling behavior in the steel stress-strain model for future studies. The strain hardening ratio in compression was implemented with a negative value (%3.6). When the steel stress-strain model with the modified negative strain hardening ratio was implemented in the model, the model predictions were found to be reasonable in terms of drift capacity and strength degradation behavior, as shown in Figure 4.16.

Figure 4.17 presents the lateral load versus lateral shear and flexural deformation predictions of the model. Due to relatively high shear span to depth ratio of this specimen, the hysteretic behavior until failure was dominated by flexural deformation component. The shear response contribution was estimated to be approximately linear elastic. Since the specimen did not experience shear failure, the analytically-predicted flexural dominant behavior is consistent with the experimentally observed response of this specimen.

For Specimen No:2, level of axial load was increased from 15% to 60% of the axial load capacity, to investigate the influence of axial load on column response. Test results showed that, the ductility of this specimen significantly decreased under the high axial load level. According to test measurements, at 1% drift ratio, the lateral load capacity started dropping. Up to the failure point, overall response hysteretic response characteristics were predicted reasonably well by the model. Lateral load capacity is well represented with gradual strength degradation after a drift capacity of approximately 1% in the negative loading direction.

Experimentally observed sudden drop in lateral load capacity occurred due to opening of the hooks on the transverse reinforcing bars and buckling of longitudinal reinforcing bars. This failure mode was associated with the high level of axial load applied on this specimen. Although the model cannot predict such sudden strength degradation, since rebar buckling behavior is not defined in its formulation, model predictions for the lateral load capacity and drift capacity of this column are still reasonably accurate.

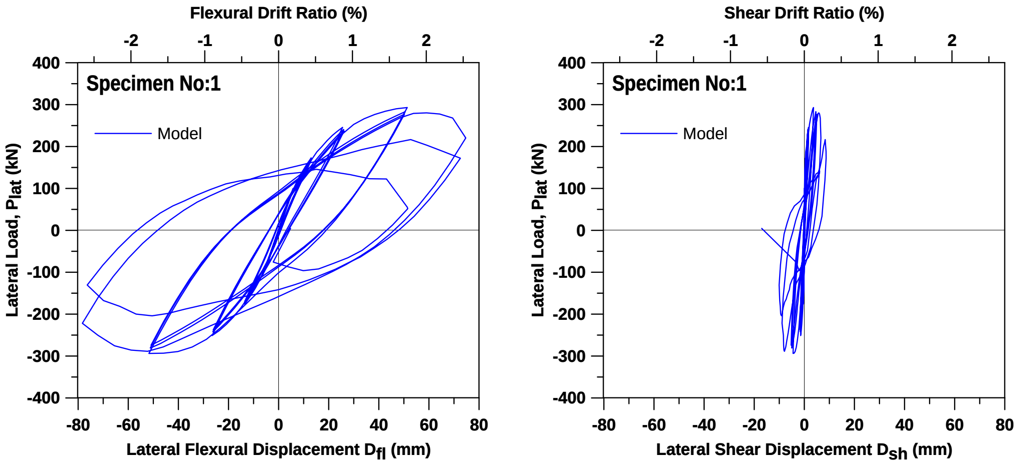

Figure 4.17. Flexural and Shear Deformation vs. Lateral Load for Specimen No:1 (Sezen, 2002)

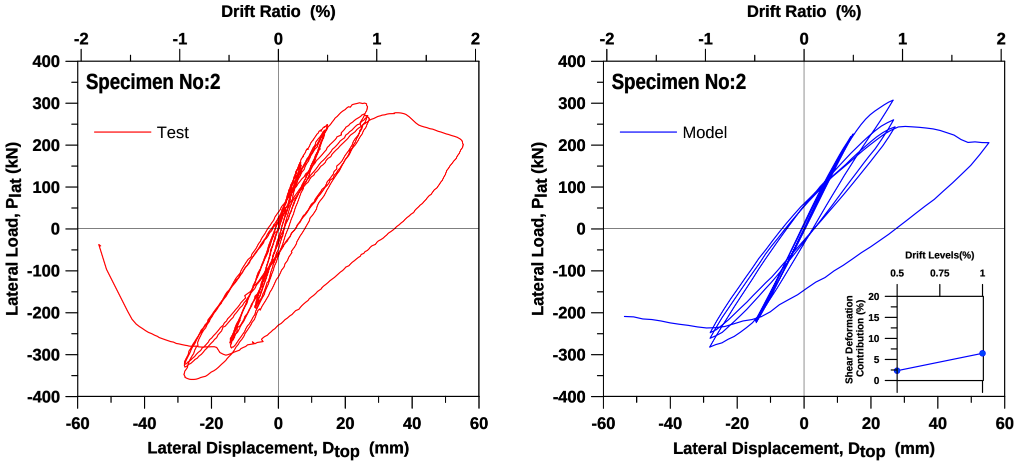

Figure 4.18. Experimentally Observed and Analytically Predicted Lateral Load vs Top Displacement Results for Specimen No:2 (Sezen, 2002)

The column specimen fails under a flexural mode, due to the buckling of longitudinal bars. Model predictions are consistent with this behavior, with limited contribution of shear deformation to lateral displacement, as depicted in Figure 4.19.

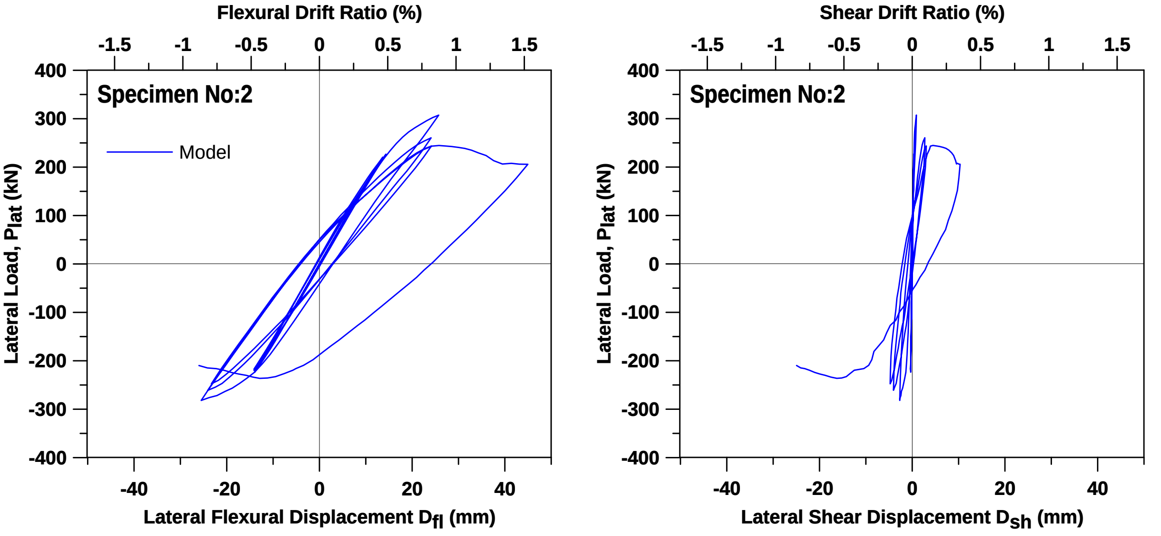

Figure 4.19. Flexural and Shear Deformation vs. Lateral Load for Specimen No:2 (Sezen, 2002)

Finally, Specimen No:4 was tested under with low axial load (15% of axial load capacity), similarly to Specimen No:1. However, top displacement history of this specimen differs from the other two specimens tested by Sezen and Moehle (2002). The specimen was subjected to reversed cyclic followed by monotonic top displacement, as illustrated in Figure 4.20, until it lost its lateral load carrying capacity. After the specimen lost its lateral load carrying capacity, it was pulled back to the zero displacement and axially loaded until it fails under axial load. The main purpose of this different loading type was to investigate the axial load carrying capacity of columns that have experienced significant damage under during an earthquake.

Test observations for Specimen No:4 showed that, this column failed under flexural dominant behavior, due to bar buckling at approximately 2.5% drift level. In the model estimation, shear deformation contribution is less dominant in overall lateral response, which is consistent with the test results.

The lateral load capacity prediction and the drift capacity prediction (2.5% drift) of the model are reasonable. After reaching the lateral load capacity, strength of the column decreases significantly according to test observations. However, the model predicts a less-pronounced and gradual strength degradation, since bar buckling behavior is not implemented in the model formulation.

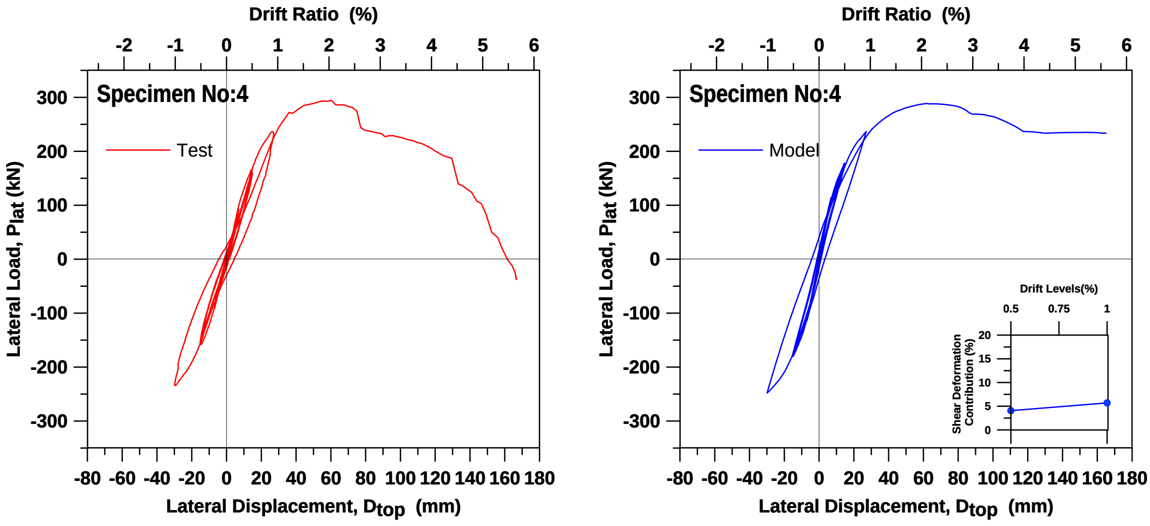

Figure 4.20. Experimentally Observed and Analytically Predicted Lateral Load vs Top Displacement Results for Specimen No:4 (Sezen, 2002)

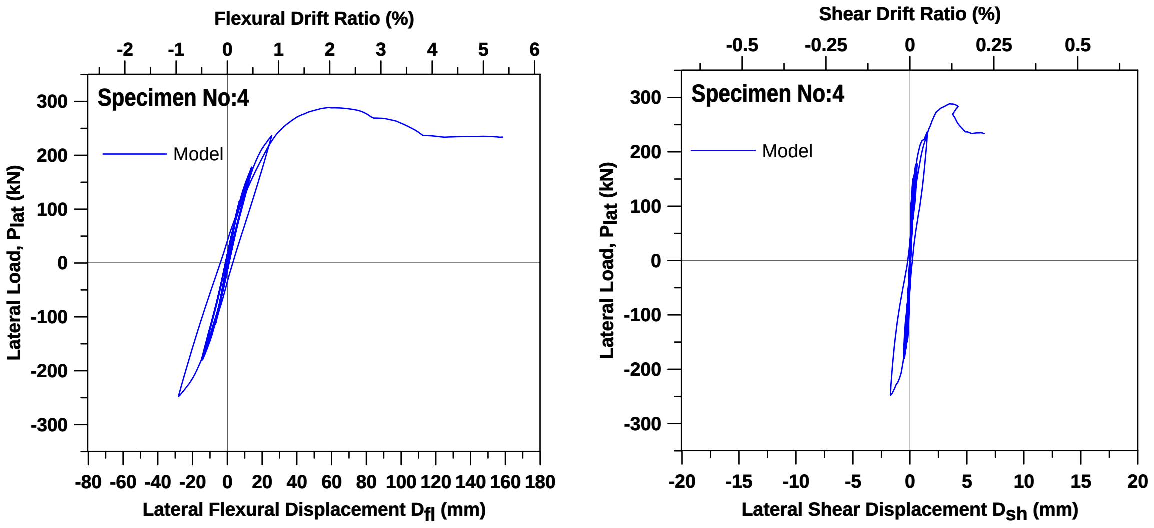

Figure 4.21. Flexural and Shear Deformation vs. Lateral Load for Specimen No:4 (Sezen, 2002)

For Specimen No:4, flexural and shear deformation versus lateral load response predictions of the model are provided in Figure 4.21. As illustrated in figure, flexural deformations constitute almost the entire lateral displacement of this specimen, and shear response is almost linearly elastic, since the governing mode of behavior of this column is flexural, as also observed during the test.

4.3. Priestley and Benzoni (1996) Specimens

Priestley and Benzoni (1996) tested two large scale circular specimens that were described in Chapter 3. Column 1 was expected to fail in flexure. By increasing the number of longitudinal bars and increasing the spacing of transverse reinforcement, Column 2 was designed to fail in shear. Cyclic steel stress strain model parameters R_0, a_1 and a_2 were calibrated for these specimens according to prior recommendations of Menegetto Pinto (1973), as applied for the Lynn (2001) specimens, with the values of 20, 18.5 and 0.15, respectively.

Test observations for Column 1 indicated that, as expected, the specimen presented flexural controlled behavior behavior and failure, reaching drift level of 3% and ductility level of 10. Due to the unsymmetrical displacement history that was applied on the column specimen, in the negative loading, a drift capacity of approximately 3.5% was reached.

The model gives a reasonably prediction in terms of the overall response, only exception is strength degradation starting at last drift level in negative loading direction is not captured well (Figure 4.22). The lateral load capacity of the column is in good agreement. The initial stiffness of the column is well predicted, and prediction of the pinching behavior is reasonable. Flexural and shear deformation contributions to the response are shown in Figure 4.22. Shear deformation contribution is limited, and the shear response is close to linear elastic, which is consistent with the experimentally observed flexural dominant response of this column.

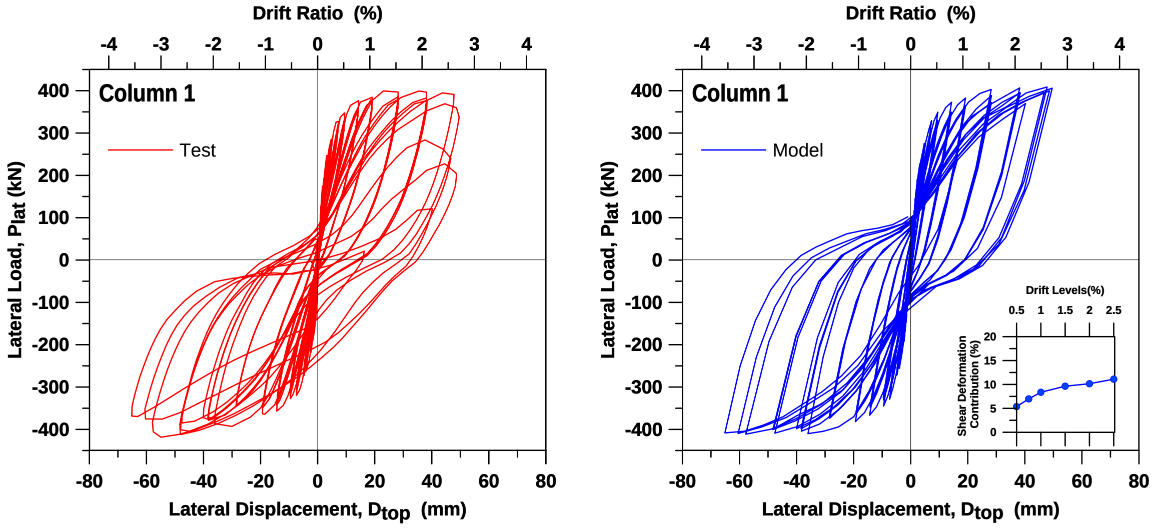

Figure 4.22. Experimentally Observed and Analytically Predicted Lateral Load vs Top Displacement Results for Specimen 1 (Priestley and Benzoni, 1996)

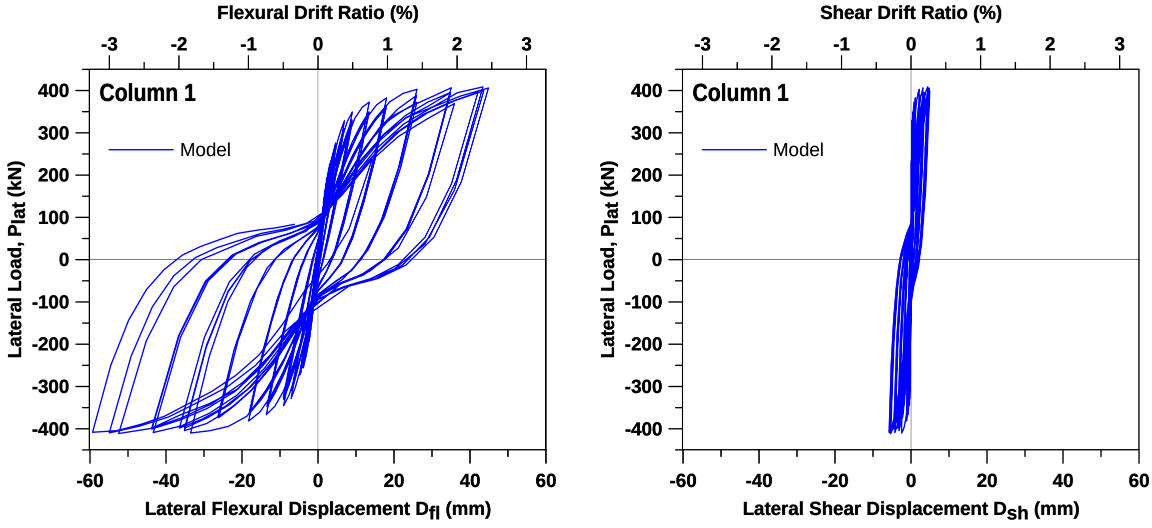

Figure 4.23. Flexural and Shear Deformation vs. Lateral Load for Column 1 (Priestley and Benzoni, 1996)

Column 2 was designed to fail in shear. Number of longitudinal bars in this specimen were increased to two times of the Column 1 to increase the flexural strength of the column and make it prone to shear failure.

Due to its higher flexural capacity, Column 2 reached a higher lateral load capacity compared to Column 1. However, its ductility capacity coefficient reduced from 10 to 4, and its drift capacity decreased from 3.5% to less than 2%.

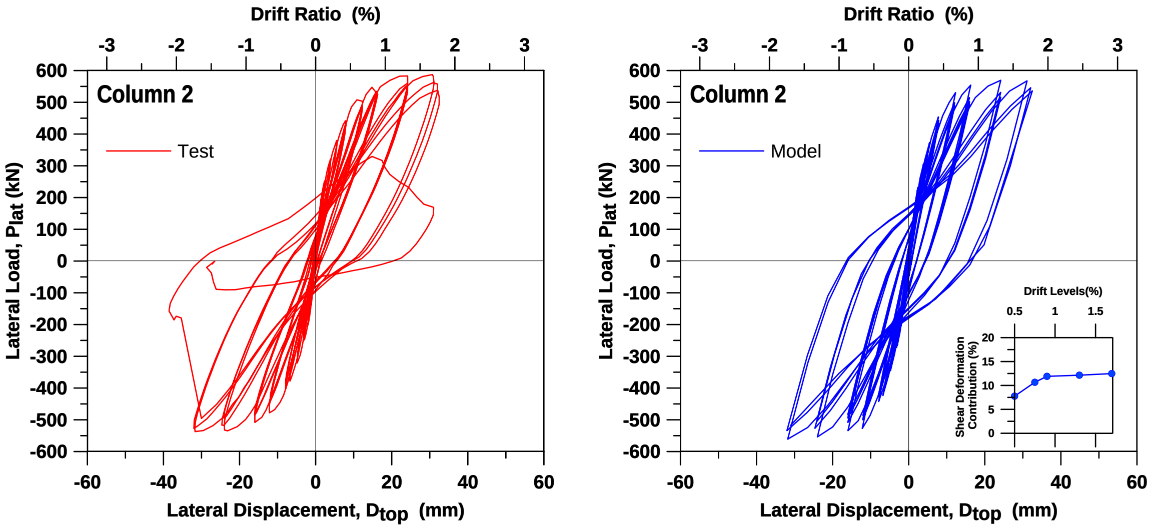

Figure 4.24. Experimentally Observed and Analytically Predicted Lateral Load vs Top Displacement Results for Column 2 (Priestley and Benzoni, 1996)

The model prediction slightly underestimates the lateral load capacity of this column, especially in the positive loading direction. More significantly, the model does not predict the sudden strength degradation due to shear failure at the negative 1.5%-2% drift level (Figure 4.24). So overall, for this particular column specimen, the model failed to accurately simulate the experimentally-observed shear failure and predict the relatively low drift capacity. Yet, model estimations for the lateral load capacity, stiffness, and ductility characteristics were reasonable. Since the model was not able to predict the shear failure, the flexural deformation contribution in the model results is dominating (Figure 4.25).

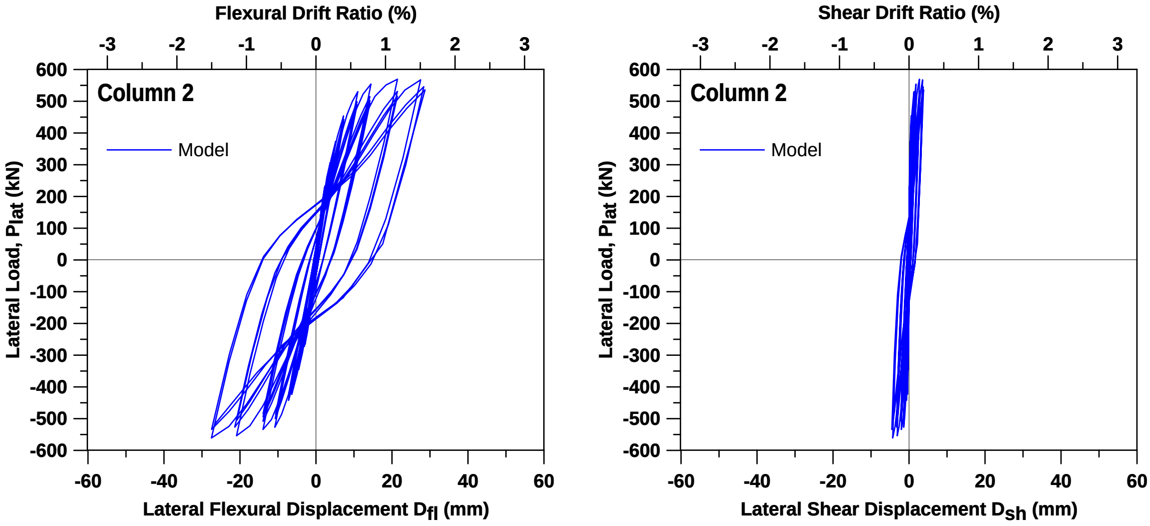

Figure 4.25. Flexural and Shear Deformation vs. Lateral Load for Column 2 (Priestley and Benzoni, 1996)

4.4. Shanmugam (2009) Specimens

Shanmugam (2009) tested two column specimens that were designed to experience flexural failure modes, with high transverse reinforcement ratios and relatively large shear span to depth ratios. Confinement was very effective for both columns, due to the low spacing and high volumetric ratio of transverse circular hoops. Therefore, concrete material properties were calibrated with respect to confinement equations as described in Chapter 3. Cyclic steel parameters of R_0, a_1 and a_2 were selected similarly to the Lynn (2001) and Priestley and Benzoni (1996) specimens, as 20, 18.5 and 0.15, respectively. Highly ductile flexural behavior was observed for both specimens. The columns were able to maintain their lateral load capacities up to very higher drift levels. For specimen H/D=3 T/M=0 1.32%, the model predicted the lateral load capacity and and drift capacity (at initiation of strength degradation) in agreement with the experimental results (Figure 4.26). Initial stiffness estimation was also reasonable. The experimentally-observed strength degradation initiated at 8% drift ratio in the positive loading direction, which was reasonably simulated by the model.

However, the area under the hysteretic load-displacement loops was significantly overestimated by the model. A possible reason for this is the incapability of the model to simulate bar buckling, not as a failure mode but its effect on the hysteretic shape of the stress-strain loops of reinforcing steel bars. Therefore, similar to Specimen No:1 (Sezen and Moehle, 2002) the modified negative strain hardening value (0.3%) was implemented and result is shown in Figure 4.26.

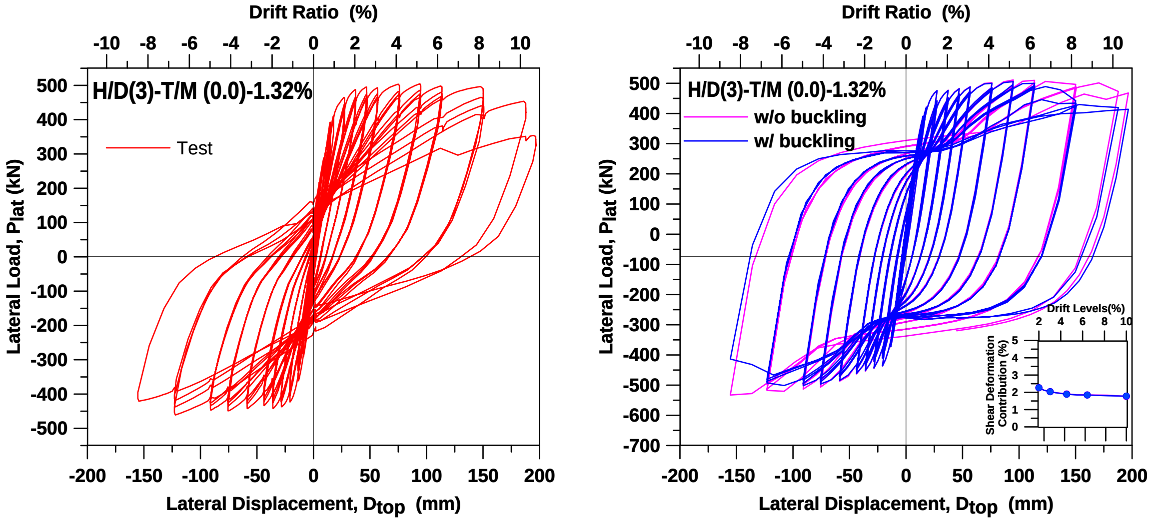

Figure 4.26. Experimentally Observed and Analytically Predicted Lateral Load vs Top Displacement Results for Specimen H/D=3 T/M=0 1.32% (Shanmugam, 2009)

Figure 4.27 shows the analytical model predictions of lateral load vs. flexural and shear deformations responses for specimen H/D=3 T/M=0 1.32% (w/ buckling). The model predicted a flexural-dominated response, with almost linear elastic shear behavior, which is consistent with the experimentally-observed behavior of the column.

As the last specimen for validation of the model, specimen H/D=6 T/M=0 0.73% (Shanmugam, 2009) had a larger shear span to depth ratio (M/VD=6) and a lower transverse reinforcement volumetric ratio. In addition, the applied top displacement history was different from the previous specimen. Since the stroke capacity of horizontal the actuator was limited, after 6% drift, the column specimen was tested under repeated cyclic loading in the positive loading direction only.

This allowed reaching a drift level of more than 12% during the test. This column also exhibited a very ductile flexural response, as expected, and strength degradation was not observed during the test (Figure 4.28).

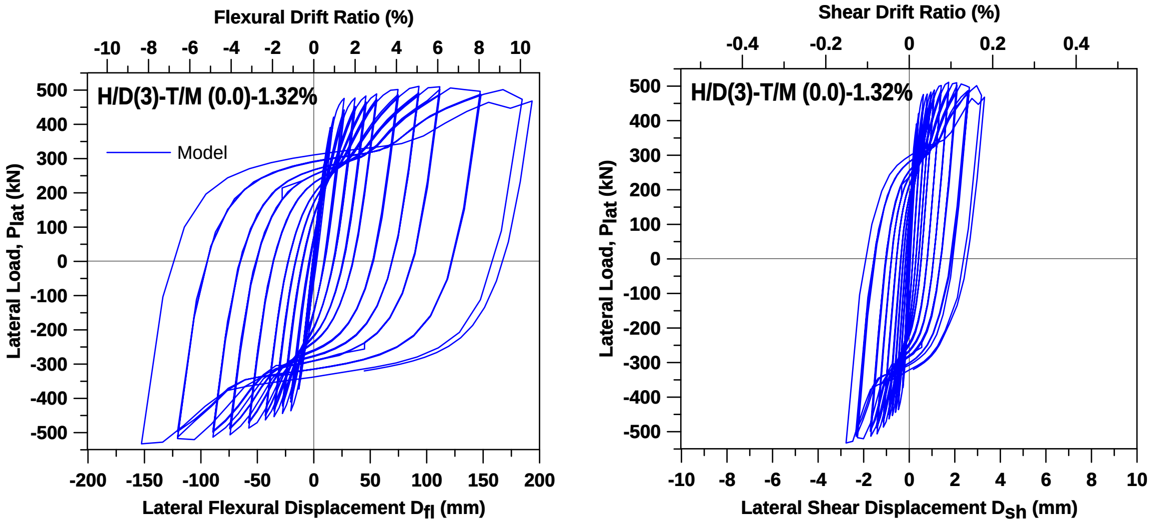

Figure 4.27. Flexural and Shear Deformation vs. Lateral Load for Specimen H/D=3 T/M=0 1.32% (Shanmugam, 2009)

The analytical and experimental lateral load vs. top displacement responses of this specimen are compared in Figure 4.28. As it can be observed in the figure, the model prediction of the response is reasonably well in terms of lateral load capacity and initial stiffness. Similarly to the previous specimen, the model predicts wider load-displacement loops compared to the test result, especially at higher drift levels. Moreover, the model predicts slightly higher lateral load capacity at last drift levels in positive loading direction. Besides, lateral load capacity estimation is in good agreement in negative loading direction.

As shown in Figure 4.29, the model prediction for this specimen is a flexural dominant response. Shear deformation contribution to top displacement is negligible and the shear response is almost linear elastic.

This is consistent with the experimentally-observed behavior mode of the specimen, and is also expected since this specimen is the most slender of all columns investigated in this study, with the largest shear span to depth ratio of 6.

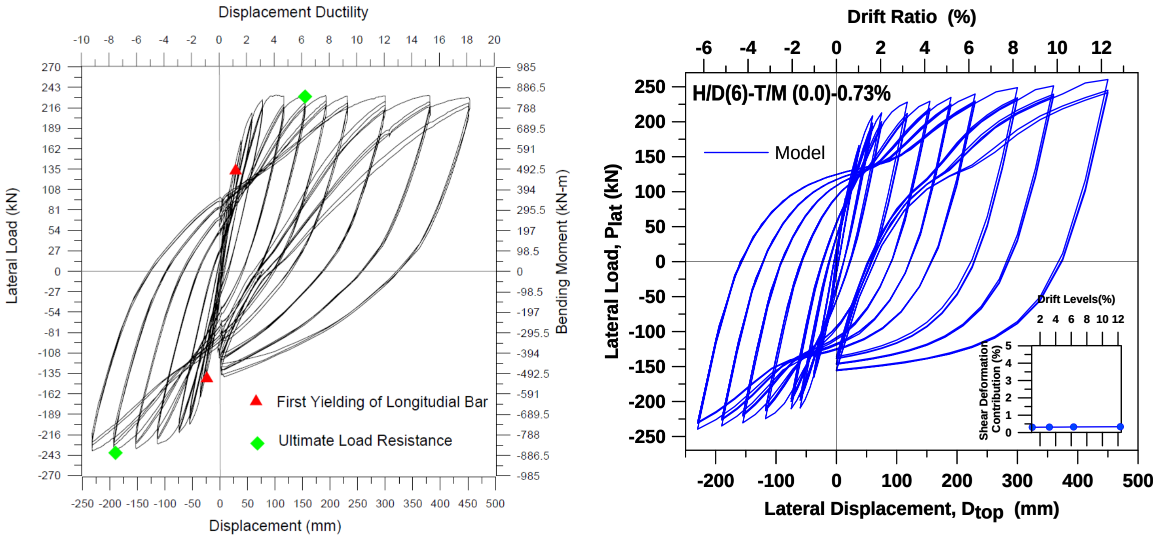

Figure 4.28. Experimentally Observed and Analytically Predicted Lateral Load vs Top Displacement Results for Specimen H/D=6 T/M=0 0.73% (Shanmugam, 2009)

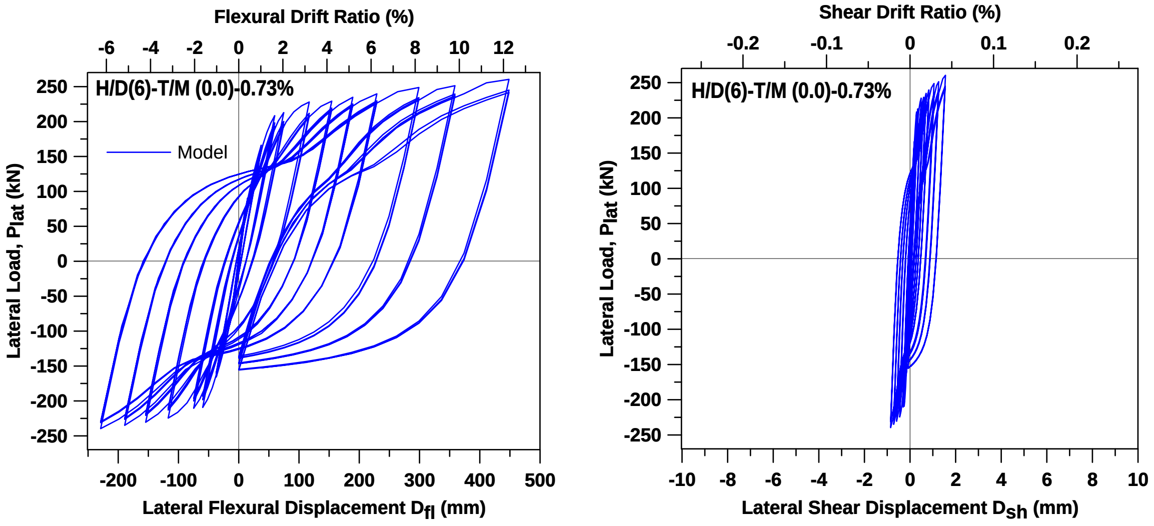

Figure 4.29. Flexural and Shear Deformation vs. Lateral Load for Specimen H/D=6 T/M=0 0.73% (Shanmugam, 2009)

5. CONCLUSION

5.1. Overview

The purpose of the study was to investigate a relatively simple yet reliable analytical modeling approach for simulating the hysteretic lateral load response of reinforced concrete columns that experience either flexure-controlled or shear-controlled failures, or a combination of the two. A finite element modeling methodology developed previously for reinforced concrete structural walls was adopted, calibrated, and validated against test results obtained from the literature for a variety of column specimens with different response characteristics. The constitutive panel element formulation of the finite element modeling approach is based on a fixed crack angle modeling methodology. Constitutive material models used incorporate the effects of compression softening, tension stiffening, hysteretic biaxial damage, strain localization, shear aggregate interlock effects, and dowel action. A simple modeling approach, using a rotational spring at the column-pedestal interface, was also implemented to consider strain penetration effects on the longitudinal reinforcing bars embedded in the pedestal.

The model was extensively calibrated and experimentally validated against test results for a total of twelve column specimens tested as part of four experimental programs (Lynn, 2001; Sezen and Moehle 2002, Benzoni and Priestley, 1996; Shanmugam 2009), which were observed to experience both flexure-dominated behavior and shear-controlled failure modes. For consistency, the same model formulation and calibration methodology was used for all column specimens investigated. Model results were compared with test measurements, mostly in terms of lateral load vs. top displacement responses of the columns. Although experimental results for local responses and deformations were not available, local response predictions of the analytical model (shear vs. flexural deformation components of lateral displacement, displacement profile along column height, longitudinal strains at column base) were also presented.

5.2. Conclusion

The conclusions derived from comparison of model response predictions and test results for the column specimens investigated in this study are as follows:

- Overall, the adopted finite element modeling methodology was found to be effective in simulating the response characteristic of reinforced concrete columns with different shear span to depth ratios, cross-sectional geometries, longitudinal and transverse reinforcement configurations, and axial load levels. Model predictions for the lateral load vs. top displacement responses were found to be in reasonable agreement with test results for most of the column specimens investigated, in terms of their lateral load capacity, lateral stiffness, drift capacity (ductility), lateral load degradation, cyclic degradation of lateral stiffness, and pinching behavior. Considering that the same model formulation was used and the same calibration methodology (for the number of model elements used, geometric discretization of the cross-section, and calibration of material parameters) was adopted for all of the column specimens, and that no ad-hoc calibration was performed to improve the model predictions, the model can be said to be successful in capturing the response characteristics of the columns investigated.

- Importantly, the model was able to predict a flexure-controlled response for the specimens that experienced predominantly flexural responses during the experiments, and a shear-controlled failure mode (with significantly lower drift capacity and more pronounced pinching) for the specimens that ultimately failed in shear during testing. Analytical results obtained using the model for the contribution of flexural and shear deformations to the top displacement of the columns were found to be consistent with the experimentally-observed failure mode of most of the column specimens investigated.

Therefore, the model is effective in differentiating between a flexure-dominant response or a shear-controlled failure of a column, based on only the geometric and reinforcement characteristics of a column (as well as axial load level), in a purely mechanical manner, without the need to use any empirical relationship that defines the shear capacity or shear response characteristics.

- Local response and deformation predictions of the model could not be validated against experimental measurements, since local deformation measurements were not reported in most of the experimental studies. However, the local response predictions obtained from the model results (contribution of flexural and shear deformations to lateral displacement, longitudinal strains at column base, profile of lateral displacements along column height) were all reasonable and in agreement with the overall response predictions obtained. Similar to structural walls, the distribution (along column width) of longitudinal strains at the base of the columns were predicted to be moderately nonlinear, especially for columns with lower shear-span-to-depth ratios.

5.3. Recommendations for Future Studies

Based on result of this study, the following recommendations for future research can be made:

- For columns with large spacing of transverse reinforcement, buckling of longitudinal reinforcing bars is likely and may have significant effect on the drift capacity of a column with flexure-controlled behavior. However, this failure mode cannot be captured by the analytical model used in this study, since rebar buckling is not considered in the present model formulation. The constitutive relationship implemented in the model for reinforcing steel can be improved to incorporate bar buckling behavior.

- For modeling of the response of columns with deficient anchorage characteristics or inadequate lap splices, hysteretic bond stress vs. slip springs that connect the concrete panel elements with discrete rebar elements can be implemented in the model formulation.

- The present model formulation is applicable for one-directional lateral loading only. Column response under bi-directional lateral loads and torsional effects cannot be simulated by the model. It should be investigated whether the model formulation can be extended for bi-directional lateral loading, for a more reliable design or performance assessment that incorporates three-dimensional analysis under bi-directional earthquake demands.

REFERENCES

1. Belarbi, A. and T. T. Hsu, "Constitutive Laws of Concrete in Tension and Reinforcing Bars Stiffened by Concrete", *Structural Journal*, Vol. 91, No. 4, pp. 465–474, 1994.

2. Chang, G. and J. B. Mander, "Seismic Energy Based Fatigue Damage Analysis of Bridge Columns: Part 1-Evaluation of Seismic Capacity", *NCEER Technical Report*, Vol. No: NCEER-94-0006, State University of New York, Buffalo.

3. Clarke, M. J. and G. J. Hancock, "A Study of Incremental-Iterative Strategies for Non-linear Analyses", *International Journal for Numerical Methods in Engineering*, Vol. 29, No. 7, pp. 1365–1391, 1990.

4. Coleman, J. and E. Spacone, "Localization Issues in Force-Based Frame Elements", *Journal of Structural Engineering*, Vol. 127, No. 11, pp. 1257–1265, 2001.

5. D'Ambrisi, A. and F. C. Filippou, "Modeling of Cyclic Shear Behavior in RC Members", *Journal of Structural Engineering*, Vol. 125, No. 10, pp. 1143–1150, 1999.

6. Dhakal, R. P. and K. Maekawa, "Modeling for Postyield Buckling of Reinforcement", *Journal of Structural Engineering*, Vol. 128, No. 9, pp. 1139–1147, 2002.

7. Elmorsi, M., M. R. Kianoush and W. Tso, "Nonlinear analysis of cyclically loaded reinforced concrete structures", *Structural Journal*, Vol. 95, No. 6, pp. 725–739, 1998.

8. Fillipou, F., E. Popov and V. Bertero, "Effect of Bond Deterioration on Hysteretic Behaviour of Reinforced Concrete Joints. Report EERC 83-19", *Earthquake Engineering Research Center, University of California, Berkeley*, 1983.

9. Fischinger, M., T. Vidic, J. Selih, P. Fajfar, H. Zhang and F. Damjanic, “Validation of a macroscopic model for cyclic response prediction of RC walls”, *Computer Aided Analysis and Design of Concrete Structures*, Vol. 2, pp. 1131–1142, 1990.

10. Galal, K. E. and A. Ghobarah, “Flexural and Shear Hysteretic Behaviour of Reinforced Concrete Columns with Variable Axial Load”, *Engineering Structures*, Vol. 25, No. 11, pp. 1353–1367, 2003.

11. Gullu, M. F., *Finite Element Modeling of Reinforced Concrete Structural Walls*, Master’s Thesis, Bogazici University, 2013.

12. Gullu, M. F. and K. Orakçal, “Nonlinear Finite Element Modeling of Reinforced Concrete Structural Walls”, *Proceedings, 16th World Conference on Earthquake Engineering, Santiago, Chile*, 4134, 2017.

13. He, X. and A. Kwan, “Modeling Dowel Action of Reinforcement Bars for Finite Element Analysis of Concrete Structures”, *Computers & Structures*, Vol. 79, No. 6, pp. 595–604, 2001.

14. Hu, D. and M. Barbato, “Simple and efficient finite element modeling of reinforced concrete columns confined with fiber-reinforced polymers”, *Engineering Structures*, Vol. 72, pp. 113–122, 2014.

15. Kent, D. C. and R. Park, “Flexural Members with Confined Concrete”, *Journal of the Structural Division*, 1971.

16. Kolozvari, K., K. Orakcal and J. Wallace, “Shear-Flexure Interaction Modeling of reinforced Concrete Structural Walls and Columns under Reversed Cyclic Loading”, *Pacific Earthquake Engineering Research Center, University of California, Berkeley, PEER Report*, Vol. 141, No. 2015/12, 2015.

17. Kolozvari, K. I., *Analytical Modeling of Cyclic Shear - Flexure Interaction in Reinforced Concrete Structural Walls*, Ph.D. Thesis, University of California, Los

Angeles, 2013.

18. Lehman, D. E., *Seismic Performance of Well-Confined Concrete Bridge Columns*, Ph.D. Thesis, University of Michigan, 1998.

19. Lynn, A. C., *Seismic Evaluation of Existing Reinforced Concrete Building Columns*, Ph.D. Thesis, University of California, Berkeley, 2001.

20. Mander, J. B., M. J. Priestley and R. Park, “Theoretical Stress-Strain Model for Confined Concrete”, *Journal of structural engineering*, Vol. 114, No. 8, pp. 1804–1826, 1988.

21. Mansour, M., J.-Y. Lee and T. T. Hsu, “Cyclic Stress-Strain Curves of Concrete and Steel Bars in Membrane Elements”, *Journal of Structural Engineering*, Vol. 127, No. 12, pp. 1402–1411, 2001.

22. Massone, L. M., K. Orakcal and J. W. Wallace, “Modeling of Squat Structural Walls Controlled by Shear”, *ACI Structural Journal*, Vol. 106, No. 5, p. 646, 2009.

23. McDaniel, C., *Scale Effects on the Shear Strength of Circular Reinforced Concrete Columns*, Ph.D. Thesis, University of California, San Diego, 1997.

24. Menegotto, M. and E. Pinto, “Method of Analysis for Cyclically Loaded Reinforced Concrete Plane Frames Including Changes in Geometry and Non-Elastic Behavior of Elements Under Combined Normal Force and Bending”, *Proceedings,IABSE Symposium on Resistance and Ultimate Deformability of Structures Acted on by Well-Defined Repeated Loads, Lisbon, Portugal*, 1973.

25. Mourlas, C., M. Papadrakakis and G. Markou, “A computationally efficient model for the cyclic behavior of reinforced concrete structural members”, *Engineering Structures*, Vol. 141, pp. 97–125, 2017.

26. Mullapudi, T. R. and A. Ayoub, “Modeling of the Seismic Behavior of Shear-

Critical Reinforced Concrete Columns", *Engineering Structures*, Vol. 32, No. 11, pp. 3601–3615, 2010.

27. Orakcal, K., *Nonlinear Modeling and Analysis of Slender Reinforced Concrete Walls*, Ph.D. Thesis, University of California, Los Angeles, 2004.

28. Orakcal, K., D. Ulugtekin and L. Massone, "Constitutive Modeling of Reinforced Concrete Panel Behavior Under Cyclic Loading", *Proceedings, 15th World Conference on Earthquake Engineering*, Vol. 3573, 2012.

29. Osorio, E., J. M. Bairán and A. R. Marí, "Analytical Modeling of Reinforced Concrete Columns Subjected to Bidirectional Shear", *Engineering Structures*, Vol. 138, pp. 458–472, 2017.

30. Ozcebe, G., *Inelastic Response of Reinforced Concrete Columns Under Uni-Directional and Bi-Directional Load Reversals*, Ph.D. Thesis, University of Toronto, 1987.

31. Ozcebe, G. and M. Saatcioglu, "Hysteretic Shear Model For Reinforced Concrete Members", *Journal of Structural Engineering*, Vol. 115, No. 1, pp. 132–148, 1989.

32. Pang, X.-B. D. and T. T. Hsu, "Behavior of Reinforced Concrete Membrane Elements in Shear", *Structural Journal*, Vol. 92, No. 6, pp. 665–679, 1995.

33. Priestley, M. N. and G. Benzoni, "Seismic Performance of Circular Columns with Low Longitudinal reinforcement ratios", *Structural Journal*, Vol. 93, No. 4, pp. 474–485, 1996.

34. Pujol, S., *Drift Capacity of Reinforced Concrete Column Subjected to Displacement Reversals*, Ph.D. Thesis, Missouri University of Science and Technology, 2002.

35. Saatcioglu, M. and G. Ozcebe, "Response of Reinforced Concrete Columns to Simulated Seismic Loading", *Structural Journal*, Vol. 86, No. 1, pp. 3–12, 1989.

36. Saatcioglu, M. and S. R. Razvi, “Strength and Ductility of Confined Concrete”, *Journal of Structural engineering*, Vol. 118, No. 6, pp. 1590–1607, 1992.

37. Sezen, H., *Seismic Behavior and Modeling of Reinforced Concrete Building Columns*, Ph.D. Thesis, University of California, Berkeley, 2002.

38. Shanmugam, S. P., *Seismic Behavior of Circular Reinforced Concrete Bridge Columns Under Combined Loading Including Torsion*, Ph.D. Thesis, Missouri University of Science and Technology, 2009.

39. Simons, J. W. and G. H. Powell, *Solution Strategies for Statically Loaded Nonlinear Structures*, Earthquake Engineering Research Center, University of California, 1982.

40. Takeda, T., M. A. Sozen and N. N. Nielsen, “Reinforced concrete response to simulated earthquakes”, *Journal of the Structural Division*, Vol. 96, No. 12, pp. 2557–2573, 1970.

41. Thomson, J. H. and J. W. Wallace, “Lateral load behavior of reinforced concrete columns constructed using high-strength materials”, *Structural Journal*, Vol. 91, No. 5, pp. 605–615, 1994.

42. Ulugtekin, D., *Analytical Modeling of Reinforced Concrete Panel Elements Under Reversed Cyclic Loadings*, Master’s Thesis, Bogazici University, 2010.

43. Vecchio, F. J. and M. P. Collins, “The Modified Compression-Field Theory for Reinforced Concrete Elements Subjected to Shear”, *Journal Proceedings*, Vol. 83, pp. 219–231, 1986.

44. Vulcano, A., V. V. Bertero and V. Colotti, “Analytical modeling of RC structural walls”, *Proceedings of 9th world conference on earthquake engineering*, Vol. 6, pp. 41–46, 1988.

45. Xu, S.-Y. and J. Zhang, "Hysteretic Shear-Flexure Interaction Model of Reinforced Concrete Columns for Seismic Response Assessment of Bridges", *Earthquake Engineering and Structural Dynamics*, Vol. 40, No. 3, pp. 315–337, 2011.

APPENDIX A: LOCAL RESPONSES

A.1. Longitudinal Strains on Concrete

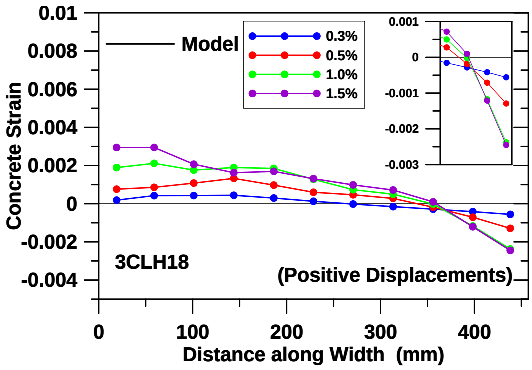

Figure A.1. Longitudinal Strain Profiles for Specimen 3CLH18 (Lynn, 2001)

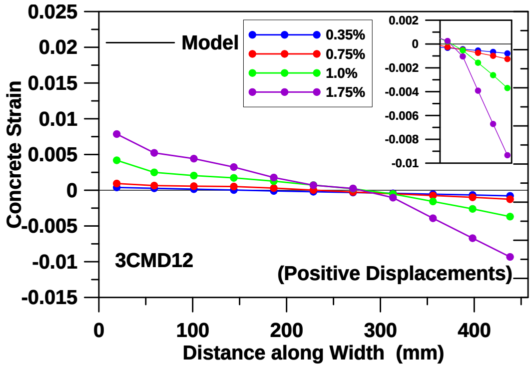

Figure A.2. Longitudinal Strain Profiles for Specimen 3CMD12 (Lynn, 2001)

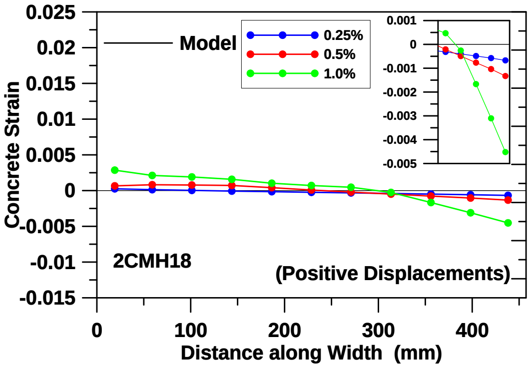

Figure A.3. Longitudinal Strain Profiles for Specimen 2CMH18 (Lynn, 2001)

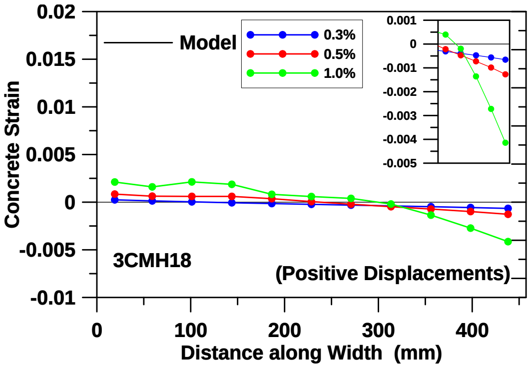

Figure A.4. Longitudinal Strain Profiles for Specimen 3CMH18 (Lynn, 2001)

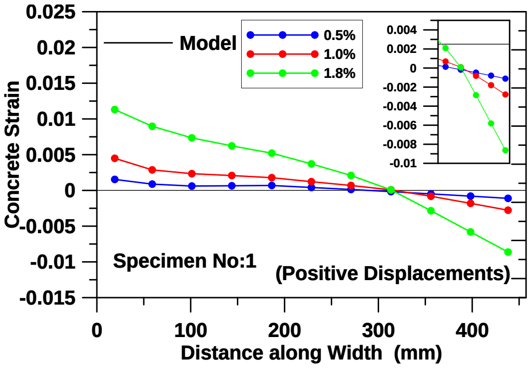

Figure A.5. Longitudinal Strain Profiles for Specimen No:1 (Sezen, 2002)

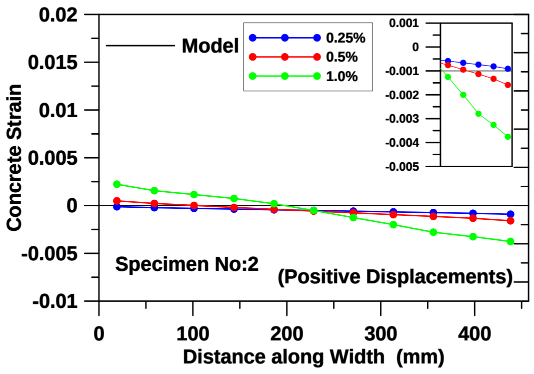

Figure A.6. Longitudinal Strain Profiles for Specimen No:2 (Sezen, 2002)

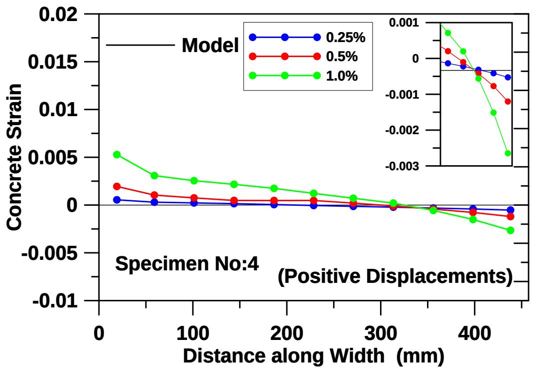

Figure A.7. Longitudinal Strain Profiles for Specimen No:4 (Sezen, 2002)

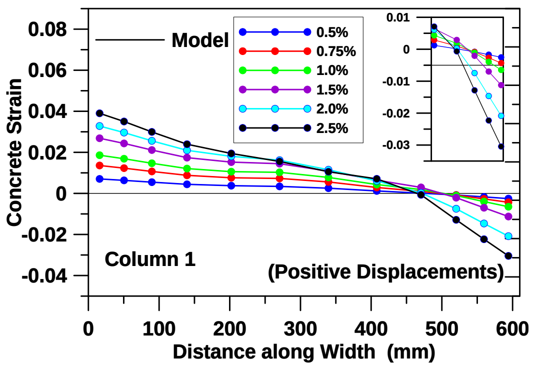

Figure A.8. Longitudinal Strain Profiles for Column 1 (Priestley and Benzoni, 1996)

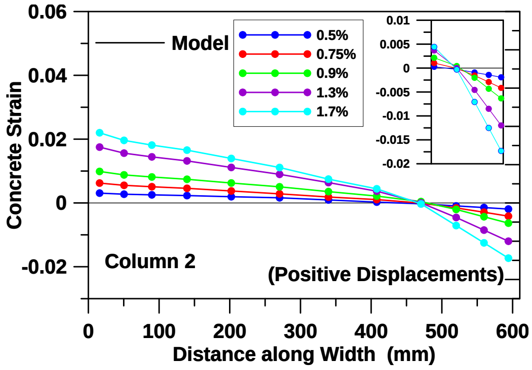

Figure A.9. Longitudinal Strain Profiles for Column 2 (Priestley and Benzoni, 1996)

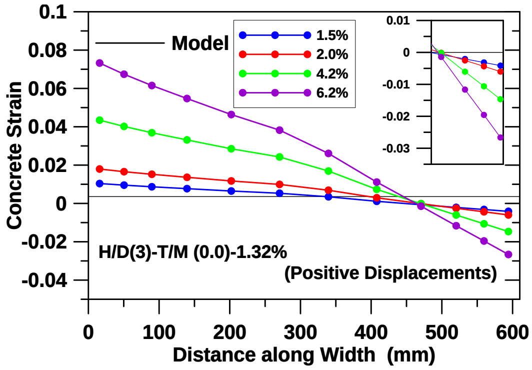

Figure A.10. Longitudinal Strain Profiles for Specimen H/D=3 T/M=0 1.32% (Shanmugam, 2009)

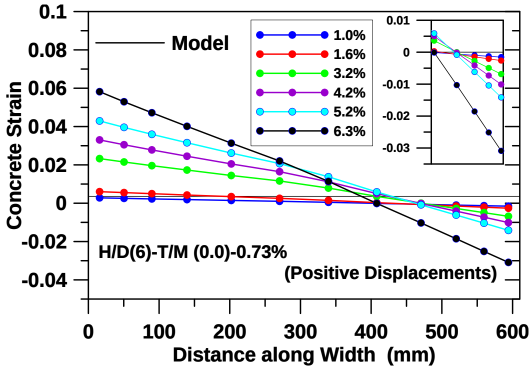

Figure A.11. Longitudinal Strain Profiles for Specimen H/D=6 T/M=0 0.73% (Shanmugam, 2009)

A.2. Displacement Profiles

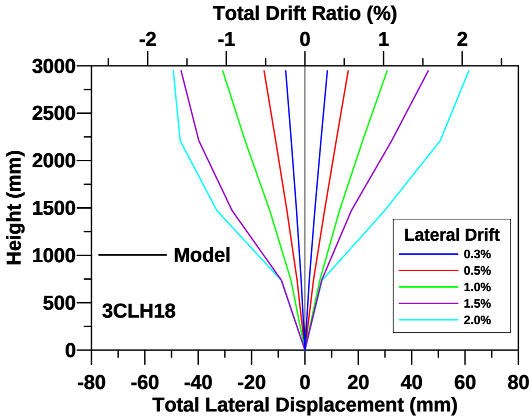

Figure A.12. Total Lateral Displacement Profiles for Specimen 3CLH18 (Lynn, 2001)

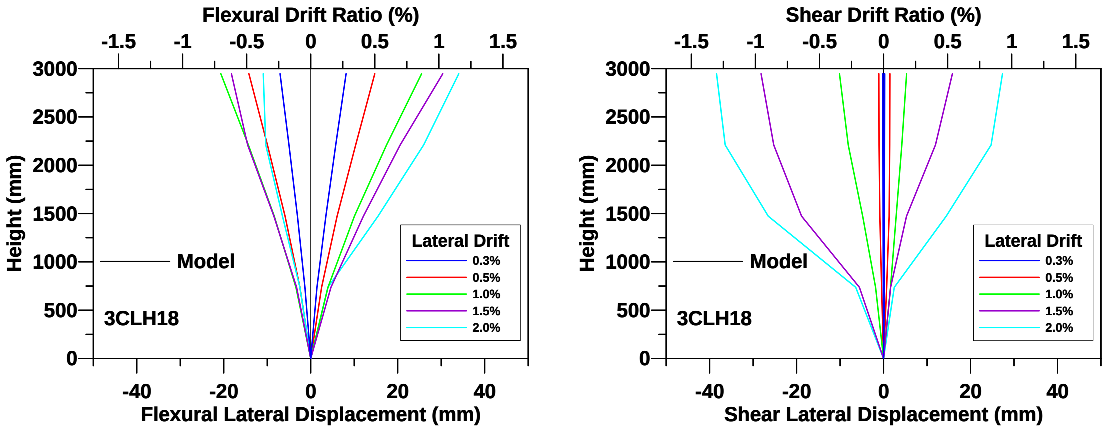

Figure A.13. Flexural and Shear Displacement Profiles for Specimen 3CLH18 (Lynn, 2001)

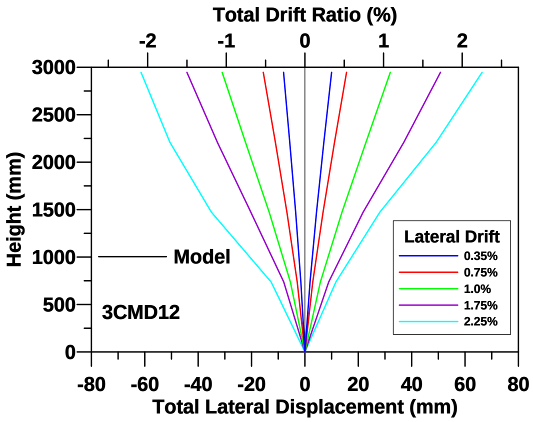

Figure A.14. Total Lateral Displacement Profiles for Specimen 3CMD12 (Lynn, 2001)

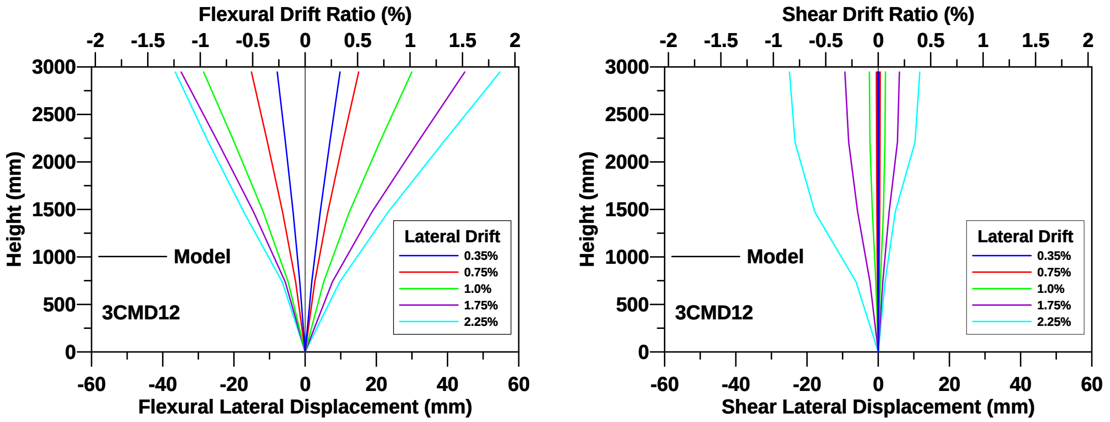

Figure A.15. Flexural and Shear Displacement Profiles for Specimen 3CMD12 (Lynn, 2001)

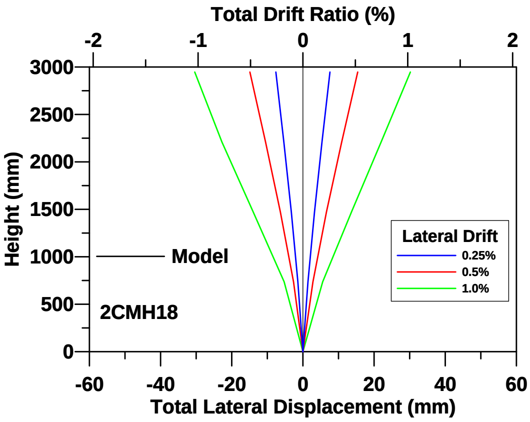

Figure A.16. Total Lateral Displacement Profiles for Specimen 2CMH18 (Lynn, 2001)

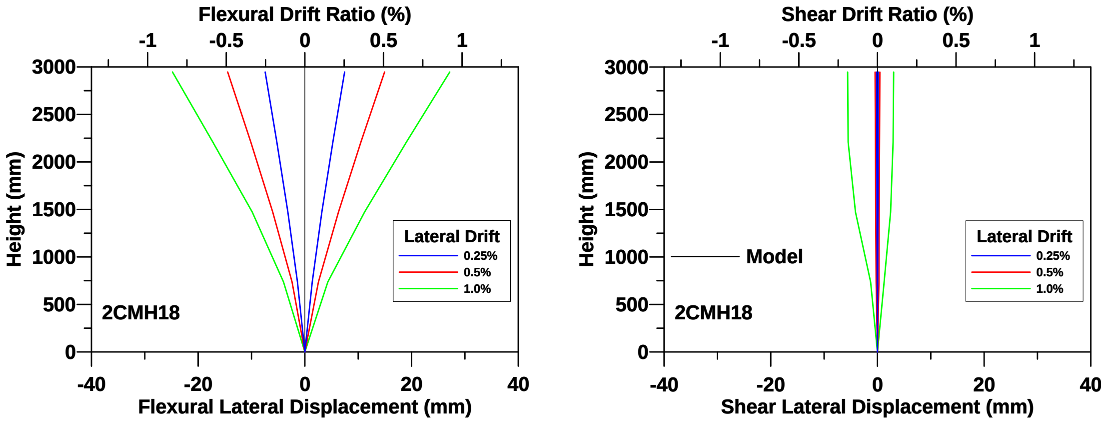

Figure A.17. Flexural and Shear Displacement Profiles for Specimen 2CMH18 (Lynn, 2001)

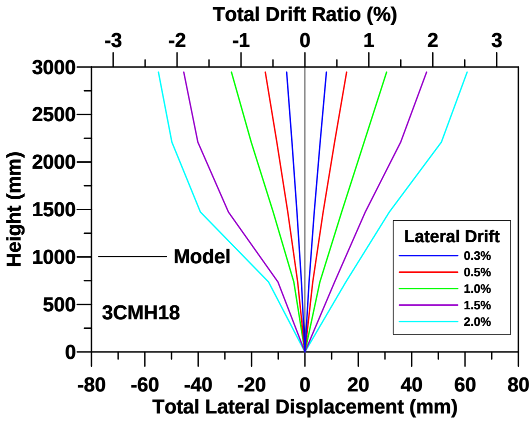

Figure A.18. Total Lateral Displacement Profiles for Specimen 3CMH18 (Lynn, 2001)

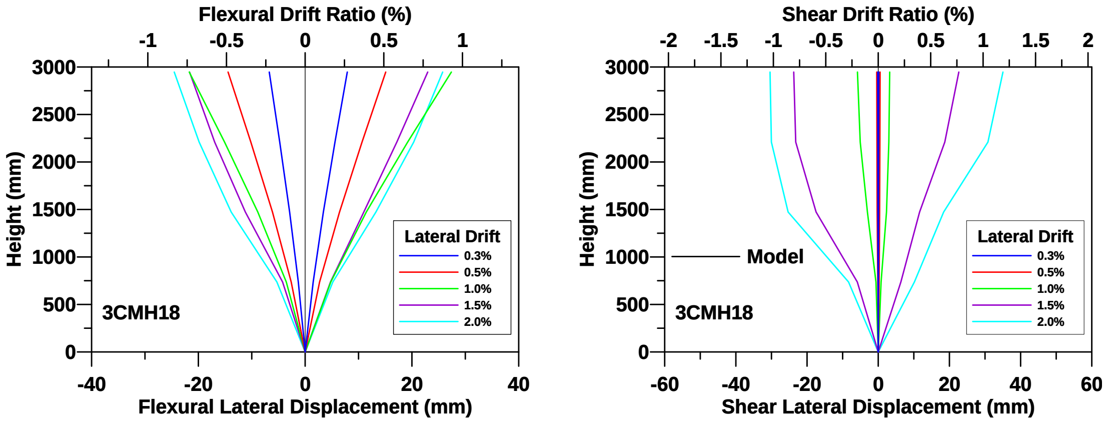

Figure A.19. Total Flexural and Shear Displacement Profiles for Specimen 3CMH18 (Lynn, 2001)

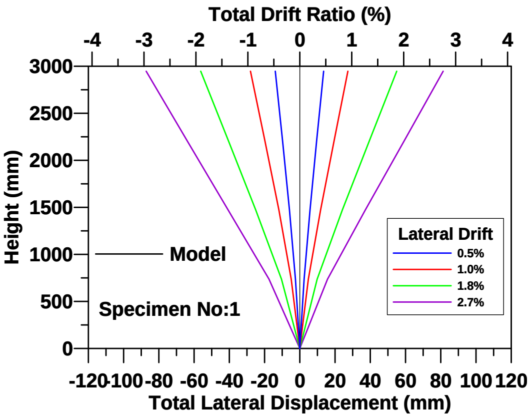

Figure A.20. Total Lateral Displacement Profiles for Specimen No:1 (Sezen, 2002)

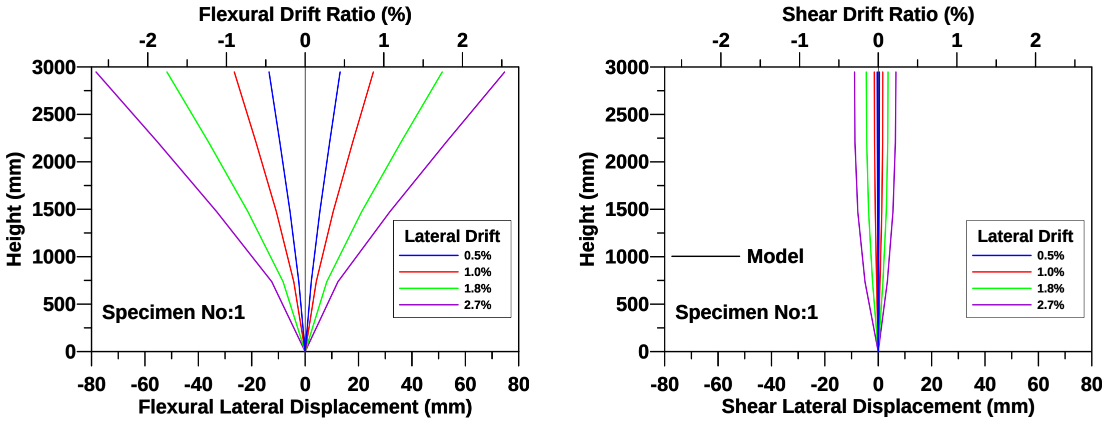

Figure A.21. Total Flexural and Shear Displacement Profiles for Specimen No:1 (Sezen, 2002)

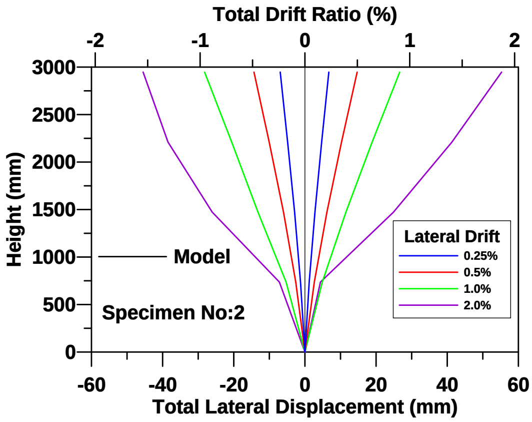

Figure A.22. Total Lateral Displacement Profiles for Specimen No:2 (Sezen, 2002)

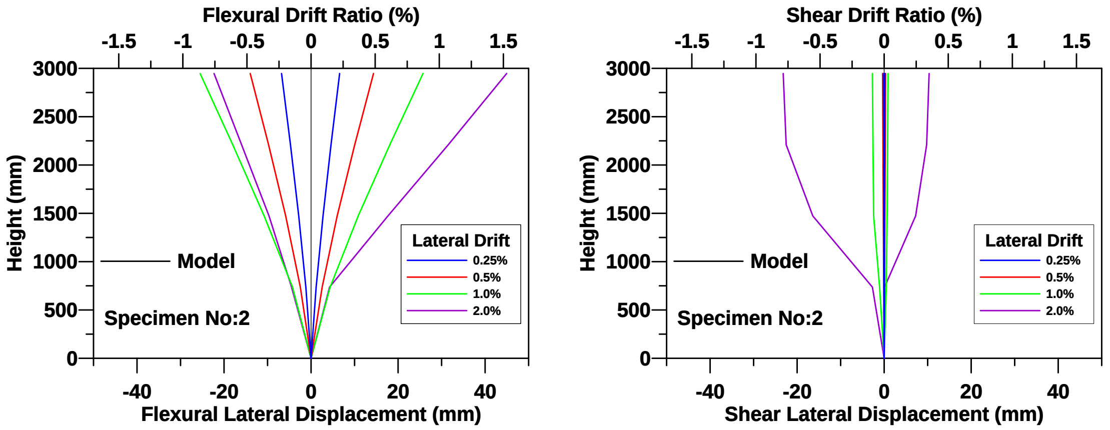

Figure A.23. Total Flexural and Shear Displacement Profiles for Specimen No:2 (Sezen, 2002)

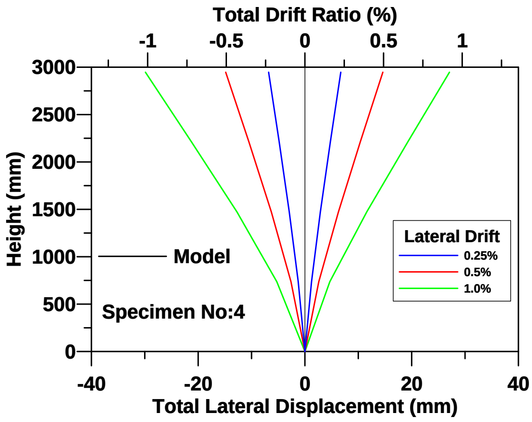

Figure A.24. Total Lateral Displacement Profiles for Specimen No:4 (Sezen, 2002)

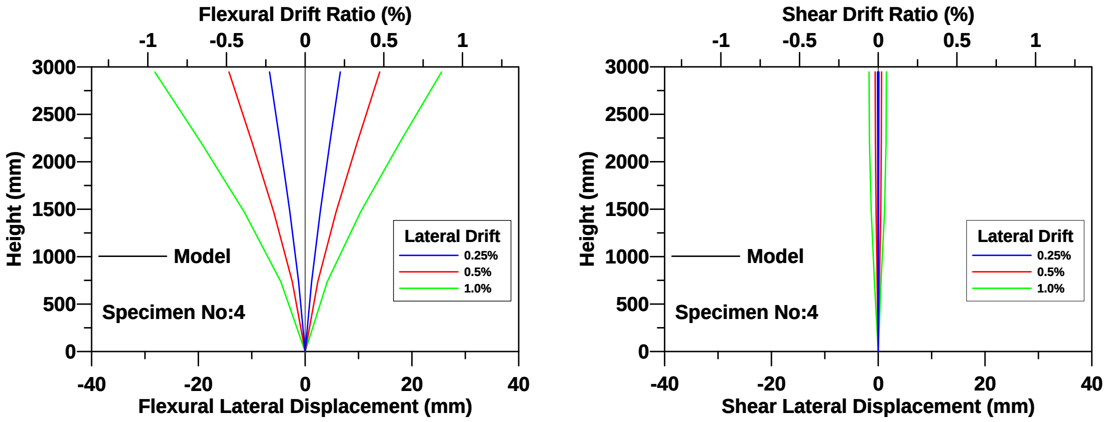

Figure A.25. Total Flexural and Shear Displacement Profiles for Specimen No:4 (Sezen, 2002)

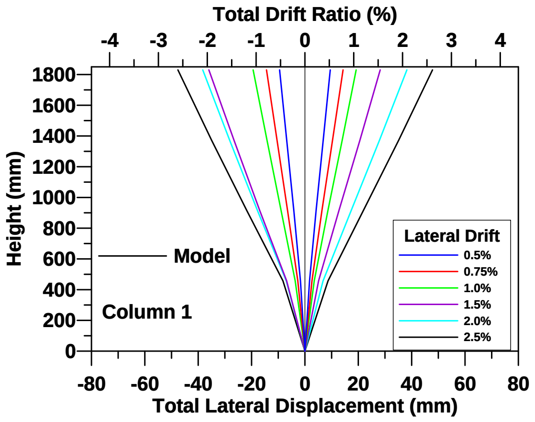

Figure A.26. Total Lateral Displacement Profiles Column 1 (Priestley and Benzoni, 1996)

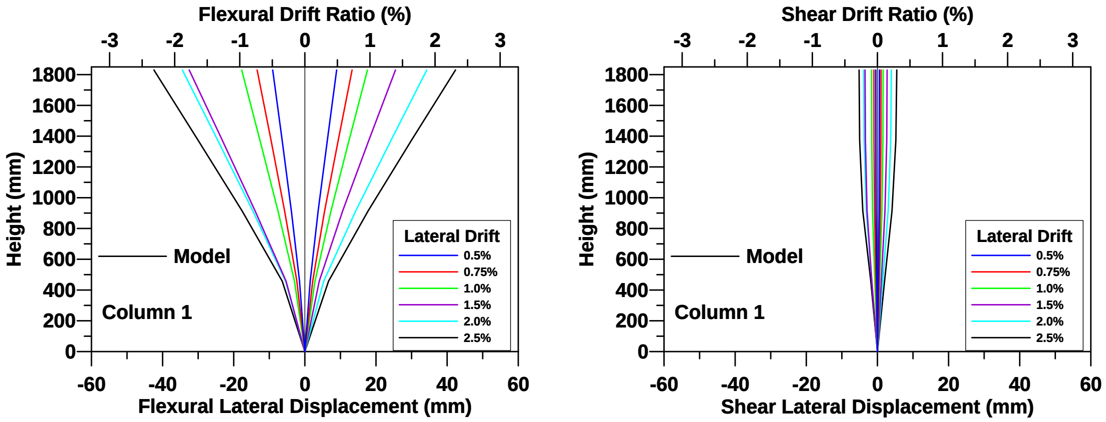

Figure A.27. Total Flexural and Shear Displacement Profiles Column 1 (Priestley and Benzoni, 1996)

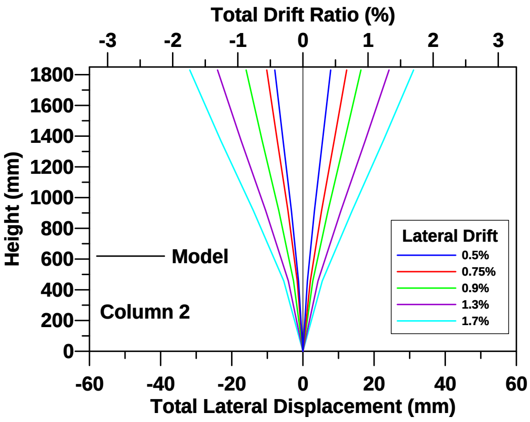

Figure A.28. Total Lateral Displacement Profiles Column 2 (Priestley and Benzoni, 1996)

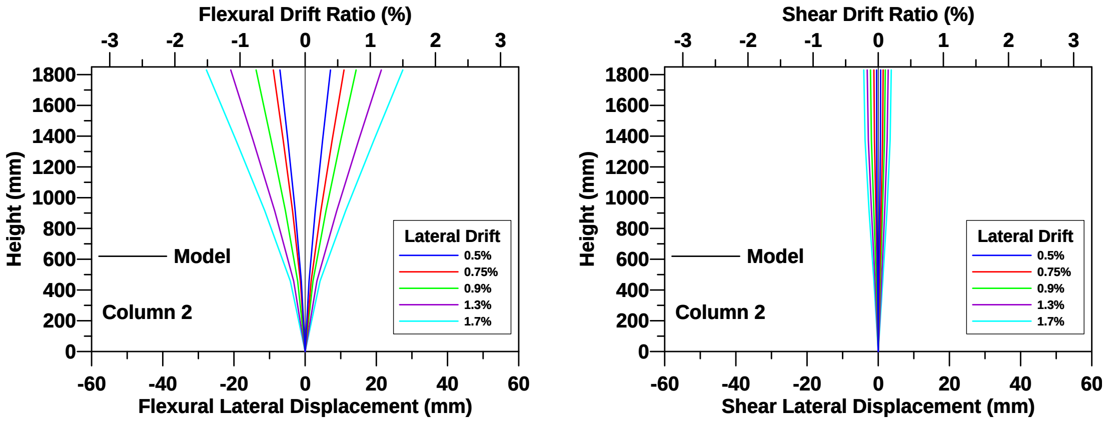

Figure A.29. Total Flexural and Shear Displacement Profiles Column 2 (Priestley and Benzoni, 1996)

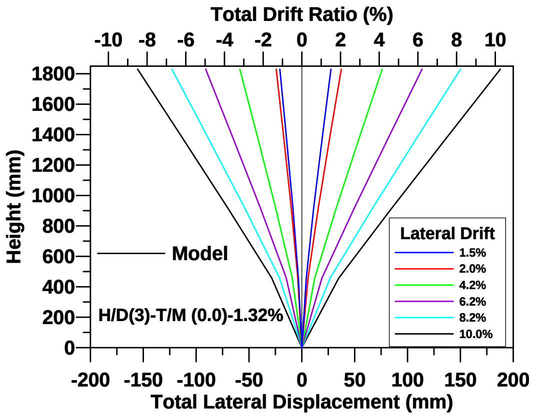

Figure A.30. Total Lateral Displacement Profiles for Specimen H/D=3 T/M=0 1.32% (Shanmugam, 2009)

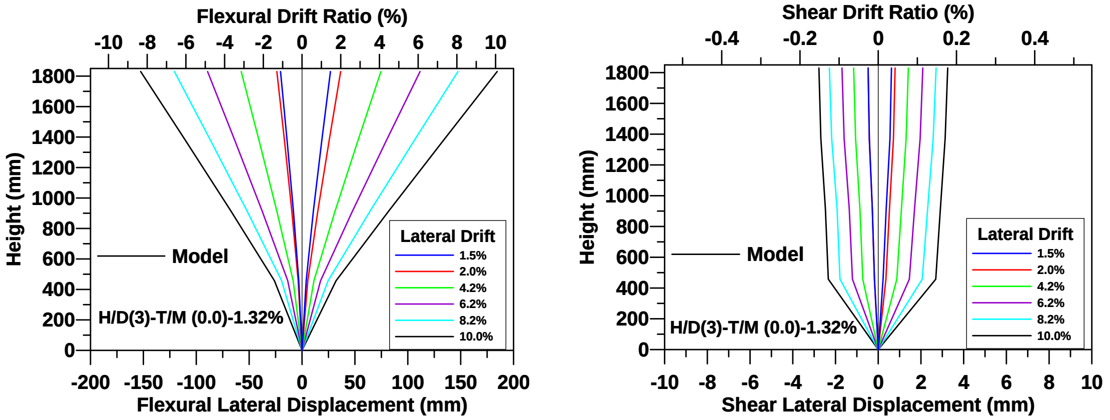

Figure A.31. Total Flexural and Shear Displacement Profiles for Specimen H/D=3 T/M=0 1.32% (Shanmugam, 2009)

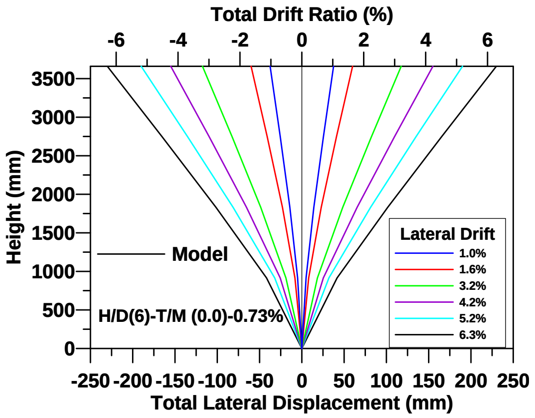

Figure A.32. Total Lateral Displacement Profiles for Specimen H/D=6 T/M=0 0.73% (Shanmugam, 2009)

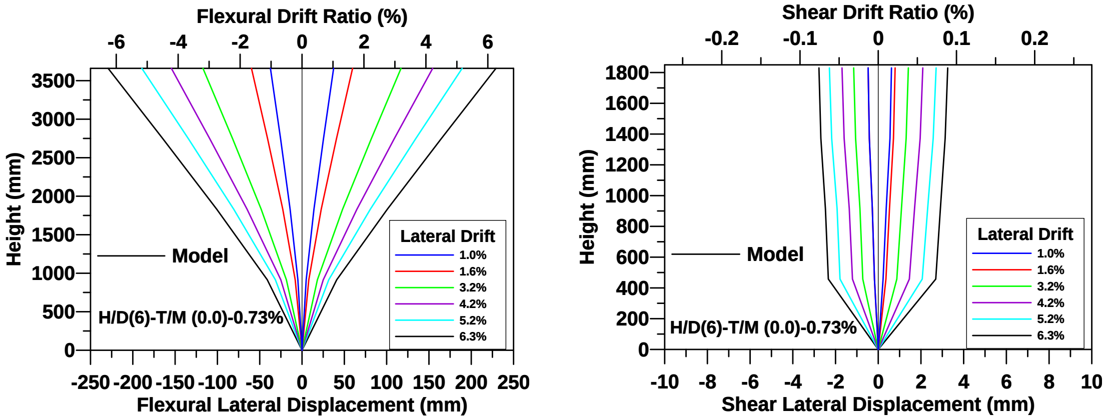

Figure A.33. Total Flexural and Shear Displacement Profiles for Specimen H/D=6 T/M=0 0.73% (Shanmugam, 2009)

A.3. Cumulative Energy Dissipation

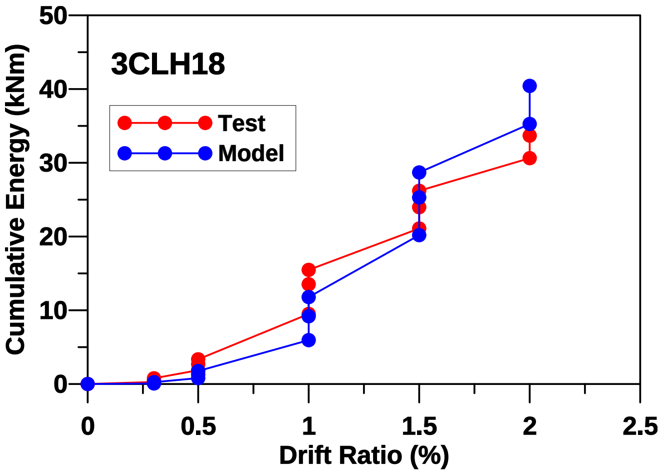

Figure A.34. Dissipated Cumulative Energy vs. Drift Level for Specimen 3CLH18 (Lynn, 2001)

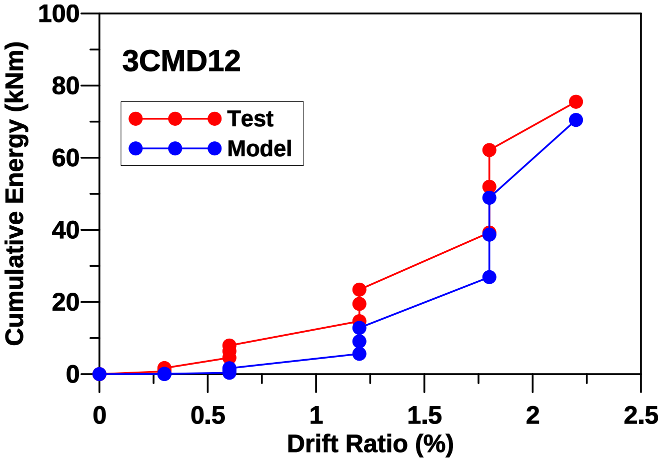

Figure A.35. Dissipated Cumulative Energy vs. Drift Level for Specimen 3CMD12 (Lynn, 2001)

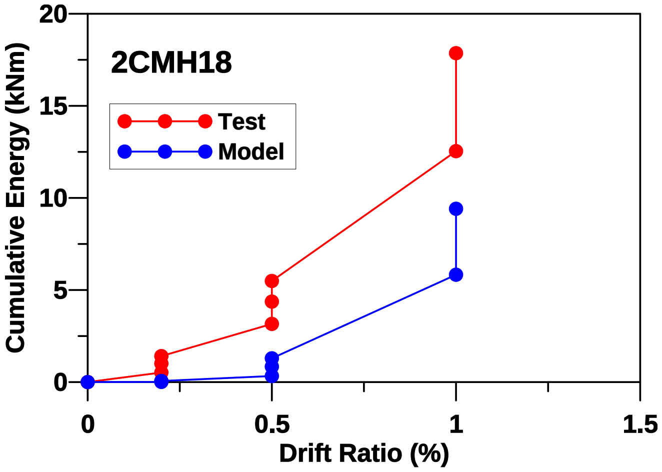

Figure A.36. Dissipated Cumulative Energy vs. Drift Level for Specimen 2CMH18 (Lynn, 2001)

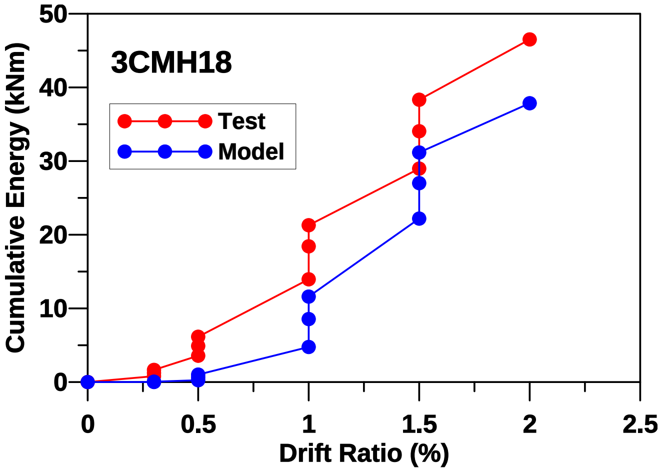

Figure A.37. Dissipated Cumulative Energy vs. Drift Level for Specimen 3CMH18 (Lynn, 2001)

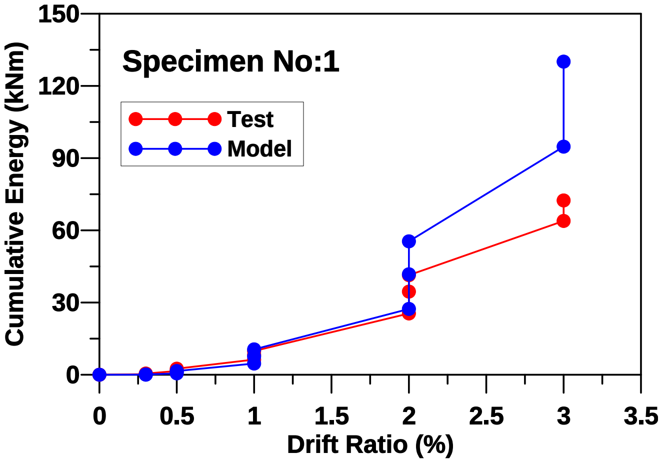

Figure A.38. Dissipated Cumulative Energy vs. Drift Level for Specimen 1 (Sezen, 2002)

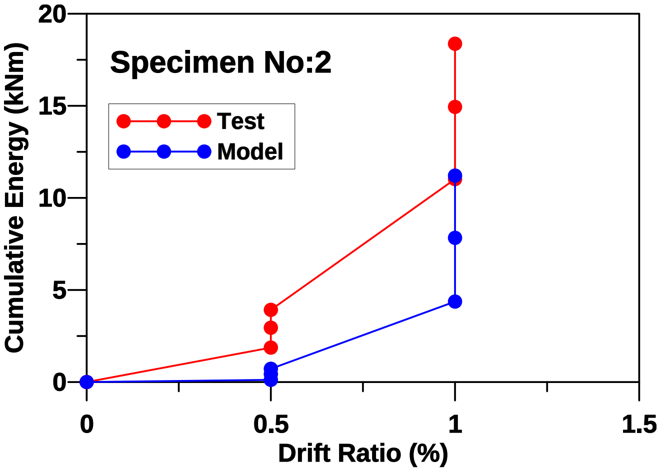

Figure A.39. Dissipated Cumulative Energy vs. Drift Level for Specimen 2 (Sezen, 2002)

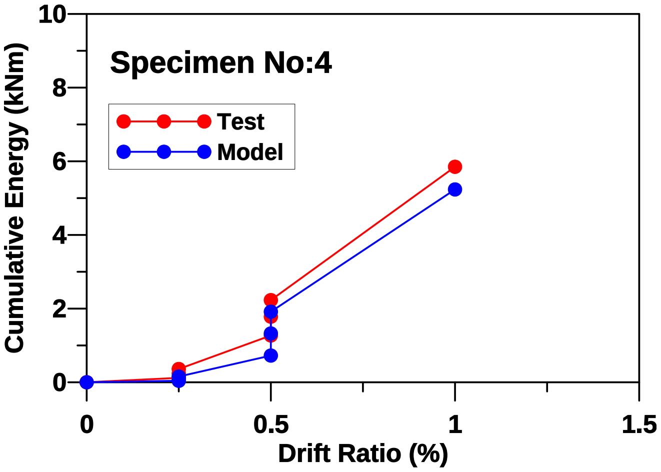

Figure A.40. Dissipated Cumulative Energy vs. Drift Level for Specimen 4 (Sezen, 2002)

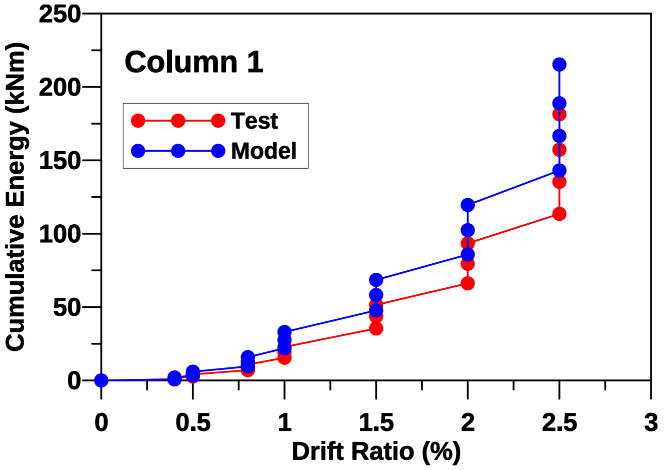

Figure A.41. Dissipated Cumulative Energy vs. Drift Level for Column 1 (Priestley and Benzoni, 1996)

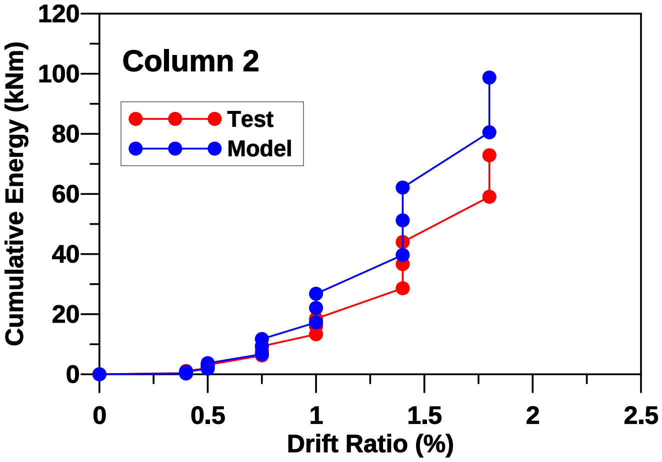

Figure A.42. Dissipated Cumulative Energy vs. Drift Level for Column 2 (Priestley and Benzoni, 1996)

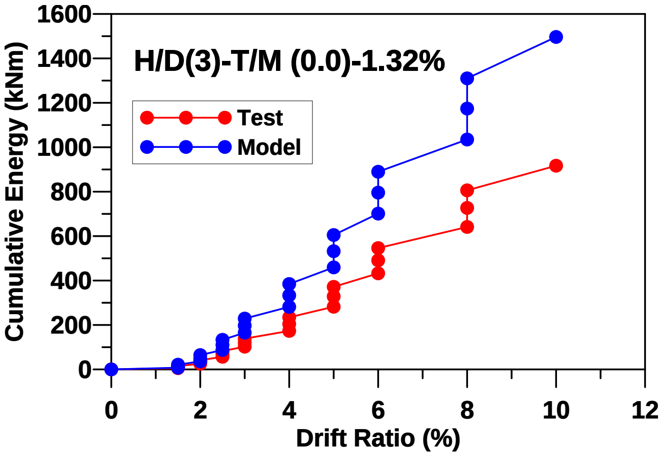

Figure A.43. Dissipated Cumulative Energy vs. Drift Level for Specimen H/D=3 T/M=0 1.32% (Shanmugam, 2009)